

---

Electronic Thesis and Dissertation Repository

---

12-15-2022 2:00 PM

# Development of a Computationally Efficient Method for Modelling Thermal Energy Storage in Packed Beds of Spherically Encapsulated Phase Change Material

Colin Jaffray, *The University of Western Ontario*

Supervisor: Straatman, Anthony G., *The University of Western Ontario*

Co-Supervisor: Siddiqui, Kamran., *The University of Western Ontario*

A thesis submitted in partial fulfillment of the requirements for the Master of Engineering Science degree in Mechanical and Materials Engineering

© Colin Jaffray 2022

Follow this and additional works at: <https://ir.lib.uwo.ca/etd>



Part of the [Energy Systems Commons](#)

---

## Recommended Citation

Jaffray, Colin, "Development of a Computationally Efficient Method for Modelling Thermal Energy Storage in Packed Beds of Spherically Encapsulated Phase Change Material" (2022). *Electronic Thesis and Dissertation Repository*. 9059.

<https://ir.lib.uwo.ca/etd/9059>

This Dissertation/Thesis is brought to you for free and open access by Scholarship@Western. It has been accepted for inclusion in Electronic Thesis and Dissertation Repository by an authorized administrator of Scholarship@Western. For more information, please contact [wlsadmin@uwo.ca](mailto:wlsadmin@uwo.ca).

## **Abstract**

A novel computationally efficient method for modelling melting and solidification processes in packed beds of PCM encapsulated spheres is introduced. The proposed method involves the full discretization of only one centrally located sphere to fully simulate the phase change process, while treating all other spheres in the packed bed as voids with boundary conditions derived from the simulated sphere. At each time step, the computed heat transfer parameters on the exterior surface of the simulated sphere undergoing the phase change process are extracted, and imposed as boundary conditions on surrounding spheres. The proposed method results in a significant reduction in computational resources that otherwise are required to simulate phase change in all spheres in the packed bed, while accurately simulating the thermal exchange between the packed bed elements and heat transfer fluid. Sample results are presented to demonstrate the proposed method.

## **Keywords**

Phase Change Material, Thermal Energy Storage, Packed Bed, Spherically Encapsulated PCM

## Summary for Lay Audience

This research work involves using computer software to simulate the melting and solidification processes of materials. The purpose of the work is to support the development of energy storage systems which rely on storing energy as heat. This type of energy storage is called thermal energy storage. Because materials absorb thermal energy as they undergo melting, they can effectively store thermal energy during their transition from a solid to a liquid. Storing thermal energy in this way can be advantageous, because the material stays at approximately the same temperature as it melts, and a significant amount of energy can be stored before the material is fully melted.

Specific materials which are used for the purpose of storing thermal energy through a change of state are considered in the study. These materials, which are called phase change materials, have certain favorable properties which make them good candidates for thermal energy storage.

It can be quite challenging to model the melting and solidification processes of phase change materials accurately. Describing the phase change process using mathematical models and computer software is difficult, and depends on the specific materials being used, and the geometry of the containers in which they are contained. This research focuses on modelling the melting and solidification of a specific phase change material in a spherical container.

The goal is to produce a computational model which is capable of accurately modelling the melting and solidification process within a single sphere, before extending the model to a larger thermal energy storage system containing many spheres.

The ultimate goal of the research is to support the development of more efficient thermal energy storage systems by providing a practical approach which can be used to test the design of different concepts. As it stands the currently established methods for testing conceptual designs are either relatively inaccurate, or require such unrealistic computational processing requirements that they are impractical to use.

## **Acknowledgements**

Thank you to friends & family, who supported me during my work and made this possible.

Special gratitude to my thesis supervisors Dr. Anthony Straatman and Dr. Kamran Siddiqui. Their expertise and vast knowledge guided every step of the research, and gave me a strong sense of direction and purpose. I will forever be grateful for having been given the opportunity to work under such formidable yet patient teachers.

Thanks to all of my colleagues at Western University, who supported my work and helped expand my knowledge of engineering software & theory. These contributions were critical to my success.

My greatest motivation will always be my parents & sister, who have supported me from the very start of my journey, and motivated me to strive for excellence.

# Contents

Abstract.....	ii
Summary for Lay Audience.....	iii
Acknowledgements.....	iv
List of Figures.....	vii
List of Tables.....	ix
List of Appendices.....	x
Nomenclature.....	xi
Abbreviations.....	xi
Mathematical Symbols.....	xi
Preface.....	xiii
1. Introduction.....	1
1.1 Background.....	3
1.1.1 Thermal Energy Storage.....	3
1.1.2 Phase Change Material.....	8
1.1.3 Packed Beds.....	13
1.2 Literature Review.....	15
1.2.1 Spherically Encapsulated PCM.....	15
1.2.2 Packed Beds of Spherically Encapsulated PCM.....	18
1.3 Motivation and Objectives.....	22
1.4 Thesis Layout.....	25
2. Model Development.....	26
2.1 General Model.....	27
2.1.1 Numerical Formulation.....	27
2.1.2 Buoyancy and Volumetric Expansion.....	28
2.1.3 Phase Change Modelling.....	30
2.1.4 Numerical Procedure.....	33
2.2 2D Cylindrical Model.....	34
2.2.1 Geometry & Materials Description.....	35
2.2.2 Mesh Generation Approach.....	37
2.2.3 Boundary Conditions.....	38
2.2.4 Grid & Timestep Independence Testing.....	41

2.2.5	Model Calibration .....	43
2.2.6	Model Validation .....	46
2.3	Spherical Model .....	48
2.3.1	Geometry & Materials Description.....	48
2.3.2	Mesh Generation Approach .....	49
2.3.3	Boundary Conditions .....	51
2.3.4	Grid & Timestep Independence Testing.....	52
2.3.5	Melting Results for the Spherical Case.....	54
2.3.6	Discussion of Spherical Melting Behavior & Implications Thereof .....	56
3.	Approach for Modelling Packed Beds of Spherically Encapsulated PCM .....	62
3.1	Model Implementation in a Packed Bed .....	63
3.1.1	Geometry & Materials Description.....	63
3.1.2	Mesh Generation Approach .....	65
3.1.3	Boundary Conditions .....	67
3.1.4	Numerical Procedure .....	70
3.1.5	Flow Through the Packed Bed.....	71
3.2	Computationally Efficient Method Introduction.....	73
3.2.1	General Description of the Method.....	73
3.2.2	Heat Flux Correction.....	75
3.3	Demonstration of the Method Via Parametric Study .....	79
3.3.1	Reference Cases .....	80
3.3.2	Variations in Sphere Diameter.....	84
3.3.3	Variations in Inlet Temperature .....	87
4.	Summary and Conclusions .....	91
4.1	Recommendations for Future Study.....	93
	Bibliography .....	94
	Appendices.....	99
	Appendix A – PCM Property Tables .....	99
	Curriculum Vitae .....	105

## List of Figures

Figure 1.1 – Average Hourly Electrical Demand for Different States for Different Seasons [1]... 1	
Figure 1.2 - Period of surplus solar energy requiring energy storage [6]. .... 4	4
Figure 1.3 - Standard Heating Curve [6] for a generic material that can exist in three phases. .... 4	4
Figure 1.4 - PCM classification tree [7]...... 11	11
Figure 1.5 - Schematic of a simple packed bed device [16]. ..... 13	13
Figure 2.1 - Diagram of the model development progression. .... 26	26
Figure 2.2 - Schematic of the cylindrical cavity used by Teather and Siddiqui [54]. ..... 36	36
Figure 2.3 - Illustration of hexahedral O-grid mesh structure for phase change material and acrylic wall..... 37	37
Figure 2.4 - Boundary condition locations shown on the quasi two-dimensional cylinder geometry. .... 40	40
Figure 2.5 – Simulated contours of liquid fraction (right columns) at different moments in the melting process compared to the physical reference experiment (left columns). .... 45	45
Figure 2.6 – Solid-liquid interface comparison during melting for two-dimensional cylinder Left = Reference experiment [54], Right = Numerical model ..... 47	47
Figure 2.7 - 2D Diagram of the considered spherical Geometry (dimensions in mm)..... 49	49
Figure 2.8 - Hexahedral O-grid mesh structure for the single encapsulated sphere case ..... 50	50
Figure 2.9 - PCM melting time comparison for different grid resolutions & Time steps ..... 53	53
Figure 2.10 – Graph of liquid fraction vs time for the spherical case considered. .... 54	54
Figure 2.11 - Contours of liquid fraction taken at a vertical midplane at different time intervals for the three-dimensional sphere during the melting process..... 55	55
Figure 2.12 – Contours of liquid fraction for the spherical case at 68% volume average liquid fraction, taken at a vertical midplane..... 56	56
Figure 2.13 – Velocity contours corresponding to a 68% volume average liquid fraction melting PCM sphere, taken at a vertical midplane. .... 57	57
Figure 2.14 – Velocity vector field corresponding to a 68% volume average liquid fraction melting PCM Sphere, taken at a vertical midplane..... 58	58
Figure 2.15 – Three-dimensional view of the velocity vector field corresponding to a 68% volume average liquid fraction melting PCM sphere, taken at a horizontal plane at the top of the solid-liquid PCM interface (plane shown in figure 2.14). .... 59	59

Figure 2.16 – Temperature contours corresponding to a 68% volume average liquid fraction melting PCM sphere, taken at a vertical midplane. ....	60
Figure 2.17 – Area average heat transfer coefficient plotted against the liquid fraction (melt fraction) of the spherically encapsulated PCM. ....	61
Figure 3.1- 2D Schematic of the 3D packed bed geometry considered (dimensions in mm). ....	64
Figure 3.2 - Isometric and 2D view of the 3×3×3 sphere packed bed mesh. The blue boundary is the inlet, and the red boundary is the outlet. ....	65
Figure 3.3 - Clustering of grid Elements towards the sphere wall boundaries in the outer flow field for the packed bed mesh. ....	66
Figure 3.4 - Schematic of the Boundary Condition Locations Used for the Packed Bed. ....	69
Figure 3.5 - Velocity vector field in the packed bed of PCM encapsulated spheres, taken at a diagonal middle plane at the start of the melting process. The packed bed flow field is constant throughout the melting process. ....	71
Figure 3.6- Schematic Representation of Translational Heat Flux Method. ....	74
Figure 3.7 – Variation in the mean temperature of a fluid in an internal pipe flow with constant wall temperature. ....	76
Figure 3.8 - Contours of liquid Fraction (top) and temperature field (bottom) at different time intervals in a packed bed melting process using the translational heat flux method. ....	81
Figure 3.9 - Contours of liquid fraction (top) and temperature field (bottom) at different time intervals in a packed bed solidification process using the translational heat flux method. ....	83
Figure 3.10 - Comparison of central sphere melting time for different sphere diameters. ....	85
Figure 3.11 - Comparison of central sphere solidification time for different sphere diameters. ...	86
Figure 3.12 - Comparison of central sphere melting time for different HTF inlet temperatures (phase transition temperature 299K). ....	88
Figure 3.13 - Comparison of central sphere solidification time for different HTF inlet temperatures (phase transition temperature 299°K). ....	89



## List of Tables

Table 2.1 – Summary of numerical methods used.....	34
Table 2.2 – RT26 PCM material properties [55,56]. .....	36
Table 2.3 – Acrylic material properties [57].....	37
Table 2.4 - Summary of boundary conditions imposed on the quasi two-dimensional cylinder for melting and solidification simulations. ....	39
Table 2.5 - Grid independence test results for melting of PCM in a quasi two-dimensional cylinder. ....	42
Table 2.6 – Timestep independence test results for melting of PCM in a quasi two-dimensional cylinder. ....	42
Table 2.7 - Summary of boundary conditions imposed on the three-dimensional sphere for melting simulations. ....	51
Table 3.1 - Summary of boundary conditions imposed on the three-dimensional packed bed for melting and solidification simulations. ....	67
Table 3.2 - Summary of Numerical Methods Used for The Packed Bed Cases.....	70

# List of Appendices

Appendices.....	99
Appendix A – PCM Property Tables .....	99

# Nomenclature

## Abbreviations

CFD – Computational Fluid Dynamics

HTF – Heat Transfer Fluid

LHS – Latent Heat Storage

PCM – Phase Change Material

TES – Thermal Energy Storage

## Mathematical Symbols

$A_{mush}$  - Mushy Zone Constant [Dimensionless]

$A_S$  – Surface Area of Sphere [ $m^2$ ]

$C_p$  – Specific Heat Capacity [J/kg-K]

$\vec{F}$  – External Body Forces [N]

$\vec{g}$  – Gravitational Acceleration [ $m/s^2$ ]

$h$  - Convective heat transfer coefficient [ $W/m^2-K$ ]

$H_L$  – Enthalpy [J/kg]

$L$  – Latent Heat Capacity [J/kg]

$m$  – Mass [kg]

$\dot{m}$  – Mass flow rate [kg/s]

$N$  – Number of spheres [Dimensionless]

$p$  – Pressure [Pa]

$Q$  – Thermal Energy [J]

$S_e$  – Energy Source Term

$S_m$  – Momentum Source Term

$t$  – Time [s]

$T$  – Temperature [K]

$\bar{U}$  – Average overall heat transfer coefficient [ $\text{W}/\text{m}^2\text{-K}$ ]

$\vec{v}$  – Velocity [m/s]

$\alpha$  – Thermal Expansion Coefficient [ $1/\text{K}$ ]

$\beta$  – Liquid Fraction [Dimensionless]

$\Delta$  – Delta/Difference [Dimensionless]

$\nabla$  - Gradient [Dimensionless]

$\rho$  – Density [ $\text{kg}/\text{m}^3$ ]

$\tau$  – Stress Tensor

$\phi$  – Heat Flux [ $\text{W}/\text{m}^2$ ]

## **Preface**

In the past century, the earth has experienced an unprecedented amount of greenhouse gas emissions. The ever-increasing level of pollution generated by the human race has contributed to significant atmospheric deterioration, and ozone layer depletion.

The long-term consequences of global warming are still disputed by many, but the general consensus is that global warming is negatively impacting the planet and its inhabitants. Therefore, many nations around the world have attempted to implement environmental policies and international agreements which limit and regulate the allowable amount of environmentally damaging emissions which can be generated. These policies and agreements are implemented in an attempt to reduce the rate of growth of greenhouse gas emissions globally.

Despite the adoption of these policies however, the rate of greenhouse gas emissions continues to rise globally on a yearly basis. This is largely attributed to the fact that adherence to environmentally friendly policy typically bears significant economic cost. Because of this, it is difficult or impossible for many industries to pursue environmentally friendly practices, because the short-term economic consequences of doing so represent more of an immediate threat than the long-term consequences of global warming. There is therefore an urgent need to develop processes, industries, and technologies that are both environmentally friendly, and equally or more economically viable than their classical counterparts. The successful development and deployment of such technologies has the potential to greatly reduce environmental impacts.

# Chapter 1

## 1. Introduction

Among the most relevant technological fields in addressing environmental issues are those that deal with energy and its management. It is important to improve the efficiency with which energy is managed, including energy generation, consumption, and energy storage. Efficient energy storage can be particularly challenging. Energy demand is not constant because of the way energy use varies at different times throughout the year (for climate reasons), or even throughout the day (usage peaks during the day and diminishes overnight) [1]. The variation in electrical energy demand with respect to time of day and time of year in the US is shown in figure 1.1 [1].

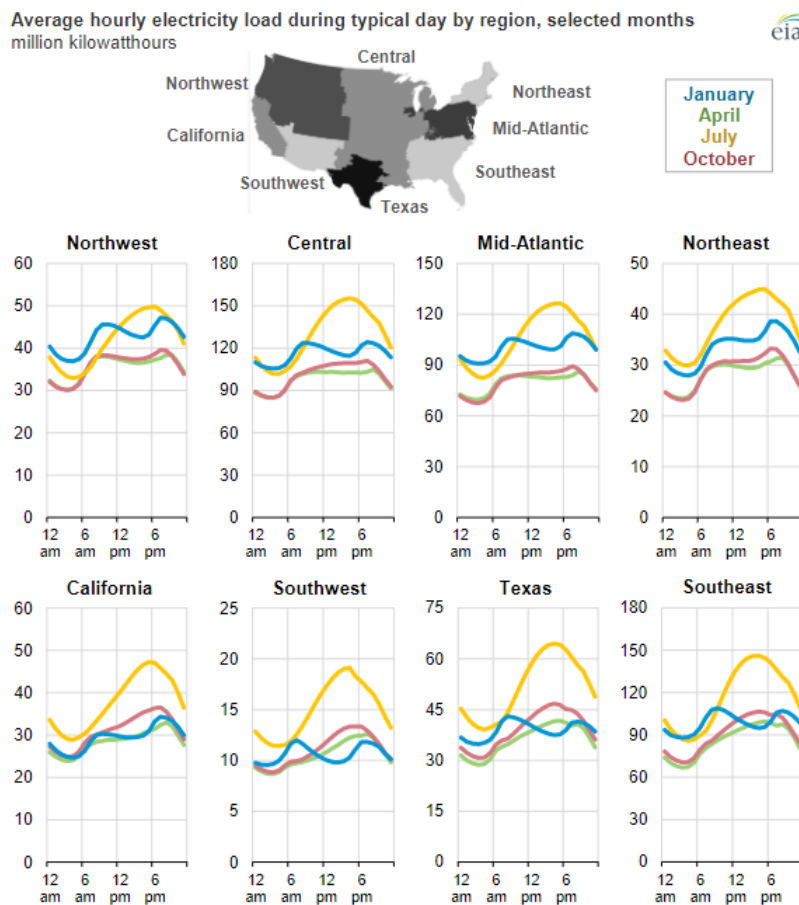


Figure 1.1 – Average Hourly Electrical Demand for Different States for Different Seasons [1].

It can be difficult to design flexible energy generating systems capable of generating energy in accordance with the rate at which energy demand varies. Often times energy generating systems are scaled to meet the maximum possible demand (periods in which energy consumption is highest), and are liable to generate surplus or additional energy in periods where energy demand is low [2]. It is therefore extremely important to be able to manage the surplus energy efficiently by means of efficient energy storage, so that this extra energy is not wasted. Stored energy can then be recovered from an energy storage system in periods of high demand, thus improving the effectiveness of the overall energy generation and management system, leading to a reduction in environmental cost.

Many forms of energy storage exist. Typically, the quantity of energy recovered from energy storage systems is lower than the energy input, resulting in low round-trip efficiencies [2]. Energy storage processes which rely on the conversion of energy from one form to another for the purpose of storage often suffer a reduction in the quality of the useful energy (i.e. the exergy loss), due to the irreversibility associated with energy conversion processes, leading to reduced overall efficiency. It is therefore desirable to be able to store energy directly before it has undergone too many energy conversion processes [3].

Many energy systems rely on thermal energy as the source, such as solar thermal or steam-based power generation. Efficient thermal energy storage has the potential to significantly improve the overall effectiveness of such energy systems [4]. This is especially true for intermittent energy sources such as solar thermal. The ability to store solar thermal energy in times of an energy abundance (daylight) and then efficiently recover and use that thermal energy during periods where the solar energy is not available, can elevate these types of energy system from niche applications to mainstream viability. In the more general sense, effective thermal energy storage can be used to improve the overall effectiveness of any process that generates thermal energy, or produces waste heat as a byproduct. There are a myriad of opportunities for energy storage systems to improve overall energy management, and reduce environmental impacts, in almost every industry and sector.

The research work presented herein is performed with the goal of supporting the development of efficient and effective thermal energy storage systems. It is the author's hope that their contribution to the development of better, more efficient energy management systems can

ultimately contribute to a reduction in environmental emissions, and help preserve the planet and its environment for years to come.

## **1.1 Background**

### **1.1.1 Thermal Energy Storage**

Energy can be stored in many different forms, depending on how the energy is generated, and the target destination for the energy after being recovered from storage.

Among energy storage options, thermal energy storage (TES) has gained significant attention in recent years due to its dual benefit of supporting energy conservation (e.g. from conventional energy resources) and reliable integration of renewable energy resources such as solar energy [2].

TES uses the concept that energy can be stored as thermal energy, or heat within some substance or material. This is accomplished by heating some storage medium with some thermal energy source by means of some heat transfer mechanism. If the storage medium is able to retain this thermal energy, it is effectively storing the heat, which can then be recovered at a later time when the thermal energy is in demand.

TES systems in general are particularly attractive for use in energy systems that already rely on thermal energy generation, such as solar-based power generation [2]. Since TES systems store thermal energy directly, they can reach round-trip efficiencies of upwards of 95% [3]. TES also pairs inherently well with intermittent energy generation sources such as solar to increase their reliability, and can be used to offset the non-availability periods of such energy systems by providing thermal energy consistently [4]. Almost half (47%) of the currently installed concentrated solar power generating systems in the world are integrated with TES systems because of their inherent compatibility [5].

A visualization of the mismatch between energy availability and energy demand for solar energy is presented in figure 1.2 [6].



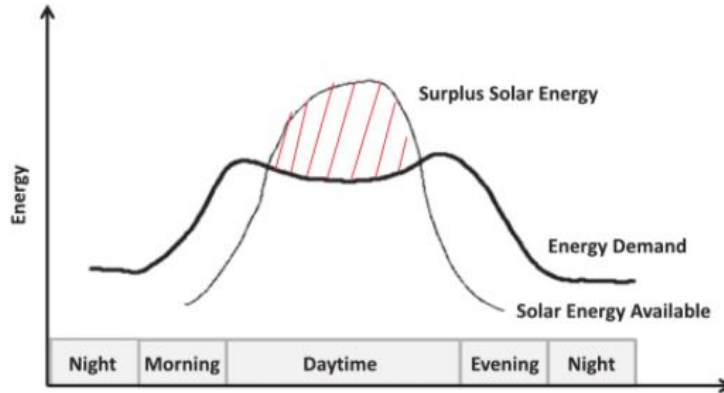


Figure 1.2 - Period of surplus solar energy requiring energy storage [6].

With respect to figure 1.2, the surplus solar energy (the red hatched region), which is already in the form of thermal energy, could be stored for future use if an efficient thermal energy storage mechanism were available. The ability to store the surplus energy and recover it efficiently during the period where availability is lower than the demand has the potential to greatly improve the effectiveness of the system overall.

One of the primary considerations when designing a thermal energy storage system is the selection of an appropriate storage medium. This involves the selection of a material or substance which will act as the storage medium, by virtue of being heated by the thermal energy source. In terms of a material or substance's ability to store and retain heat, there are two general types of heat to consider: sensible heat, and latent heat. The standard heating curve for a typical material is shown in figure 1.3. [6]

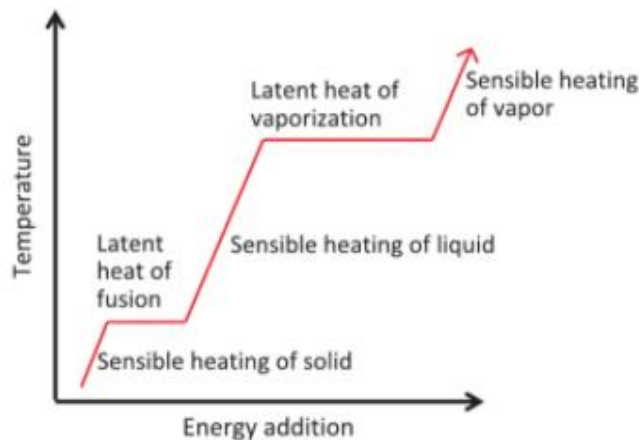


Figure 1.3 - Standard Heating Curve [6] for a generic material that can exist in three phases.

With respect to the heating curve shown in figure 1.3, the overall heating process for a material starting in the solid state can be described as follows:

- Any increase in thermal energy content contributes to sensible heating of the solid, until the melting temperature is reached.
- At the melting temperature, any increase in thermal energy content contributes to a change in state between solid and liquid, until the material has been entirely converted into a liquid.
- Further increase in thermal energy content contributes to sensible heating of the liquid, until the vaporization temperature is reached.
- At the vaporization temperature, any increase in thermal energy content contributes to a change in state between liquid and gas, until the material has been entirely converted into a gas.
- Further increase in thermal energy content contributes to sensible heating of the gas.

A further explanation of both sensible heat and latent heat, and their relation to thermal energy storage is provided in the following sections.

### ***Sensible Heat***

Sensible heating refers to a substance's ability to store heat or thermal energy in the form of a temperature increase of the material. As a material increases in temperature, its sensible heat or thermal energy content increases as well. The key property used to describe a substance's ability to contain thermal energy in the form of a temperature increase is the heat capacity of the substance, often denoted by  $C_p$  (constant pressure heat capacity) or  $C_v$  (constant volume heat capacity). This material specific property, which is given in units of energy change per change in temperature on a mass specific basis, effectively describes how much the thermal energy content of the substance changes as the temperature of the substance changes. This property is also typically a function of the temperature and pressure of the substance [6], meaning that the storage capacity of TES systems that rely on sensible heating is liable to change as the temperature of the storage media increases or decreases [6]. The change in thermal energy content of a substance experiencing sensible heating can be described using the following expression:

$$\Delta Q = mC\Delta T$$

where

- $\Delta Q$  is the change in the thermal energy content of the material (J)
- $m$  is the mass of the material experiencing sensible heating (kg)
- $C$  ( $C_p$  or  $C_v$ ) is the mass specific heat capacity of the substance (J/kg K)
- $\Delta T$  is the change in temperature of the material experiencing sensible heating (K or °C)

In general, materials with a higher heat capacity are capable of storing more thermal energy as sensible heat, and are therefore better suited to TES systems which rely on sensible heating [6]. A significant challenge, however, when designing TES systems that rely on sensible heating is the storage medium's natural tendency to dissipate or exchange heat with its surroundings. Further compounding the issue is that energy is dissipated at an increased rate as the temperature of the storage medium increases. Sensible heating TES systems therefore need to be well insulated to prevent energy loss to the surroundings, which can adversely affect energy charge and discharge rates into the storage device from the thermal energy source.

Additionally, the rate of heat transfer into the sensible heat TES system is proportional to the temperature difference between the storage medium and the heat source. Because of this, the charging rate typically diminishes as the storage device approaches the temperature of the heat source, at which point no further sensible heating is possible. Consequently, sensible heat TES systems often have poor round-trip efficiencies due to their tendency to lose heat to their surroundings, and are not stable for long term energy storage for the same reason [6]. These challenges often make it impractical to employ sensible heat TES as an effective energy storage strategy for many applications.

### ***Latent Heat***

When a material or substance approaches its melting temperature (the temperature at which it begins to transition from a solid state to a liquid state), or its boiling temperature (the temperature at which it begins to transition from a liquid state to a gaseous state), it may continue to absorb

thermal energy and increase in thermal energy content. However, a change in temperature will no longer be observed, as the further change in energy content will instead be contributed towards a change of state of the material [6]. The energy associated to the change of state (phase change) of the material is referred to as the latent heat content, and, like the heat capacity in the case of sensible heating, is a material specific property.

The latent heat capacity of a material is called the latent heat of fusion when the phase change is between the solid and liquid phase, and the latent heat of vaporization when the phase change is between the liquid and gas phase. This property is typically given in terms of the energy requirement to fully transition from one state to another on a mass specific basis. The change in thermal energy content of a substance having undergone a phase change can be described using the following expression:

$$\Delta Q = mL$$

where

- $\Delta Q$  is the change in the thermal energy content of the material (J)
- $m$  is the mass of the material undergoing phase change (kg)
- $L$  is the latent heat capacity of the material for the appropriate change of state (J/kg)

In general, materials with a higher latent heat capacity are capable of storing more thermal energy as latent heat, and are therefore better suited to TES systems which rely on latent heating [6].

Latent heat storage is a particularly attractive option for TES for several reasons. During a latent heat storage process, the energy storage medium typically remains at a near uniform temperature, therefore the temperature difference between the storage medium and the energy source or sink remains relatively constant. The isothermal nature of the energy storage and discharge process is therefore of significance for designing TES systems that rely on the steady rate of heat transfer being a primary design consideration.

An additional advantage of the isothermal nature of latent heat TES systems is that the temperature difference between the storage medium and the surrounding environment is approximately

constant, and does not grow as the energy content of the storage medium increases, as is the case with sensible heating. This makes it easier to prevent energy losses to the surroundings, and in general results in a higher round trip efficiency for TES systems that employ latent heating vs those that employ sensible heating [4].

As latent heat storage systems store heat primarily as latent heat, their energy storage density is also 50-100 times greater than sensible heat storage systems [4], thus latent heat storage systems are typically more compact and occupy less physical space. This is again a desirable quality in terms of designing TES systems for practical applications, where physical space constraints are often a relevant factor.

Materials that are designed specifically for the purpose of storing thermal energy as latent heat are referred to as phase change materials (PCMs) or latent heat storage materials. PCMs are of significant interest in thermal energy storage applications, given the energy density of latent heat, and the constant temperature at which a phase change will occur, both of which are favorable for thermal energy storage [6]. Some relevant background information regarding phase change materials is presented in the following section.

### **1.1.2 Phase Change Material**

Materials which are specifically designed for the storage of thermal energy as latent heat are often referred to as phase change materials, or PCMs.

#### ***PCM Properties***

While almost every material or substance is capable of undergoing a phase change, PCMs generally have certain favorable thermophysical properties which lend themselves well to acting as thermal energy storage media. The following PCM material properties are of importance when selecting PCMs as storage media for thermal energy storage applications [7].

### Thermodynamic Properties

- 1) High latent heat capacity of fusion
- 2) High thermal conductivity
- 3) Appropriate melting/solidification temperature for the application

A high latent heat capacity of fusion corresponds to the energy density that the PCM based TES system is capable of achieving. At higher latent heat capacities, PCMs are capable of storing more thermal energy per unit mass, meaning less material is required. Specifically, the latent heat of fusion (and not some other change of state) is of importance, as almost all PCM are designed for use between the solid and liquid phases [7].

High thermal conductivity is important in order to satisfy the charging and discharging rate requirements for the given application. Higher thermal conductivity means faster charge and discharge of the storage device, which is often a primary design consideration [7].

Different materials will undergo a phase transition at different temperatures, so the selection of a material with the appropriate transition temperature for the given application is also of importance. The transition temperature should allow for a moderate temperature difference in both charging and discharging, so that meaningful heat transfer may occur [7].

### Physical Properties

- 1) High density
- 2) Minimal volumetric expansion

A greater density is desirable for the same reason as a high latent heat capacity – an increase in energy density. Because physical space constraints are often a consideration for practical applications, greater density results in PCM based TES systems occupying less physical space [7].

Typical material undergoes minor volumetric expansion during sensible heating, and moderate volumetric expansion during a change of state. Because PCMs typically must be enclosed within some sort of container, it is desirable to select materials that experience a relatively low degree of volumetric expansion during both sensible heating and a change of state [7].

### Chemical Properties

- 1) Chemically stable
- 2) Inert
- 3) Non-toxic & safe
- 4) Nonflammable

A suitable PCM should be chemically stable over time, and not subject to degradation. This allows for the PCM based TES system to function as intended over an extended time period.

The materials should also be inert, with no chemical reaction occurring between the PCM and the encapsulating material or other substances in the surroundings.

For safety reasons the materials would also ideally be non-toxic and nonflammable.

### Economic Properties

- 1) Abundant
- 2) Inexpensive

Ideal PCM should be readily available and inexpensive. Regardless of material performance, if the material is extremely rare or expensive to procure, then it will likely not be suitable for most practical applications, given cost is always a consideration.

### ***PCM Classifications***

Phase change materials are usually separated into three broad classifications: organic, inorganic, and eutectic [7]. A classification diagram of PCMs is given in figure 1.4, with a high-level summary of each classification given in the subsequent text: [7]

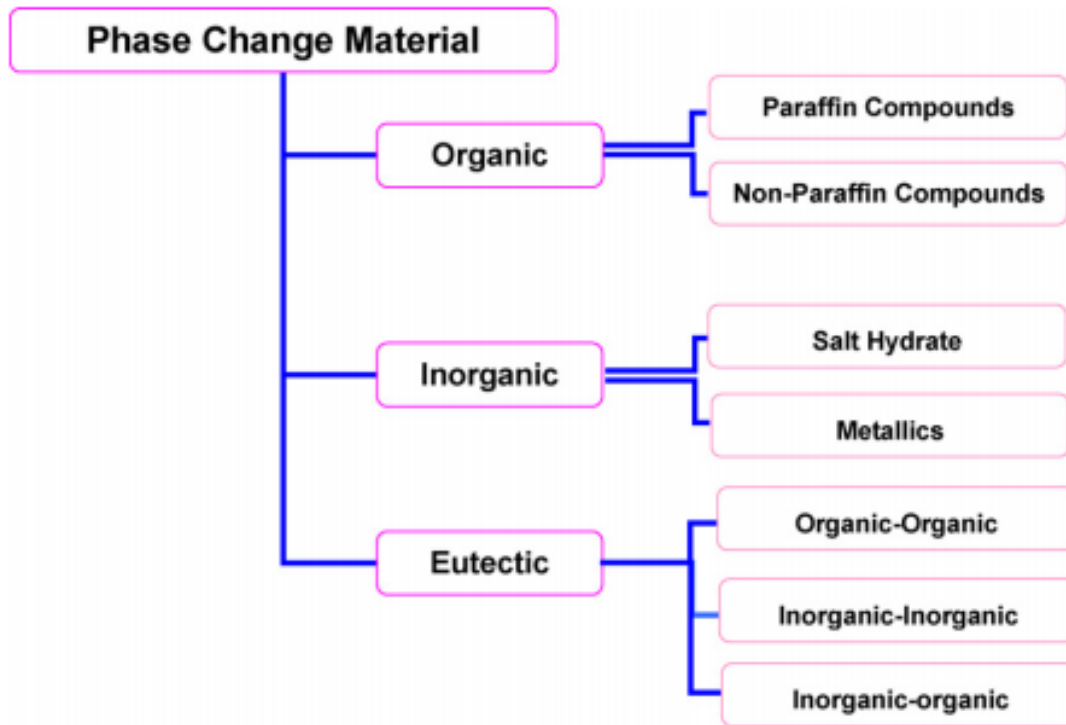


Figure 1.4 - PCM classification tree [7].

### Organic Phase Change Materials

Organic PCMs are the group of PCMs whose chemical compositions contain carbon. Among the most commonly used organic PCM materials are the paraffin waxes, which are the hydrocarbons of the molecular form  $C_nH_{2n+2}$  [8]. These paraffin waxes exhibit a wide range of transition temperatures based on their molecular weight, and typically have high latent heat capacities. They often have low thermal conductivity, and are sometimes moderately flammable as many are used as fuels [7]. They are often non-inert and thus difficult to enclose or encapsulate using typical plastic materials. The transition temperature and latent heat capacities of some common paraffins are included in Appendix A1.

Other organic PCMs that are suitable candidates for latent heat storage include alcohols, glycols, esters, and various fatty acids [7]. These materials likewise have many favorable properties for TES, such as high latent heat capacities, are often safer than the paraffin waxes. The transition temperature and latent heat capacities of some common fatty acids are included in Appendix A2.



### Inorganic Phase Change Materials

The most commonly used PCM in industry (currently) are the salt hydrates [6], belonging to the inorganic PCM classification. These PCMs are usually a combination of water and some inorganic salt of the molecular form  $AB \cdot nH_2O$ , where AB is the salt compound [9]. These salt hydrates often possess high latent heat capacities, and relatively high thermal conductivity when compared to the organic paraffin PCMs. They also tend to experience a relatively low degree of volumetric expansion during both sensible heating and during the phase change. The transition temperature and latent heat capacities of some common salt hydrates are included in Appendix A3.

Other PCMs belonging to the inorganic classification include metallic PCMs. Metals typically have high thermal conductivity and high transition temperature ranges, but relatively low latent heat capacity [10]. Metal PCMs are typically not considered for most PCM applications because of their prohibitive cost and liability to undergo chemical interactions with their surroundings such as corrosion or oxidation. They may however be the only suitable materials for applications requiring very high transition temperatures [10]. The transition temperature and latent heat capacities of some common metallic PCMs are included in Appendix A4.

### Eutectic Phase Change Materials

The eutectic phase change materials are composite materials comprised of two or more components which change phase simultaneously. The materials form a mixture which behaves as a single composite material [11]. Many of the eutectic PCMs are combinations of other inorganic and organic PCMs, and are combined in an attempt to maximize the favorable properties of their constituents while eliminating or reducing less favorable properties. They are considered the most “engineered” of the PCM classifications, and are generally more expensive [10]. The transition temperature and latent heat capacities of some eutectic materials are included in Appendix A5.

In general, heat transfer rate is often the limiting factor when designing TES that employ PCMs as energy storage media [12]. Most PCMs suffer from low thermal conductivity, thus limiting their ability to effectively transfer heat, particularly in their solid phase, hence, negatively impacting charging and discharging rates, which may become inadequate to meet the demand of practical applications. This challenge can be somewhat overcome by increasing the thermal conductivity

of the materials [13,14] or by optimizing the design of the heat exchanging mechanisms into the PCM using different configurations [15].

Because PCMs transform into their liquid phase as they undergo heating, they typically must be held within some type of container. PCMs contained within spherical enclosures are referred to as spherically encapsulated PCMs. Spherical encapsulation geometries are among the most common in industrial applications, and have inherent compatibility with many heat exchange configurations due to their tendency to offer reduced flow resistance to the surrounding heat transfer fluid. [15]. A common heat exchange configuration which often utilizes spherical heat exchanger elements is called a packed bed.

### 1.1.3 Packed Beds

Packed beds are commonly used in chemical engineering operations and appear in industries such as chemical, biochemical, petrochemical, and pharmaceutical. Depending on the application, the primary function of packed beds can be to facilitate chemical reactions, to serve as heat exchangers or mass transfer devices, or to act as filtration devices [16]. Of special interest for the purpose of this paper is the application of packed beds as heat exchangers.

A schematic of a typical packed bed in its simplest form is provided in figure 1.5 [16].



Figure 1.5 - Schematic of a simple packed bed device [16].

The working principle of a simple packed bed device for the purpose of acting as a heat exchanger or thermal energy storage device are as follows:

The packed bed device is comprised of a large container that is filled with some packing material (the grey hatched region in figure 1.5). The packing can be randomly filled with small objects like pellets, particles, rings, or spheres, or it can be designed for specific structured packing arrangements such as long tubes or organized lattice structures [16]. For the purpose of thermal energy storage, the packed bed container should be well insulated to minimize heat loss to the surroundings, and the packing material should be some material capable of effective heat retention and transfer.

Some thermally charged heat transfer fluid (HTF) is allowed to enter the packed bed device through an inlet orifice (top of figure 1.5), carrying thermal energy from the thermal energy source. As this HTF passes through the packed bed, thermal energy is transferred from the HTF to the surrounding packing material, thereby increasing the thermal energy content of the packed bed [16]. Once the HTF exits the packed bed through the outlet orifice (bottom of figure 1.5), it will have lost some of its thermal energy content and can be recycled back through the thermal energy source for reheating, or disposed of.

Typical packed bed devices also include some sort of filter or containment just inboard of both the inlet and outlet, to prevent the packing material from escaping the device via these orifices. Passing through these filtration mechanisms does however contribute to a pressure loss in the surrounding HTF, as does passing through the packing material. These pressure losses should be accounted for in the pressurized system supplying the HTF, and can primarily be characterized by the bed packing arrangement and particle size, bed length, and HTF Reynolds number and physical properties [17].

A typical application for this type of packed bed for heat storage application is for industrial waste heat recovery [16]. Hot exhaust gases from some industrial process are allowed to escape through a packed bed vessel that is packed with some heat storage media, thereby heating the packing. Afterwards other cool gases such as atmospheric air are fed back through the packed bed device for the purpose of preheating the air.

The great advantage of this type of heat exchanger and heat storage device is the large surface area to volume ratio that the packing material experiences when deployed in this type of configuration. Because heat transfer rate is typically proportional to surface area, increasing the surface area with which the heat storage medium is in contact with the surrounding heat transfer fluid can greatly improve the heat transfer rate into and out of the packing material when compared to the same quantity of packing material deployed in other less favorable geometries. Packed bed heat exchangers also have the added benefit of utilizing both convective and conductive heat transfer mechanisms, which again further improve the rate of heat transfer they are capable of achieving.

Typical packed bed thermal energy storage devices that are currently used in industry almost exclusively rely on sensible heating [16], and still suffer from relatively low thermal efficiencies. While these waste heat recovery devices are still an improvement over no waste heat recovery mechanism at all, there exists significant room for improvement in terms of their ability to retain a larger fraction of the thermal energy that they are exposed to.

Packed beds containing latent heat storage/phase change materials are emerging as potential candidates for waste heat recovery and thermal energy storage applications, though these technologies are still in their infancy. The development of these devices is still largely academic, and have not yet seen widespread adoption in industry. In the following section, a literature review is presented summarizing the current literature on the subject of spherically encapsulated PCMs, and packed beds of encapsulated PCM.

## **1.2 Literature Review**

### **1.2.1 Spherically Encapsulated PCM**

Despite an increase of research interest and studies regarding the energy deposition and withdrawal processes in spherically encapsulated PCMs in last decade, there is no generally accepted approach developed for modelling and predicting the behavior of melting and solidification processes of PCMs in spherical containers using numerical modelling [18].

The melting and solidification process of phase change materials is always accompanied by a moving solid-liquid interface, separating the two phases. This type of problem is referred to as a “moving boundary problem”, or Stefan’s problem, attributed to Stefan because of his study of ice cap formation near the north pole in 1981 [19]. This early work was one of the first to study the position of the liquid-solid interface over time during melting and solidification processes, though was strictly one-dimensional and involved many simplifications.

Generally, the melting of PCM within encapsulated spheres is broadly classified under two main categories: The solid and liquid phase have the same density (constrained melting), and the solid and liquid phase have different densities (unconstrained melting) [20].

One of the earliest works regarding the numerical modelling of constrained PCM was provided by Khodadadi and Zhang in 2001 [21]. The work concluded that the buoyancy-driven convection within the melting gradually became the dominant heat transfer mechanism as a larger fraction of liquid appeared within the sphere. The work also highlighted the formation of several time-dependent recirculation currents forming within the sphere, as a result of the buoyancy. The final conclusions suggest that correctly characterizing the buoyancy driven convection and recirculation currents are the most important parts of accurately modelling the PCM melting process.

In 2008 Tan carried out the work in [22], studying the constrained and unconstrained melting for spherically encapsulated PCM with physical experiments for different initial PCM temperatures. The work drew similar conclusions to that in [21] regarding heat transfer mechanisms - that conduction is the dominant heat transfer mechanism early in the melting process, whereas convection heat transfer becomes dominant as the melting progresses. The work also suggests that unconstrained melting occurs faster than constrained melting.

In 2009 Tan et al. [23] published experimental and numerical work which was focused on better understanding the role of the buoyancy-driven convection during constrained PCM melting processes within spherical containers. The work demonstrated that a large degree of thermal stratification occurs in the upper half of the PCM sphere as a consequence of the melted PCM rising along the walls of the spherical container and displacing colder fluid. The work also attributed to the waviness at the bottom of solid PCM during melting to the presence of an unstable fluid layer, bounded on all sides by the vertical recirculation currents. The authors attributed the

discrepancy between the numerical results and the physical experiment to the fact that the two-dimensional numerical model failed to account for three-dimensional melting effects.

The 2015 work of Galione et al. [24] compared both a three-dimensional model and two-dimensional model to the work of Tan et al. [23]. The comparison demonstrated that three-dimensional numerical simulations provided a closer approximation to the experimental results presented in [23] than the two-dimensional study, suggesting that three-dimensional modelling was important to accurately capture the melting behavior, suggesting a departure from axisymmetry about the vertical axis of the PCM sphere.

Li et al. [25] developed a numerical model and accompanying physical experiment to study the constrained melting of PCM encapsulated in spherical enclosures. The experimental and numerical work involved a parametric study which varied the sphere diameter, PCM thermal conductivity, shell material, and external temperature. In general, the numerical studies showed relatively poor accordance with their experimental counterparts. The findings from their work concluded that hotter external temperatures, smaller diameter spheres, higher thermal conductivity PCMs, and higher thermal conductivity shell materials all contributed to faster melting times, as would be expected.

Sattari et al. [26] conducted a numerical study in an attempt to replicate the geometry used in the physical experiment by Tan et al. [23], as had been done by Galione et al. [24] using different mathematical models. Their work drew similar conclusions to that in [25] regarding the impact of the sphere wall temperature and sphere diameter on melting time, and suggested that the sphere wall temperature was overall the largest contributor to the overall melting time of the PCM. Their numerical work however showed poorer accordance with the physical experiment in [23] than the numerical study in [24] which used the same experimental results as validation, suggesting that the model development approach used in [24] are superior to that in [26].

In 2018, Soni et al. [27] performed a numerical study for the purpose of investigating the reasons for discrepancies between numerical studies and experimental results in previous works regarding the melting of PCM in encapsulated spheres. Again, the physical experiments conducted by Tan et al. [23] are used as the basis of comparison. The study involved using a numerical model which considered a difference in thermal conductivity between the liquid and solid PCM states, and a numerical model where thermal conductivity was constant between the solid and liquid state. The

findings suggest that the numerical model where the thermal conductivity was allowed to vary between the liquid and solid state showed better accordance with the experimental results in [23] than the model where thermal conductivities were constant, though both models still showed some discrepancy with the experimental results.

A recurring trait in all of the literature considered is the various authors' adamancy that correctly modelling the melting process of PCM encapsulated spheres is largely attributed to correctly modelling the buoyancy induced natural convection within the melting. All studies point to this behavior as being the most difficult to model accurately, and being the largest contributing factor towards discrepancies between physical experiments and numerical models. Many of the constrained melting studies considered use the Boussinesq approximation in combination with a thermal expansion coefficient to model the buoyancy forces and natural convection that result from the temperature gradients which occur inside the melt.

Another important conclusion drawn in the literature is that three dimensional studies provide closer approximations to experimental results than two dimensional studies. Accurately capturing the three-dimensional melting behavior is important for producing results which match most closely with physical experiments.

While these general similarities and best practices can be drawn from the studies considered, almost all deviate from each other in terms of the numerical implementation, boundary conditions, meshing strategies, and modelling approach, even when considering the same geometry and materials. A generally accepted and universally used approach for modelling the melting process in PCM encapsulated spheres is yet to be reported.

## **1.2.2 Packed Beds of Spherically Encapsulated PCM**

Packed bed TES has been extensively studied for use in certain applications, particularly for coupling with concentrated solar power systems [28-36]. These studies investigate the performance of packed beds of solid storage media (sensible heat storage) contained in tanks of liquid or gas heat transfer fluids. Such packed bed TES systems demonstrate good performance in terms of energy density, heat transfer rate and cost, as summarized in the review presented in

[37]. All of the aforementioned studies focus exclusively on sensible heating of solid storage objects.

Significantly fewer studies have investigated packed beds as latent heat storage systems using phase change materials. The large surface area to volume ratio of the packed bed arrangement can be used to enhance energy exchange when compared to PCMs contained in other less favorable configurations [20], making them potentially an excellent candidate for TES.

When considering packing arrangements for PCM-based packed bed TES, different encapsulation geometries have been considered, such as rectangular encapsulation, cylindrical encapsulation, spherical encapsulation etc..

The three-dimensional numerical work in [38] by Li et al. investigated structured packed beds of rectangularly encapsulated PCM. The work involved imposing an effective thermal conductivity on the PCM capsules to approximate the effects of melting. The findings from the work suggest that the PCM based packed bed device performed better than a comparable system which relied only on sensible heating, because of the increased energy density and constant temperature of the PCM capsules. The study also investigated the impact of the Reynolds number in the surrounding heat transfer fluid and concluded that both charging and discharging rates were faster with an increase in flow Reynolds number.

Li et al. [39] followed up their previous contribution with numerical work that investigated the performance of cylindrically encapsulated PCM in structured packed beds. Again, an effective thermal conductivity correction is applied to the PCM. The findings from the work similarly concluded that increased velocity in the surrounding heat transfer fluid led to faster charging and discharging rates. The work also investigated several different structured packing arrangements, and found that parallel packing in a tapered trapezoidal packed bed was superior to both parallel packing in a rectangular bed and interlaced packing in a rectangular bed in terms of charge and discharge rates. This increased performance was attributed to increased HTF velocity for the tapered trapezoidal arrangement.

Ming et al. [40] performed experimental and numerical work which investigated the performance of packed bed latent heat storage (LHS) devices containing spherically encapsulated PCM. The numerical work involved the use of a concentric dispersion packed bed model to estimate the



temperature distribution of capsules and surrounding heat transfer fluid without modelling melting, which produced results in moderate agreement with the physical experiment. The findings suggest that increases in the HTF inlet temperature and increases in HTF velocity through the packed bed both lead to increased performance of the packed bed device in terms of charge and discharge rate. The work also included a comparison to shell and tube thermal energy storage systems, and concluded that the charging and discharging rates in the packed bed configuration were 2-3 times faster, and the packed bed configuration was approximately 2 times more efficient.

Wei et al. [41] conducted numerical work for the purpose of comparing four different encapsulated geometries used for packed bed thermal energy storage. The work used corrections to estimate the temperature of the PCM components without modelling melting. In their comparison of spherical, cylindrical, plate, and tube encapsulation geometries, they concluded that the spherical capsules showed the best performance in terms of charge and discharge rates, because the space left between spheres allowed for a flow pattern that was favorable for heat transfer. They also remarked that spherical capsules were easier to accumulate within the packed bed tank.

The packing arrangements within packed bed thermal energy storage devices has been shown to greatly impact their performance. The numerical studies in [42-44] investigate the impact of packing structures and structured versus unstructured arrangements on the flow distribution and heat transport within packed beds. The findings in all three studies suggest that spherical particles with regular (structured) packing arrangements can reduce flow resistance of the surrounding HTF and improve convective heat transfer of the packed bed.

A review of different studies regarding the impact of packing arrangements is presented in [45]. The conclusions drawn by the authors suggest that while convective heat transfer is often superior in structured packing arrangements, random packing arrangements have more commercial application due to their simplicity, and reduced cost of filling the packed bed.

Xia et al. [46] numerically studied the effects of structured versus unstructured packing arrangements on heat transfer performance in packed beds with the same porosity ratio. Their findings suggest that the random packing arrangements had better heat transfer performance. The conclusions can be somewhat misleading however, because random packing arrangements typically have lower porosity than structured packing arrangements. Normalizing this porosity between structured and unstructured arrangements can lead to a different number of packing

elements, making the arrangements less comparable. The study involves applying an effective thermal conductivity to the PCM to approximate the temperature gradients resulting from natural convection within the melting spheres.

In terms of modelling the temperature gradients developed within the PCM spheres during melting, several methods are employed in the literature. One approach for modelling spherically encapsulated PCM packed beds is that employed by Erekan and Dincer [47]. A packed bed concentric dispersion model is used to model the packed bed, wherein only thermal conduction inside the solid spheres is considered. An empirical heat transfer coefficient correlation for approximating the temperature gradients within the PCM spheres is used.

Studies such as [48-49] by Arkar and Medved use a continuous solid phase model wherein the packing material is modelled as a continuous porous medium and not a matrix composed of individual spherical elements. This approach is used to generate a temperature distribution throughout the packed bed without modelling the melting and solidification processes within the spherical elements.

The continuous solid phase model is also used in [50-51] to investigate the performance of packed bed latent heat storage systems containing encapsulated phase change material. These studies investigated the influence of parameters such as the porosity ratio and HTF fluid velocity on the performance of the packed bed.

The most common approach used in modelling packed beds of spherically encapsulated PCM seems to be the continuous solid phase model, as used in [48-51]. This model is considered to be more convenient to implement than the concentric dispersion model used in [47], and almost as accurate, in the opinion of the authors conducting the review in [46].

All of the studies presented in the literature use some form of experimental correlations or empirical expressions to approximate the thermal gradients developed within the encapsulated PCM spheres. The studies avoid attempting to model the internal melting and solidification processes within the spherical packing elements of the packed beds, because of the massive computational cost associated to attempting to model internal melting and solidification, as reported in the review in [46].

It seems that the most significant obstacle associated with the modelling of the melting and solidification processes in packed beds of encapsulated PCM is the large computational resources associated with the modelling of phase change process in even a single sphere of the packed bed. Modelling the melting in an entire packed bed is therefore extremely computationally expensive, and not practical. However, the development and study of these devices would benefit greatly from some computationally efficient and practical method that is capable of accounting for the melting and solidification within the spheres.

There is a need for a computationally efficient method capable of modelling the behavior and performance of three-dimensional packed beds containing encapsulated PCM, and also accounting for the temperature gradients developed within the PCM that result from the natural convection that occurs during melting. The impact of these temperature gradients on the heat transfer rate into the PCM and consequent performance of the packed bed as a whole should be better understood in order to support the development of these devices.

Parametric studies investigating the impacts of packing arrangements, sphere diameters & materials, heat transfer fluid properties, and PCM properties would be much more practical to conduct accurately if a more efficient method existed. The development of these devices could be greatly accelerated/improved if such a method was introduced.

### **1.3 Motivation and Objectives**

The present study considers the numerical modelling of melting and solidification of PCM in encapsulated spheres contained within packed bed arrangements. While some published studies have attempted the numerical modelling of PCM encapsulated spheres within packed beds as discussed in the literature review, none seem capable of high-fidelity modelling of the internal melting and solidification behavior in a computationally efficient manner.

Most studies in the current literature impose some effective thermal conductivity or other approximate corrections on the PCM spheres in an effort to avoid actually modelling the internal melting and solidification processes, as they are known to be computationally expensive and

difficult to model. Many studies ignored the effects of the temperature gradients developed within the spheres entirely without any correction, resulting in relatively coarse and inaccurate results in terms of describing the performance of the packed bed as a whole.

The development of these packed beds of PCM encapsulated spheres for practical thermal energy storage purposes would benefit greatly from a computationally efficient method that is still capable of accurately modeling the behavior and performance of the packed bed, without resorting to coarse approximations or neglecting critical behaviors. The design and development of such devices could be supported by accurate numerical modelling of prospective designs, but doing so with currently established methods is not practical.

The objective of the presented study is to support the development of thermal energy storage devices containing packed beds of spherically encapsulated PCM.

This is to be accomplished via the development of a numerical modelling approach that is both highly accurate in terms of capturing the performance of the packed bed device without the need for approximations and corrections, and computationally efficient enough to actually be used for practical purposes.

In order to develop a working model for a packed bed consisting of PCM encapsulated spheres, the following objectives must be accomplished:

- 1) An initial model capable of describing the phase change process of a candidate phase change material must be established. This involves the selection of an appropriate PCM, and developing a model capable of accurately describing the phase change in terms of the melting time, and melting behavior of the PCM. As discussed in the literature review, there is no generally accepted method or procedure for producing such a model. Many of the key underlying details required to build a working model are poorly reported in the literature. Producing a model capable of describing the phase change process at all for a given PCM is a significant undertaking.

- 2) Accurately describing the phase change process involves the calibration of several key process tuning parameters, which are exclusive to the specific PCM and the geometry in which it is contained. These parameters must be parametrized and tuned until the model produces results which are comparable to those obtained in a physical experiment phase change process. The whole

model must be validated against a set of experimental results, in order to prove that the model is capable of accurately modelling the phase change process.

3) After a validated model is established for the geometry considered in a physical reference experiment, the model can be extended to other similar geometries of interest such as an encapsulated sphere. The model again needs to be tested in the new spherical geometry, to ensure that it is capable of producing reasonable results which are consistent with those presented in the literature for similar cases. Again, producing a model that is capable of accurately describing the phase change process of a PCM within a spherical enclosure is a significant undertaking in and of itself. The results obtained in applying the validated model to a spherical geometry should be discussed and understood.

4) Having successfully developed a model capable of describing the melting and solidification process within a single PCM encapsulated sphere, it can then be extended to the packed bed geometry of interest. At this point the packed bed itself needs to be modelled, with some chosen packing arrangement consisting of the spherically encapsulated PCM elements. Here, some method capable of reducing the computational expenditure associated to attempting to model phase change in all of the spheres in the bed must be introduced, in alignment with the original objective of developing such a method. The method must still be capable of incorporating the phase change model developed for the spherical geometry, while describing the performance of the packed bed as a whole in a computationally efficient manner. No such method has been presented in the literature. The limitations of the proposed method, and corrections which can be used to improve its accuracy in certain situations should be discussed and understood.

5) Having established a computationally efficient method for the treatment of the packed bed that can be used in conjunction with the high-fidelity phase change model for the single sphere, the method should then be demonstrated. Several cases should be run to demonstrate the viability of the method in producing accurate results in terms of the performance of the packed bed. In so doing, the method's ability to support the development of this type of thermal energy storage device for practical purposes is demonstrated.

The support of the development of this type of PCM based packed bed thermal energy storage device is made in alignment with the ultimate goal of increasing the efficiency of energy systems, in an effort to reduce environmental emissions and help combat climate change.

## 1.4 Thesis Layout

This section is intended to describe the layout of the thesis document in order to give the reader an idea regarding the flow of information.

Chapter 1 dealt primarily with the introduction of relevant concepts and relevant theoretical background information. The literature review provided in this chapter is performed with the goal of establishing the work that has already been done on the subject of numerically modelling packed beds of encapsulated PCM, and where the currently published body of literature is lacking in contributions or can be further refined. The motivation and objectives presented aim to address the deficiencies identified in the literature.

Chapter 2 deals with the model development. The numerical methods, physics, governing equations, and numerical implementation used to develop the model are introduced. The chapter further describes the process of calibrating and validating the model and key tuning parameters against a physical reference experiment, before applying the model to other geometries of interest.

Chapter 3 deals with the implementation of the model in packed beds of spherically encapsulated phase change materials. The way in which the calibrated model is adapted to the packed bed geometry is discussed, and the novel computationally efficient method for treating the packed bed is introduced. A correction for the method is also proposed. The method is then demonstrated via a parametric study, wherein several interesting properties such as sphere diameter and packed bed temperature are varied.

Chapter 4 includes a summary of the presented work, and some concluding remarks. Some recommendations for future research are made.

## Chapter 2

### 2. Model Development

The model to be developed is intended for the ultimate purpose of modelling the performance of packed beds of spherically encapsulated PCM. An initial model must first be constructed in order to validate the numerical formulations, and various methods and approaches used to model PCM phase change processes. This model development section includes an explanation of the general, geometry-independent governing equations, physics, and numerical procedures used to describe the melting and solidification of phase change material. It is followed by applying these general principles to a specific two-dimensional cylindrical geometry, for which a physical experiment had been conducted. A comparison between the results from the numerical simulation and this physical reference experiment is performed in order to validate the model, and calibrate some of the key tuning parameters. The validated model is then applied to a single spherical geometry of interest, before finally being applied to a packed bed containing many spheres. A graphical illustration of the model development progression is provided in figure 2.1.

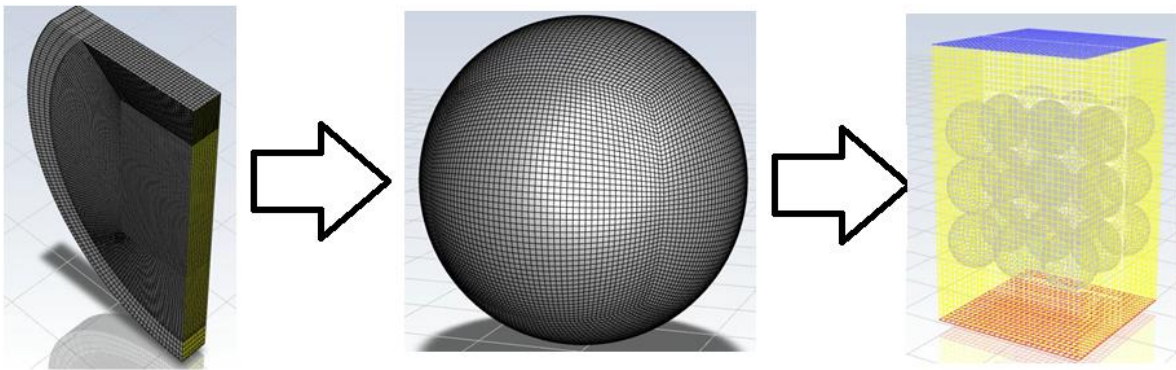


Figure 2.1 - Diagram of the model development progression.

## 2.1 General Model

This section includes a description of the general, geometry independent governing equations, physics, and numerical procedures used to describe the melting and solidification processes of phase change material.

### 2.1.1 Numerical Formulation

The flow during melting and solidification is considered to be laminar, incompressible, and Newtonian. The velocity magnitudes of molten liquid PCM developed within melting processes have been shown to be of low magnitude, and well within the laminar region [20-27]. The solid and liquid states of PCMs are virtually incompressible, and their fluid behavior is Newtonian [7-10]. The governing equations to be solved for melting and solidification problems are the conservation of mass, the conservation of momentum, and the conservation of energy.

The mass equation is given as [52]:

$$\frac{\partial \rho}{\partial t} + \nabla \cdot (\rho \vec{v}) = 0 \quad (2.1)$$

where  $\rho$  is the density,  $t$  is time, and  $\vec{v}$  is the velocity. The leading term on the left-hand side of Eq. 2.1 is only required if changes in density are resolved during phase change or sensible heating.

The momentum equation is given as [52]:

$$\frac{\partial}{\partial t} (\rho \vec{v}) + \nabla \cdot (\rho \vec{v} \vec{v}) = -\nabla p + \nabla \cdot \tau + \rho \vec{g} + \vec{F} + S_m \quad (2.2)$$



where  $p$  is the static pressure,  $\tau$  is the stress tensor,  $\vec{g}$  is the gravitational acceleration,  $\vec{F}$  are the external body forces, and  $S_m$  is a momentum sink associated to the characterization of the “mushy” interface region between the fluid and solid phases during melting and solidification.

The energy equation is given as: [52]

$$\frac{\partial}{\partial t}(\rho H) + \nabla \cdot (\rho \vec{v} H) = \nabla \cdot (k \nabla T) + S_e \quad (2.3)$$

where  $H$  is the enthalpy, and  $S_e$  is an energy source term.

## 2.1.2 Buoyancy and Volumetric Expansion

Typical phase change materials undergo moderate volumetric expansion during the transition between the solid and liquid phases, and additional minor volumetric expansion during sensible heating [12].

Detailed modelling of the volumetric expansion in the context of rigid encapsulated spherical containers is challenging, as the container must be capable of supporting the expansion of the PCM in some way. It is highly impractical to assume that the encapsulating shell material is flexible, and capable of accommodating this expansion simply by means of the walls of the PCM cavity expanding to allow for an increase in volume. Some approaches to overcome this challenge are presented in the literature.

In many of the physical experiments conducted, the volumetric expansion of the PCM is accommodated by allowing the ejection of the expanding PCM or some other placeholder fluid such as air through some orifice in the vessel [22-23,25,54]. This usually necessitates only the partial initial filling of the interior spherical cavity with PCM, and allowing the rest of the volume to be occupied by the placeholder fluid (usually air). This is what is done in the majority of

physical experiments considered in the literature review [22-23,25], and also in the physical reference experiment used to calibrate the present model [54].

In numerical studies, modelling the ejection of such a placeholder fluid and introducing some type of ejection orifice in the walls of the container can needlessly complicate the model. A volume of fluid method would have to be implemented to resolve the fluid-fluid interface between the PCM and placeholder fluid, and additional boundary conditions would have to be imposed to treat the outlet orifice in the container.

Instead of this, the modelling of this volumetric expansion can be approached in several different ways. For numerical studies concerning constrained melting, the volumetric expansion is ignored entirely by treating the PCM density as constant in both phases [20-27]. This method is simplest in terms of implementation since PCM density can be treated as constant for both the solid and liquid phases, and thus the encapsulating shell does not need to be modelled in a way that is capable of supporting the volume change during the phase transition.

Of significance however is that the melting processes of phase change materials is highly dependent upon buoyancy induced convection that occurs within the melted region, as reported in [21-27]. This buoyancy occurs as a result of temperature gradients (and hence density gradients) that develop as a result of heat transfer. Proper modelling of this buoyancy effect is critical to accurately capturing the underlying physics associated with the PCM melting and solidification processes.

So, if the PCM density is being treated as constant in order to avoid modelling a container capable of supporting volumetric expansion, some other method must be employed in order to capture the effects of the buoyancy induced natural convection within the melting.

To approximate local density variations with respect to the local temperature, the Boussinesq approximation is used whereby the density of the PCM is treated as constant everywhere except for the buoyancy term in the momentum equation. Buoyancy is then modelled by means of a thermal expansion coefficient, which describes the change in the reference density proportional to the difference between the local temperature and the reference temperature.

The Boussinesq approximation has the form [52]:

$$(\rho - \rho_0) \approx -\rho_0 \alpha (T - T_0) \vec{g} \quad (2.4)$$

where  $\rho_0$ ,  $T_0$ , are the reference density and temperature, and  $\alpha$  is the thermal expansion coefficient.

The Boussinesq approximation is capable of providing a reasonable approximation of the buoyancy forces within a fluid, as long as the temperature variations with respect to the reference temperature are relatively small. Such is the case with the temperature gradients developed within melting PCMs.

Carefully selecting the thermal expansion coefficient  $\alpha$  is quite important, however. The value of this thermal expansion coefficient will directly influence the degree of volumetric expansion the PCM experiences, and thus will greatly influence the buoyancy driven natural convection within the melt.

As has been shown in the literature [23-27], correctly modelling this behavior is of fundamental importance in order to produce numerical results which match most closely with physical experiments.

Unfortunately, the value of this thermal expansion coefficient is usually not provided on PCM material data sheets, and is rarely reported in the literature as a material specific property of a PCM. The determination of an appropriate value is, therefore, left to those constructing the numerical model. The process of calibrating and tuning this parameter for the present model is described in section 2.2.4.

### **2.1.3 Phase Change Modelling**

The model must also be capable of modelling the phase change process between the solid and liquid state of the phase change material, as the fundamental purpose of the model is to study solidification and melting of PCM.

Melting and solidification problems are also referred to as moving boundary problems. This is because the position of the interface between the solid and liquid phases is constantly changing with respect to time, as the melting or solidification process progresses. Tracking the position of this interface with respect to time is an important aspect of correctly modelling a melting and solidification problem. The position of this interface is effectively a description of the shape or profile of both the solid and liquid phase in a melting or solidification problem, and can often be of practical importance. A solution to this type of problem was first proposed by Stefan in 1881, in his study of ice cap formation in polar regions [19]. In his work, Stefan attempted to model the position of the solid-liquid interface of the ice using a one-dimensional at constant heat flux conditions.

A method referred to as enthalpy-porosity approach is commonly used for modeling the melting and solidification processes in phase change materials [20-27]. This method is not limited to strictly PCMs, but applicable to any material undergoing phase change. In the enthalpy-porosity approach, the position of the interface between the solid and liquid phases of the material is not being tracked explicitly. There is no parameter being stored regarding the position of this interface with respect to some coordinate system within the domain. Instead, a property called the liquid fraction, which indicates the percentage of a given cell volume that is in the liquid phase, has a value stored for each cell in the domain. The value of the liquid fraction is updated at each solver iteration and each time interval based on an enthalpy balance. [52]

Material in the domain which is above the melting temperature is considered to be entirely liquid, and material in the domain which is below the melting temperature is considered to be entirely solid, per the following equations:

$$\beta = 0 \text{ if } T < T_{transition} \quad (2.5a)$$

$$\beta = 1 \text{ if } T > T_{transition} \quad (2.5b)$$

where  $\beta$  is the liquid fraction, and  $T_{transition}$  is the temperature at which the PCM undergoes solidification or melting.

It is possible for cells which are at the transition temperature of the PCM to contain both liquid and solid phases. Physically this corresponds to a material which is undergoing latent heat transfer, and is thus held at the phase transition temperature while any incoming or outgoing thermal energy produces a change of state and not a temperature increase. These cells are referred to as the mushy region (or zone) of the melting PCM.

The mushy zone is an interface region between the fluid and solid regions where both liquid and solid phases exist, characterized by a value of  $\beta$  between 0 and 1. Due to the physical nature of this region, which includes stationary and moving dendritic structures saturated by liquid, the mushy zone is modeled as a "pseudo" porous medium in which the porosity decreases from 1 (pure liquid) to 0 (pure solid) as the material solidifies and vice versa as the material melts.

To determine the liquid fraction of the PCM in cells at the melting temperature, the latent heat content of each cell is computed from: [52]

$$\beta = \frac{H_L}{L} \quad (2.6)$$

where  $H_L$  is the latent heat content at the current time interval, and  $L$  is the latent heat capacity of the material.

This mushy zone region also contributes as a momentum sink in the momentum equation, given its reduced porosity as a function of the liquid fraction. Physically, this corresponds to fluid coming into contact with the mushy region being slowed down. Because of the influence on the liquid fraction on the fluid velocity, the liquid fraction influences all other governing equations which contain velocity terms. The momentum sink due to the reduced porosity in the mushy zone takes the form [52]:

$$S_m = -\frac{(1-\beta)^2}{(\beta^3+\epsilon)} A_{mush}(\vec{v}) \quad (2.7)$$

where  $A_{mush}$  is the mushy zone constant, and  $\epsilon$  is a small number ( of order  $1 \times 10^{-20}$ ) to avoid division by 0 in the solid region.

The value of the mushy zone constant is, like the thermal expansion coefficient, extremely important for accurate modelling of melting and solidification. The value of this term can directly influence the profile of the solid-liquid interface, and also the strength of convection within the melting PCM. This material-specific parameter is not usually reported in the literature, and never included on PCM material data sheets because it is a nonphysical property used only for the purpose of simulation. The process of calibrating and tuning this parameter for the present model is described in section 2.2.4.

## 2.1.4 Numerical Procedure

ANSYS Fluent [53] is used to solve the system of transport equations described above. The pressure-based solver is used, as this solver must be used when enabling the solidification and melting model within Fluent. Transient simulations are conducted to study melting and solidification over a period of time, as this is the fundamental purpose of the study. Gravity is enabled to permit buoyancy to drive fluid motion within the liquid phase of the melt. The value of the gravitational acceleration at the surface of the earth is used. Higher-order schemes are used wherever possible, with the exception of first-order upwinding used to model advection in the momentum equation. While this necessitated a higher grid resolution to obtain reasonable results, it was the only scheme that produced realistic results in and around the mushy region. Higher-order momentum schemes were found to reduce solver stability and often resulted in solver divergence. Furthermore, the position of the solid-liquid interface when using higher order momentum schemes was not in good accordance with the physical experiment, which suggested possible issues at the interface between the solid and fluid regions.

A summary of the numerical methods used are given in Table 2.1.

Table 2.1 – Summary of numerical methods used.

<b>Method</b>	<b>Value or Condition</b>	<b>Explanation</b>
Pressure-Velocity Coupling Scheme	SIMPLE	Used in literature
Gradient	Least Squares Cell Based	Most accurate method, requires less computational effort than node based.
Pressure	Second Order	Higher order scheme
Momentum	First Order Upwind	Instability issues with higher order
Energy	Second Order Upwind	Higher order scheme
Transient Formulation	Second Order Implicit	Higher order scheme

## **2.2 2D Cylindrical Model**

This section is dedicated to the implementation of the model for a specific quasi-two-dimensional cylindrical geometry, for which there is a physical experiment to use as the basis of validation. A brief description of the geometry and materials used in the physical experiment conducted by Teather and Siddiqui [54] is provided. The mesh generation approach used to spatially discretize a domain which replicates this physical experiment is then discussed. A description of the boundary conditions used to replicate the conditions of the physical experiment is provided. The process of calibrating the model to produce results closer to the physical experiment is then discussed, with special emphasis on the calibration of several key tuning parameters, namely the thermal expansion coefficient and mushy zone constant. Grid and timestep independence testing is conducted to ensure that the results are both spatially and temporally independent. A final comparison between the numerical model and physical experiment is conducted, to demonstrate that the model has been validated and is capable of producing results which are consistent with the real physical melting process.

## 2.2.1 Geometry & Materials Description

In this section, a brief description of the geometry and materials used in the physical experiment conducted by Teather and Siddiqui [54] is provided

### *Geometry*

A schematic representation of the physical reference experiment is shown in Figure 2.2. The geometry is comprised of a quasi-two-dimensional cylindrical cavity with an inner diameter of 70 mm (2.75 inches), 12.7mm (0.5 inches) in depth, and a wall thickness of 6.35 mm (0.25 inches).

The walls of this cylindrical cavity are made of acrylic. The heating to the cavity is provided via the radial wall which is exposed to a water jacket which is maintained at a constant temperature. The front and back faces of the cavity are well insulated to minimize heat transfer through these faces, and thus to make the experiment quasi two-dimensional. Rubitherm RT26 is used as the phase change material, which is mostly filled inside the cavity. A small air gap is left at the top of the cavity to facilitate thermal expansion of the PCM (see Fig. 2.1). This air is allowed to escape through a small orifice in the wall of the cylinder during the volumetric expansion of the PCM. The initial location of the PCM-air interface (i.e. when the PCM is in the initial solid state) is approximately 24 mm (0.95 inches) above the cavity center point. The data from this experiment are recorded in the vertical midplane, approximately 12.35mm (0.25 inches) inward from either end of the cylindrical cavity.



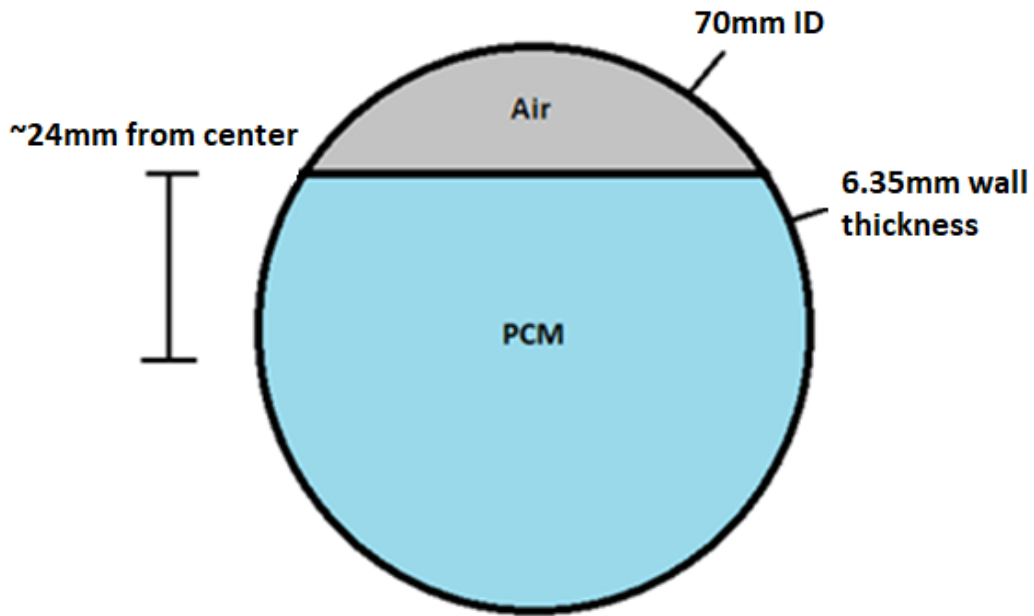


Figure 2.2 - Schematic of the cylindrical cavity used by Teather and Siddiqui [54].

### ***Material Properties***

The phase change material considered in the physical reference experiment, and thus in the computational study, is Rubitherm RT26, the material properties of which are listed in Table 2.2.

Table 2.2 – RT26 PCM material properties [55,56].

Density	880 kg/m <sup>3</sup>
Specific Heat Capacity	2000 J/kg-K
Thermal Conductivity	0.2 W/m-K
Viscosity	0.00359 kg/m-s
Latent Heat Capacity	180,000 J/kg
Transition Temperature	299K

The properties of the acrylic wall material used are presented in Table 2.3.

Table 2.3 – Acrylic material properties [57].

Density	1190 kg/m <sup>3</sup>
Specific Heat Capacity	1470 J/kg-k
Thermal Conductivity	0.2 W/m-K

### 2.2.2 Mesh Generation Approach

This section is included to discuss the mesh generation approach used to spatially discretize a domain which replicates the physical experiment in the above section. The computational meshes for the cylindrical cavity were generated using ANSYS meshing software [53]. The mesh generation strategy involved the generation of a structured o-grid hexahedral mesh, as illustrated in figure 2.3:

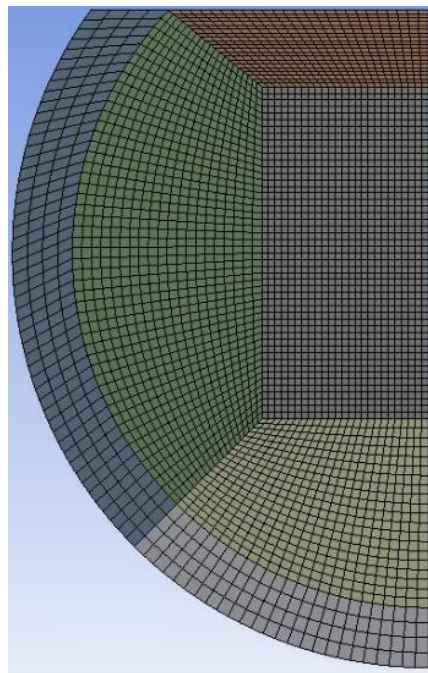


Figure 2.3 - Illustration of hexahedral O-grid mesh structure for phase change material and acrylic wall.

Symmetry axes are taken advantage of where possible, including the midplane vertical axis and the mid axial plane. This allowed for a significant reduction in mesh elements, as only a quarter of the physical geometry needed to be modelled. This was possible because the experimental results showed symmetry around these planes.

The o-grid structure allowed for the generation of a relatively uniform and orthogonal cell topology throughout the domain. No clustering of cells towards any of the boundaries was considered, because the position of the solid-liquid interface moves throughout the PCM domain during the phase change process. Uniform spacing throughout the entire domain is therefore necessary in order to maintain a consistent and uniform grid resolution to simulate this interface at any point during the phase change process.

The hexahedral o-grid structure was found to be quite important in order to facilitate convergence of the solver, and produce accurate solutions, especially since a first-order scheme was used in the momentum equation. This involved the generation of central half square mesh region, surrounded by quarter circle mesh regions on all sides. The number of grid divisions on each circumferential side of the quarter circle mesh regions matches the number of divisions on the central half square, allowing for the uniform hexahedral topology to be generated.

Unstructured tetrahedral meshes which were considered during initial model development showed less accuracy in terms of tracking the position of the solid-liquid interface throughout the phase change process, and generally involved more cells than with a structured mesh.

The acrylic shell component was modelled a few cells thick, to allow for the formation of a temperature gradient within this wall early in the simulation. The air gap region at the top of the PCM cavity is not included in the model. Instead, the interface between the air and the PCM is modelled as a wall boundary, with appropriate boundary conditions.

### **2.2.3 Boundary Conditions**

A description of the boundary conditions used to replicate the conditions of the physical experiment is provided.

The boundary conditions are summarized in Table 2.4.

Table 2.4 - Summary of boundary conditions imposed on the quasi two-dimensional cylinder for melting and solidification simulations.

<b>Location &amp; Type</b>	<b>Boundary Condition</b>
Outer Wall Exterior surface	-Constant temperature thermal condition
Outer Wall Interior surface (PCM side)	-Coupled thermal condition -No slip momentum condition
Air Boundary (above the PCM)	-Convection thermal condition -Zero Shear, slip wall condition
Midplane Wall	Symmetry
Front Face	-Adiabatic thermal condition -No slip condition
Rear Face (axial midplane)	Symmetry

A constant temperature thermal condition is applied to the Outer Wall Exterior surface of the acrylic shell, to approximate the presence of the water jacket used to maintain a constant temperature condition in the physical experiment.

The Outer Wall Interior surface of the acrylic shell is set to coupled thermal conditions, to allow for the natural formation of a temperature gradient through the wall and into the PCM cavity. This surface is also set to a no slip momentum condition, as this surface is in contact with the PCM in the liquid phase during the melting process.

The interface between the PCM and the air (Air Boundary) is set to a convection thermal condition to approximate the heat transfer that occurs between the PCM and the air pocket at this interface in the physical experiment. A zero-shear, slip condition is applied at this boundary, to approximate the free-surface condition.

The Front Face of the domain is given an adiabatic thermal condition, as this surface is well insulated to mitigate heat losses during experiments. A no-slip condition is also applied as this surface it is in contact with the PCM in the liquid phase during the melting process.

Finally, symmetry conditions are imposed on the Midplane Wall and the Rear Face. Experimental results (carried out over the full cavity) showed symmetric velocity and temperature fields about these mid vertical planes.

The locations of these boundary conditions with respect to the physical geometry are shown in figure 2.4.

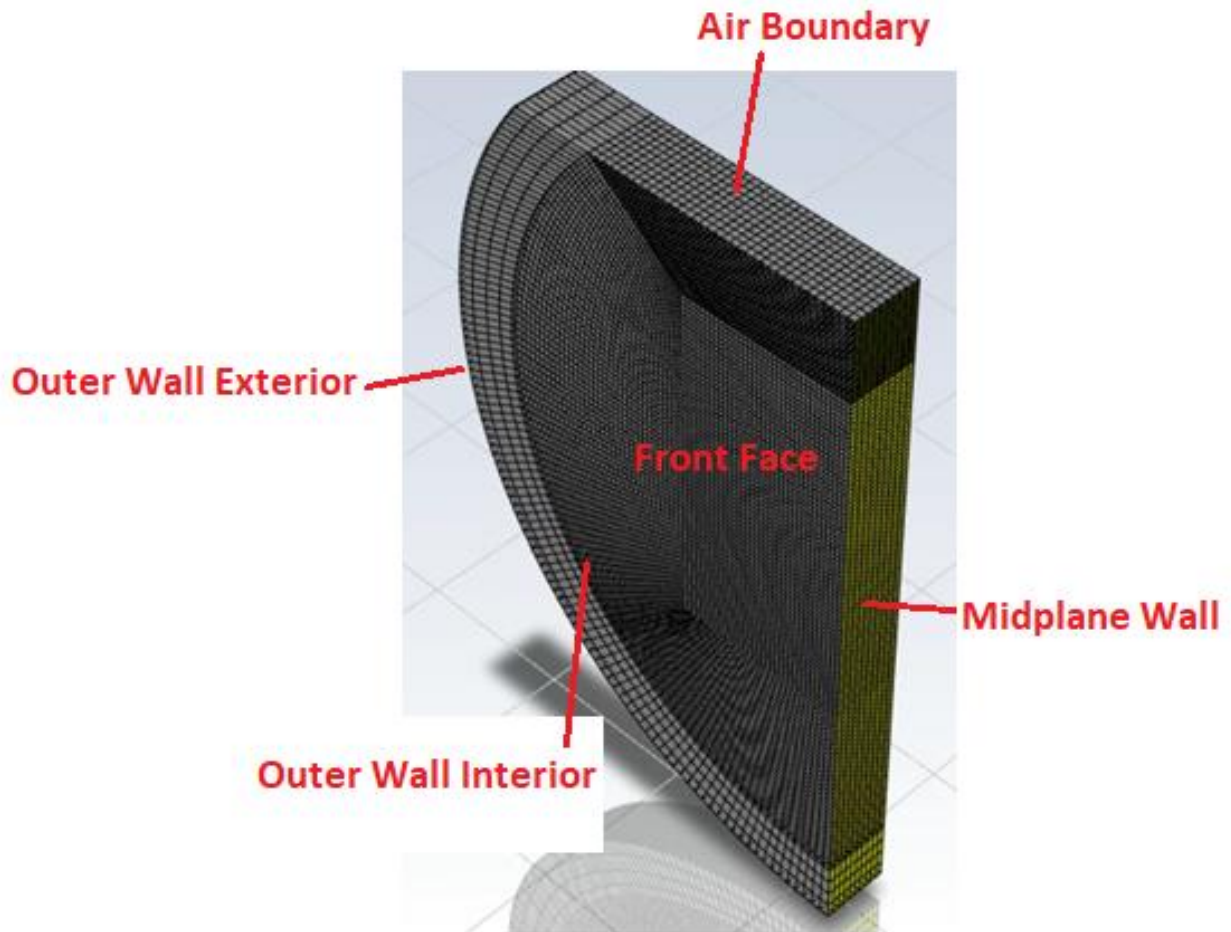


Figure 2.4 - Boundary condition locations shown on the quasi two-dimensional cylinder geometry.

## 2.2.4 Grid & Timestep Independence Testing

Grid and timestep independence testing is conducted, to ensure that the results are both spatially and temporally independent. For the purpose of determining grid and timestep independence, the melting time for different grid resolutions and different timestep sizes is considered as the point of comparison. The cases considered are allowed to run up to 20 iterations at each time step, or until the value of the residuals reach the specified convergence criteria of  $10^{-3}$ . An initial timestep size of 1 second was used in the grid independence tests, though this timestep size is varied in the timestep independence testing.

The cases were run until the PCM was considered to be fully melted. The value of the volume-averaged liquid fraction is monitored at 60 second intervals throughout the simulation. When the fully melted condition is achieved (100% volume average liquid fraction), the melting time is reported as the midpoint of the interval in which the fully melted condition appeared. Consequently, the reported melting time is +/- 30 seconds of the actual melting time.

The cases were initialized at a uniform temperature of 293K throughout the entire domain, in order to approximate the  $\sim 20^{\circ}\text{C}$  initial temperature of the experimental case. At this condition, the entire PCM is in the solid phase (0% liquid fraction), 6K below the transition temperature. Sensible heating occurs in the initial stages of the simulation, until the PCM reaches the melting temperature, at which point melting begins. This sensible heating period is included as part of the overall 'melting time' reported in both the physical experiment and the simulation.

The constant temperature thermal boundary condition used for the outer wall exterior surfaces is 306K, which replicates the  $33^{\circ}\text{C}$  temperature condition applied by the water jacket on these exterior surfaces in the physical experiment.

The grid and timestep independence test results for this case are shown in Tables 2.5 and 2.6, respectively.

Table 2.5 - Grid independence test results for melting of PCM in a quasi two-dimensional cylinder.

<b>Property\Grid Resolution</b>	<b>40,000 cells</b>	<b>155,000 cells</b>	<b>312,000 cells</b>
Melting Time (s)	23,950	23,820	23,550
% difference	-	0.54%	1.133%

Table 2.6 – Timestep independence test results for melting of PCM in a quasi two-dimensional cylinder.

<b>Property\Timestep Size</b>	<b>0.5 sec</b>	<b>1 sec</b>	<b>1.5 sec</b>
Melting Time (s)	23,950	23,950	23,890
% difference	0	0.25%	-

The solution was deemed to be grid independent at the 40,000-cell resolution at time step sizes under 1 second, as further refinement led to no significant change in the prediction of melting time for the PCM.

## 2.2.5 Model Calibration

Calibration of the melting-solidification model is necessary to capture both the shape of the solid-liquid interface and the time required for full melting/solidification. Accurate modelling of these processes requires calibration of the mushy zone constant and the thermal expansion coefficient, both of which vary depending upon thermophysical properties of the PCM. Hence, validation against physical measurements during phase change is required in order to tune these parameters.

### *Thermal Expansion Coefficient*

For the Boussinesq approximation to generate buoyancy forces related to local temperature changes, a thermal expansion coefficient for the PCM material must be specified - (See Eq. 2.4). The thermal expansion coefficient is not typically specified on PCM technical data sheets, and is poorly reported in the literature. While this coefficient is a material specific property of the PCM material, in the simulation of melting, it is used to characterize the entire convection process – and has a significant impact on the melting time of the PCM. To this end, a higher value of the thermal expansion coefficient produces stronger buoyancy forces, stronger convection currents, and thus reduced melting times, while a low value produces the opposite. Because the influence of the convective behavior is so important in correctly characterizing the overall behavior of the PCM during melting, the selection of an appropriate value for the thermal expansion coefficient is of great significance.

It is appropriate to think of the thermal expansion coefficient as a coefficient that needs to be adjusted and calibrated by the user constructing the model on a PCM & geometry specific basis. In the present case, the calibration of the thermal expansion coefficient is conducted by comparing simulations of melting to similar experimental data. The melting behavior in terms of the position of the solid-liquid interface, and melting time of the PCM showed moderate sensitivity to the value of the thermal expansion coefficient.

The ranges of values considered for the thermal expansion coefficient for the present study were of the order between  $10^{-2}$  and  $10^{-6}$ . Use of values which were far removed from the final, calibrated



value produced melting results which showed disagreement with the physical reference experiment. Figure 2.5 contains some contour plots of the liquid fraction at different moments in the melting process which were obtained using suboptimal values for the thermal expansion coefficient.

The final calibrated value used in this study for the RT26 PCM is 0.0005, which provided the best agreement with the experimental data for both the melting time and the shape/orientation of the solid-liquid interface with respect to time.

For the purpose of numerical simulations, the thermal expansion coefficient should be considered a parameter which characterizes the whole convective process, and less so as a physical property of the material. The tuning of this parameter is performed more so in the context of tuning the degree of convection that occurs during the melting, and not strictly related to just the degree of volumetric expansion that the material undergoes during a temperature change. It is in this sense a process tuning parameter, not a material property, for the purpose of numerical simulations.

### ***Mushy Zone Constant***

The solidification and melting model also requires the specification of a mushy zone constant in order to calculate the momentum sink in partially melted regions - (cells where the liquid fraction is between 0 and 1, Eq. 2.7). Again, the value of this parameter is poorly reported in the literature, as it is a material specific property. It is never included on PCM material data sheets, because it is not a physical property, but rather a parameter that is used only for the purpose of simulation.

The mushy zone constant impacts the amplitude of the velocity damping in the semi-porous mushy region of the PCM material and, therefore, impacts the shape of the interface during the melting or solidification processes. The higher the value, the faster the velocity of the material becomes zero as it solidifies. This parameter was also found to be inversely proportional to the degree of convection that occurs within the melting. Higher values were found to suppress convective behavior, and promote longer melting times as a result of reduced convective heat transfer.

It is again appropriate to think of the mushy zone constant as a parameter that needs to be adjusted and calibrated by the user constructing the model on a PCM & geometry specific basis.

Similar to the thermal expansion coefficient, the calibration of the mushy zone constant in the present case is conducted by comparison of simulations to experimental data. Again, the melting behavior in terms of the position of the solid-liquid interface, and melting time of the PCM showed moderate sensitivity to the value of the mushy zone constant.

The ranges of values considered for the thermal expansion coefficient for the present study were of the order between  $10^4$  and  $10^7$ . Use of values which were far removed from the final, calibrated value produced melting results which showed disagreement with the physical reference experiment. Figure 2.5 contains some contour plots of the liquid fraction at different moments in the melting process which were obtained using suboptimal values for the mushy zone constant.

The final calibrated value use in this study for the RT26 PCM is 100,000 which provided the best agreement with the experimental data.

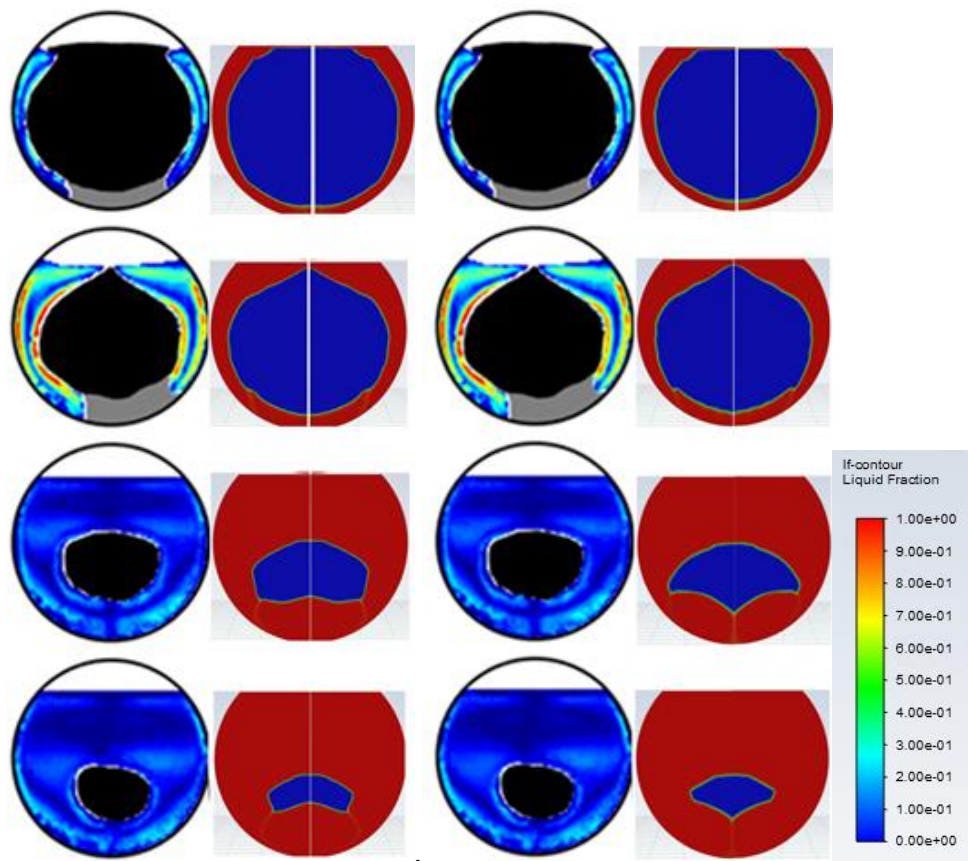


Figure 2.5 – Simulated contours of liquid fraction (right columns) at different moments in the melting process compared to the reference physical experiment [54] (left columns).

The results show disagreement with the experimental case, as a result of suboptimal values being used for the thermal expansion coefficient and mushy zone constant parameters.

### **2.2.6 Model Validation**

Experimental results from Teather and Siddiqui [54] are used for model validation. The melting time in the experiment (including sensible heating of the PCM from the initial 20°C room temperature to the melting temperature) is reported as approximately 22,170 seconds.

The melting time in the final, calibrated, numerical simulation (including sensible heating of the PCM from the initial 20°C room temperature to the melting temperature) was found to be approximately 23,950 seconds – within 7.5% of the experimental results.

The melting time is a bulk comparison parameter and hence, alone, is not an accurate indicator of the true transient phase change process and the associated spatio-temporal movement of the solid-liquid interface. Therefore, it is necessary to compare the transient behavior of the solid-liquid interface between the experimental and simulated results to demonstrate that the numerical model is indeed accurately simulating the underlying physical processes. The profiles of the solid-liquid interface at various stages during melting from simulation and experimental results are compared and shown in figure 2.6.

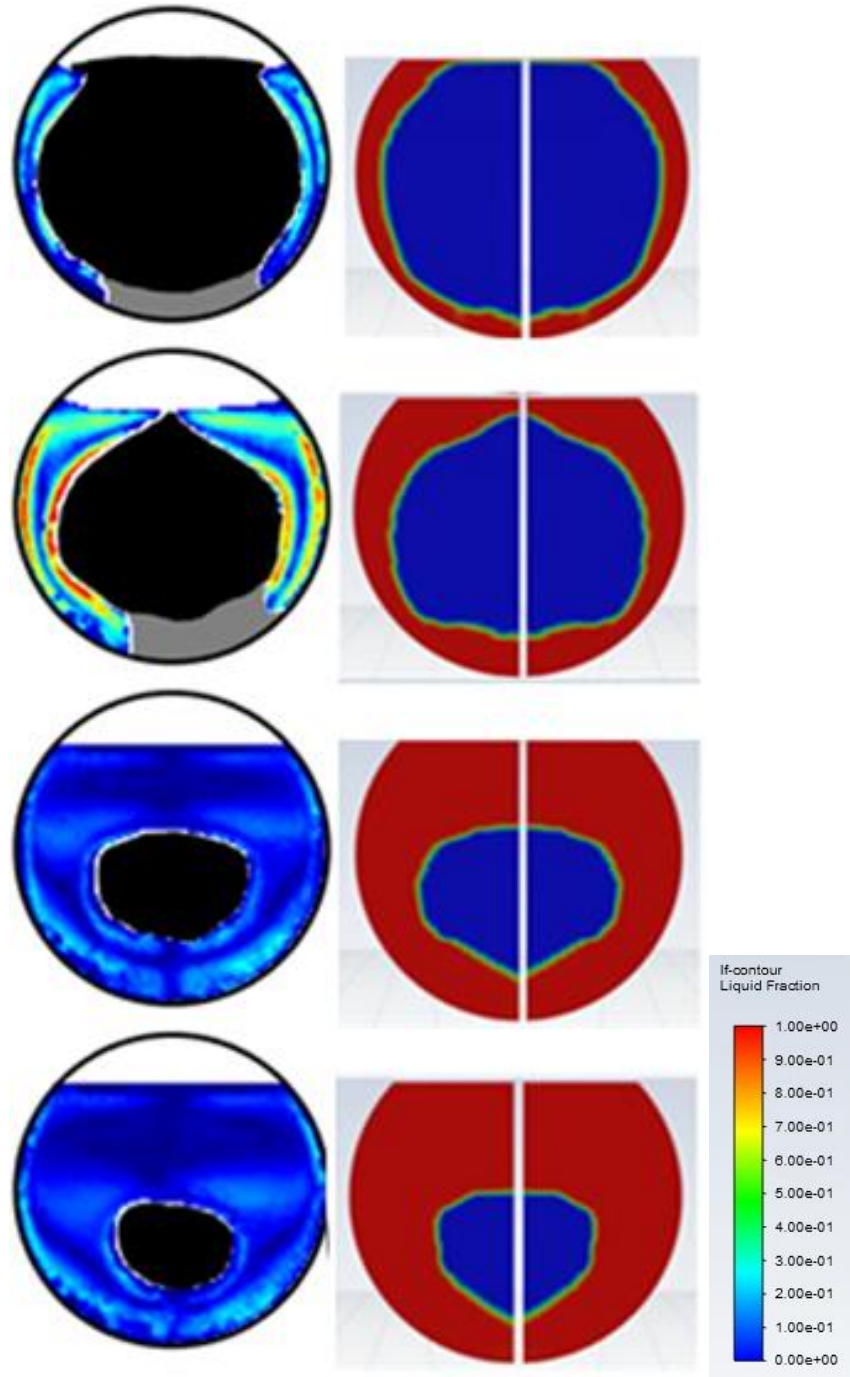


Figure 2.6 – Solid-liquid interface comparison during melting for two-dimensional cylinder  
 Left = Reference experiment [54], Right = Numerical model

The transient profiles of the simulated solid-liquid interface presented in figure 2.6 show good agreement with the experimental profiles, implying that the present model accurately simulates the phase change process in a cylindrical geometry for the specific PCM considered

## 2.3 Spherical Model

The model in the preceding section is validated for a circular geometry subjected to heat transfer through the radial wall. The encapsulated PCM in a sphere experiences similar thermal boundary condition and similar thermo-physical interactions, hence, the validated model is well-suited to simulate phase change process in a spherical geometry. In this section the implementation of the model for a three-dimensional spherical geometry is discussed. A brief description of the geometry and materials used is provided. The mesh generation approach used to spatially the spherical domain is then discussed. A description of the boundary conditions used to model a reasonable phase change process are then provided. Grid and timestep independence testing is conducted to ensure that the results are both spatially and temporally independent.

### 2.3.1 Geometry & Materials Description

In this section, a brief description of the geometry and materials used for the spherical case is provided.

#### *Geometry*

The geometry considered is a three-dimensional sphere of 22mm in diameter. The shell of the sphere has a 1mm radial thickness, resulting in an inner PCM cavity of 20mm in diameter. A 2D diagram of the considered spherical geometry is provided in figure 2.7.

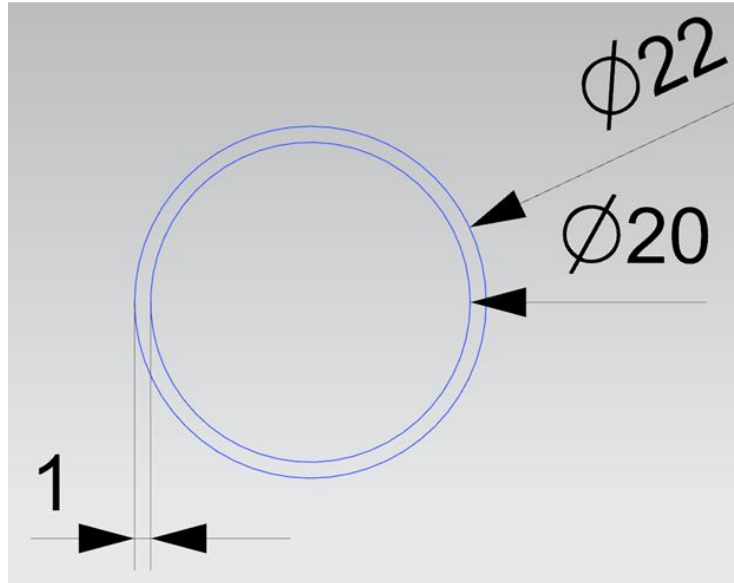


Figure 2.7 - 2D Diagram of the considered spherical Geometry (dimensions in mm).

### ***Materials***

The materials used in the spherical case for the composition of the spheres are the same as those used in section 2.2 for the cylindrical case.

The phase change material used is the Rubitherm RT26 PCM, with material properties as indicated in Table 2.2 in section 2.2, and in Appendix A6. The thermal & physical properties of the PCM are again treated as constant and independent of temperature and state, with the exception of the density of the liquid which is treated using the Boussinesq approximation. The material used for encapsulating shell is the same acrylic material as before, with material properties as indicated in Table 2.3 in section 2.2. As before the properties of the acrylic are treated as constant and independent of temperature.

### **2.3.2 Mesh Generation Approach**

The computational meshes for the single sphere were generated using Pointwise V18.3R1 64-bit meshing software [58].

The meshing strategy again involves the generation of a structured o-grid style hexahedral mesh, but now for a three-dimensional sphere with a diameter of 20 mm, as shown in figure 2.8:

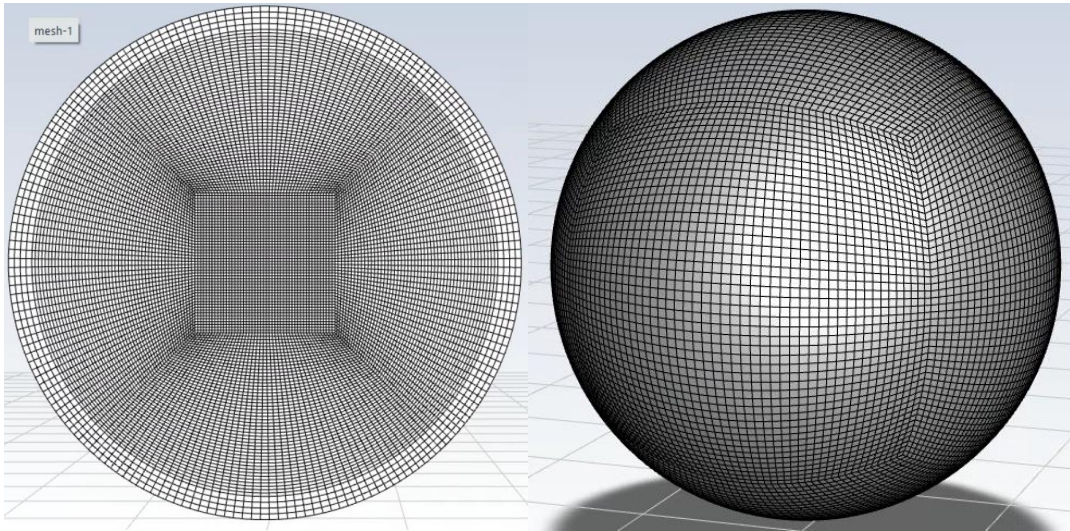


Figure 2.8 - Hexahedral O-grid mesh structure for the single encapsulated sphere case

The o-grid structure again allowed for the generation of a relatively uniform and orthogonal cell topology throughout the domain. As in the cylindrical mesh, no clustering of cells towards any of the boundaries are considered, because the position of the solid-liquid interface moves throughout the PCM domain during the phase change process. Uniform spacing throughout the entire domain is therefore necessary in order to maintain a consistent and uniform grid resolution to simulate this interface at any point during the phase change process.

Because the hexahedral o-grid structure was found to be quite important in order to improve convergence of the solver for the cylindrical case, the same structure is employed for the three-dimensional sphere. In the case of the sphere, this involved the generation of central cube mesh region, surrounded by one-sixth sphere mesh regions on all sides. The number of grid divisions on each circumferential side of the one-sixth sphere mesh regions matches the number of divisions on the central cube mesh region, allowing for the uniform hexahedral topology to be generated.

In order to model the spherical curved surfaces, an initial cube shaped group of points and connectors was projected out onto a spherical reference shape. Specifying the diameter of a sphere and then projecting the initial cube shaped mesh out onto it was found to be much more straight



forward to implement than trying to specify the spatial coordinates of different points on the curved spherical faces.

The acrylic shell component was again modelled to be a few cells thick, to allow for the formation of a temperature gradient within this wall.

In the case of the three-dimensional sphere, the entire spherical domain is spatially discretized, with no symmetry axis being taken advantage of. Though the initial inclination was to consider a smaller fraction of the total sphere as the computational domain, it was found that the results produced using a fraction of a sphere were substandard. The reasoning for this was thought to be associated to the fact that the complex three-dimensional behavior in the spherical case was not being correctly captured when using a domain which represented only a fraction of the sphere, even when symmetry conditions were used on the cut planes. This is consistent with what is reported in the literature regarding three-dimensional models [23-24].

The general consensus seems to be that full three-dimensional models provide better results, a finding which is confirmed by the present study.

### 2.3.3 Boundary Conditions

In this section, a description of the boundary conditions used to model a reasonable phase change process are provided.

A summary of the boundary conditions imposed on the spherical mesh are presented in table 2.7.

Table 2.7 - Summary of boundary conditions imposed on the three-dimensional sphere for melting simulations.

Location & Type	Boundary Condition
Sphere Outer Wall	-Constant temperature thermal condition
Sphere Inner Wall (PCM side)	-Coupled thermal condition -No slip momentum condition



For the sphere outer wall boundary, a constant temperature thermal condition is imposed, as was done in the two-dimensional cylindrical case.

At the sphere inner wall boundary, a coupled thermal condition is imposed to allow for the temperature at this interior surface to develop naturally as a result of heat transfer through the acrylic wall and into the PCM. A no slip momentum condition is also imposed on this inner surface, as this surface is in contact with the liquid PCM during the melting process.

### **2.3.4 Grid & Timestep Independence Testing**

Further grid and timestep independence testing is conducted to establish the minimum grid resolution and time step size for this spherical geometry. The same procedure used for the quasi-two-dimensional model referenced in section 2.2.4 is used here.

For the purpose of determining grid and timestep independence, the melting time for different grid resolutions and different timestep sizes is considered as the point of comparison.

The cases considered are allowed to run up to 20 iterations at each time step, or until the value of the residuals reach the specified convergence criteria of  $10^{-3}$ .

An initial timestep size of 0.5 second was used in the grid independence tests, though this timestep size is varied in the timestep independence testing.

The cases were run until the PCM was considered to be fully melted. The value of the volume-averaged liquid fraction is monitored at 60 second intervals throughout the simulation. When the fully melted condition is achieved (100% volume average liquid fraction), the melting time is reported as the midpoint of the interval in which the fully melted condition appeared. Consequently, the reported melting time is +/- 30 seconds of the actual melting time simulated.

The cases were initialized at a uniform temperature of 293°K throughout the entire domain. At this condition, the entire PCM is in the solid phase (0% liquid fraction), 6°K below the transition temperature.

Sensible heating occurs in the initial stages of the simulation, until the PCM reaches the melting temperature, at which point melting begins. This sensible heating period is included as part of the overall ‘melting time’ reported in both the physical experiment and the simulation.

The constant temperature thermal boundary condition used for the outer wall exterior surfaces is 306K, as was the case in the previous two-dimensional cylindrical case.

A graphical comparison of melting time for different grid resolutions and time step sizes in the spherical case is presented in figure 2.9.

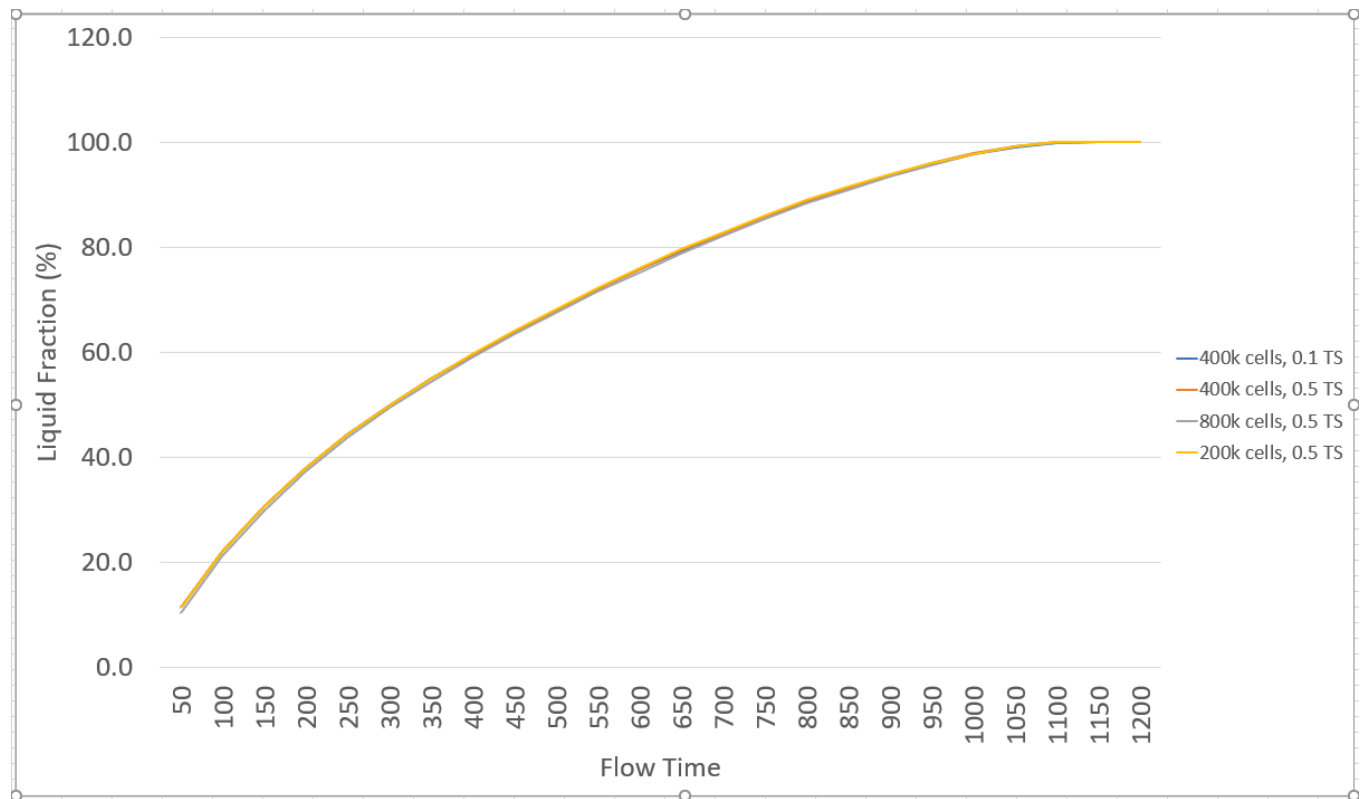


Figure 2.9 - PCM melting time comparison for different grid resolutions & Time steps

The minimum allowable grid resolution is determined to be approximately 200,000 cells, simulated using a timestep size of 0.5 seconds.

### 2.3.5 Melting Results for the Spherical Case

Though the three-dimensional spherical case has no physical experimental counterpart which can be used for quantitatively validating the results, it is thought to be still valid because it was constructed using a validated model for a very similar geometry.

Furthermore, the materials, meshing strategy, numerical procedures, and boundary conditions (where applicable) are all identical to those used in the validated cylindrical model. Hence, the results obtained for the spherical case are likely quite an accurate representation for how this PCM would behave during a melting process for a sphere of the considered dimension and material composition.

The spherically encapsulated PCM was found to become fully melted (100% volume-average liquid fraction) in approximately 1125 seconds. As before this includes the sensible heating period during which the PCM is brought up to the phase transition temperature.

The liquid fraction with respect to time is shown in figure 2.10

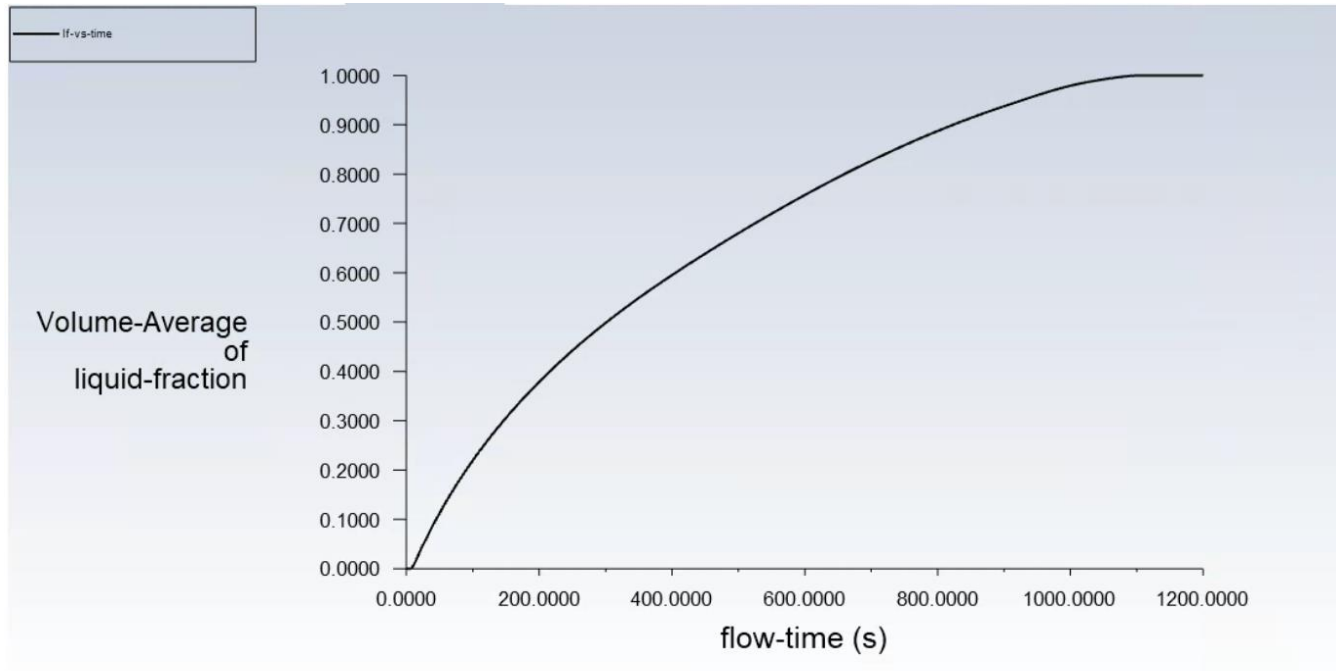


Figure 2.10 – Graph of liquid fraction vs time for the spherical case considered.

What can be observed in figure 2.10 is that the melting process is nonlinear with respect to time. In the early stages of the melt, the liquid fraction increases rapidly, but the rate of melting decreases over time. This is for several reasons. Firstly, when the melting commences, the surface area of the solid phase is the largest, allowing for more heat transfer into the solid given the large surface area. As the size of the solid begins to shrink, the surface area decreases, and the heat transfer rate into the solid decreases as well. Secondly, as the liquid phase begins to form near the outer walls of the PCM cavity, some sensible heating occurs in the liquid PCM near these surfaces. Additional thermal resistance is created, reducing the overall heat transfer coefficient. This effect is further discussed in the following section.

The melting behavior in terms of the position of the solid-liquid interface for the three-dimensional spherical case at different points throughout the melting is shown in figure 2.11.

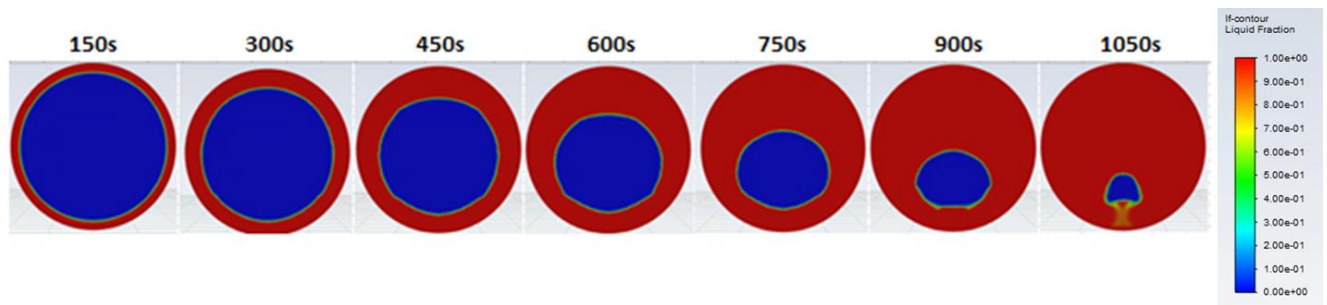


Figure 2.11 - Contours of liquid fraction taken at a vertical midplane at different time intervals for the three-dimensional sphere during the melting process.

These results show good agreement with other three-dimensional spherical melting studies presented in the literature [21-26]. Notably the shape of the solid is ‘correct’, and the average position of the remaining solid in late stages of the melt is slightly below center.

While the melting times are difficult to compare to those in the literature because they vary dramatically with material selection, heat flux conditions, and sphere diameter, the actual melting behavior is still a reasonable point of comparison

Thought it is merely a qualitative comparison, good agreeance in terms of the position of the solid-liquid interface over time with other PCM melting simulations presented in the literature is still a good indication of the model’s validity.

Successfully modelling the correct melting behavior in terms of the position of the solid-liquid interface in PCM encapsulated spheres is largely attributed to accurately capturing the buoyancy induced convection that results from the temperature and density gradients that occur during the melting process.

### 2.3.6 Discussion of Spherical Melting Behavior & Implications Thereof

The melting behavior which is observed for the spherical case in terms of the shape of the solid-liquid interface, flow field within the melt, and temperature field are further discussed in this section.

All of the following contour and vector plots (figures 2.12-2.16) are taken at the same instance in time during the melting process. This moment in time corresponds to a PCM who's volume average liquid fraction is 68%. The contours of the liquid fraction at this stage of the melting are shown in figure 2.12.

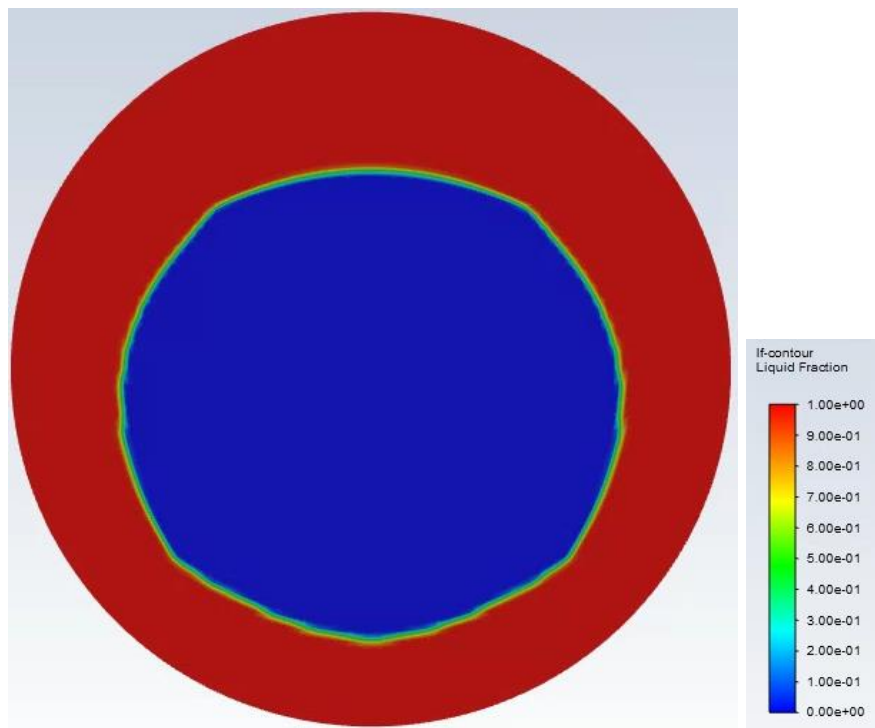


Figure 2.12 – Contours of liquid fraction for the spherical case at 68% volume average liquid fraction, taken at a vertical midplane.

This point in the melting process is chosen arbitrarily, for the purpose of discussing the general melting behavior of the PCM encapsulated sphere.

First, the fluid flow behavior within the liquid PCM should be discussed, in order to demonstrate the buoyancy induced convection that is occurring within the melting PCM.

A contour plot of velocity magnitude within the melting PCM sphere is presented in figure 2.13.

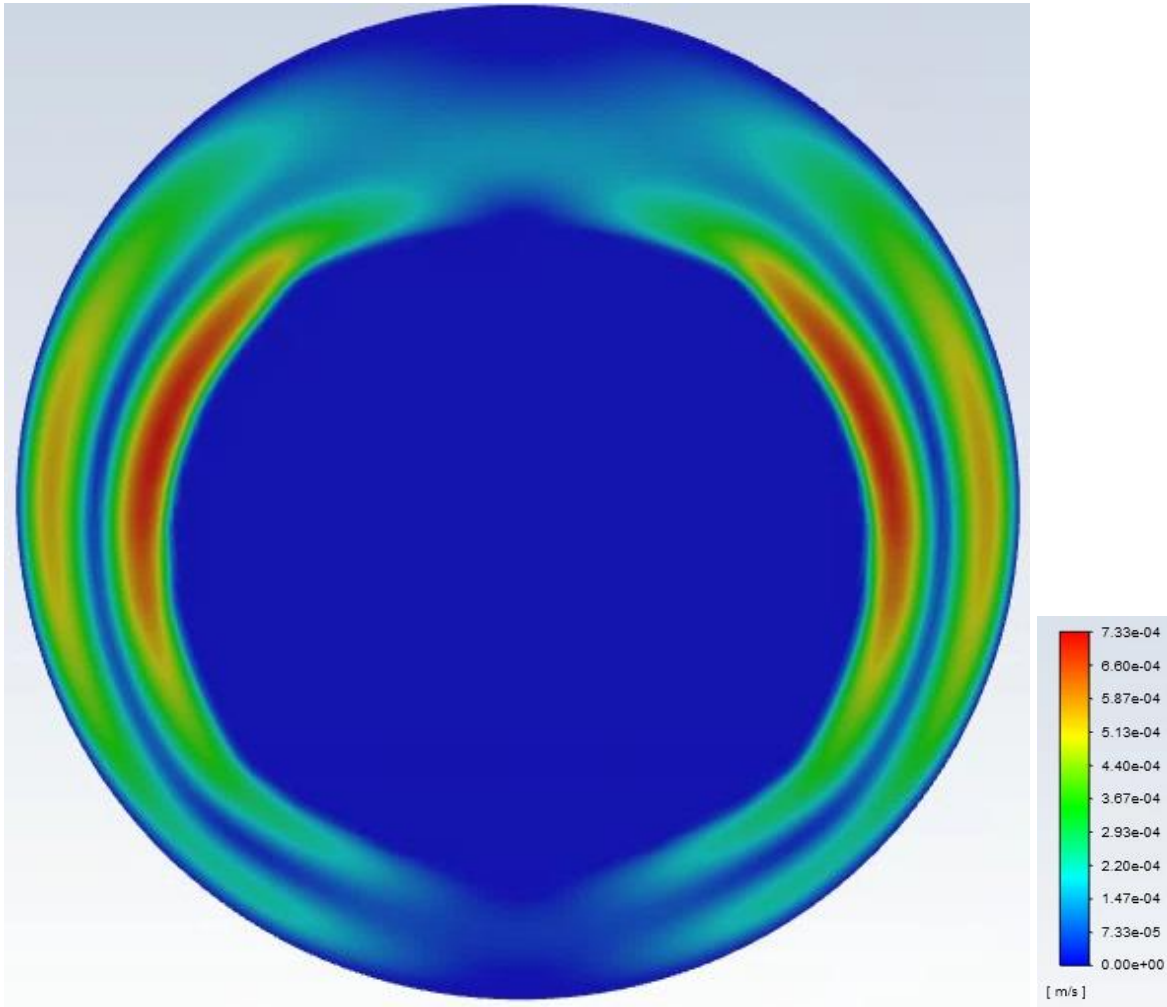


Figure 2.13 – Velocity contours corresponding to a 68% volume average liquid fraction melting PCM sphere, taken at a vertical midplane.

This contour plot well-illustrates the relative velocity magnitude developed within the convective currents. What is immediately apparent is that the largest velocity magnitudes occur at the sides of the solid PCM. As is shown in the following vector plots, the outermost currents have an upward trajectory, whereas the inner currents have downward trajectory, because of the relative

temperatures in these flows and resulting buoyancy. Relatively low velocity magnitudes are experienced at the bottom of the sphere, and in the topmost regions where the steady thermal stratification layers are formed.

The velocity vectors corresponding to the melting state shown in figure 2.13 (68% volume average liquid fraction) are shown in figure 2.14.

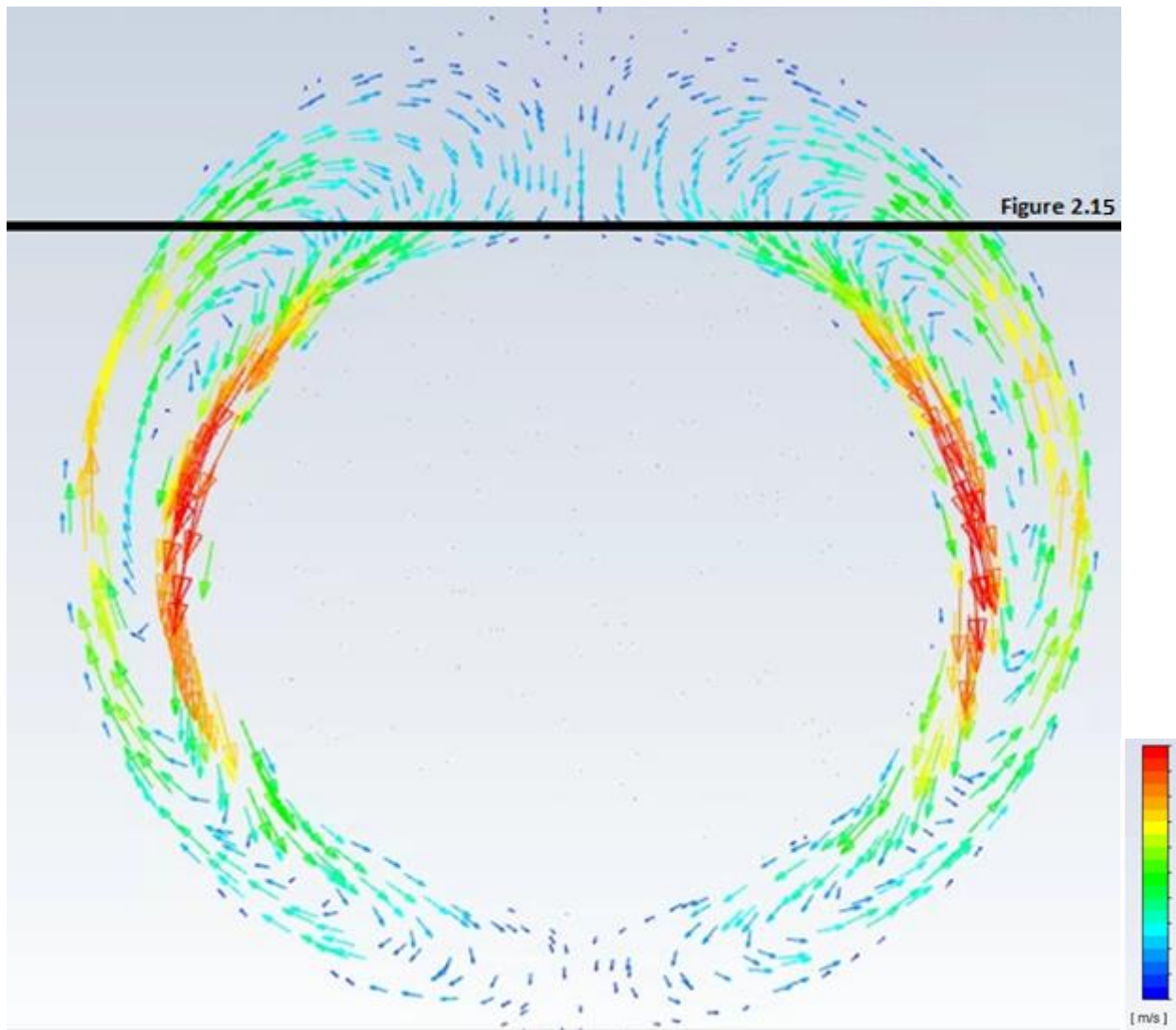


Figure 2.14 – Velocity vector field corresponding to a 68% volume average liquid fraction melting PCM Sphere, taken at a vertical midplane.

As can be seen in figure 2.14, the characteristic flow regime within melting PCM spheres can be observed: The hottest fluid regions (those which are in contact with the exterior surface of the sphere) experience density decrease during heating, promoting an upward flow trajectory along



the outside of the sphere. These flows occur simultaneously on all sides of the sphere, and are bounded by their symmetrical counterparts. As the flow comes into contact with the colder solid PCM, the flow is cooled, resulting in a density increase, and downward currents are formed along the PCM solid surface. The result is a recirculation effect that is symmetrically opposite across the center vertical axis. These recirculation currents that result from the buoyancy induced convection greatly influence the total heat transfer into the solid PCM, and are thus essential to accurately modelling the melting process. The aforementioned material thermal expansion coefficient and mushy zone constant are key parameters in terms of accurately modelling this behavior.

A notable consequence of this flow regime is that the heat contained within the melting PCM is concentrated towards the upper half of the sphere, resulting in asymmetrical melting along the horizontal axis. As such the average position of remaining solid PCM is always below the center of the sphere.

An interesting three-dimensional point of view of the velocity vector field is shown in figure 2.15, which demonstrates the three-dimensional and symmetrical nature of the flow pattern developed within the melting.

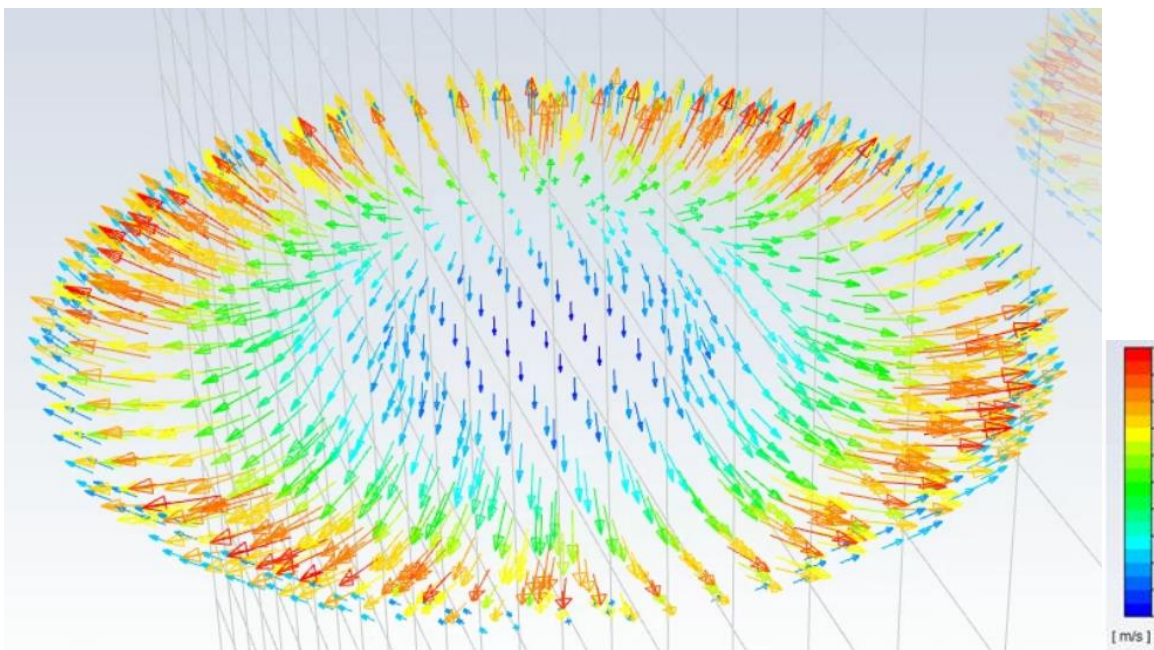


Figure 2.15 – Three-dimensional view of the velocity vector field corresponding to a 68% volume average liquid fraction melting PCM sphere, taken at a horizontal plane at the top of the solid-liquid PCM interface (plane shown in figure 2.14).



Contours of the temperature field corresponding to the same point in the melting process are shown in figure 2.16.

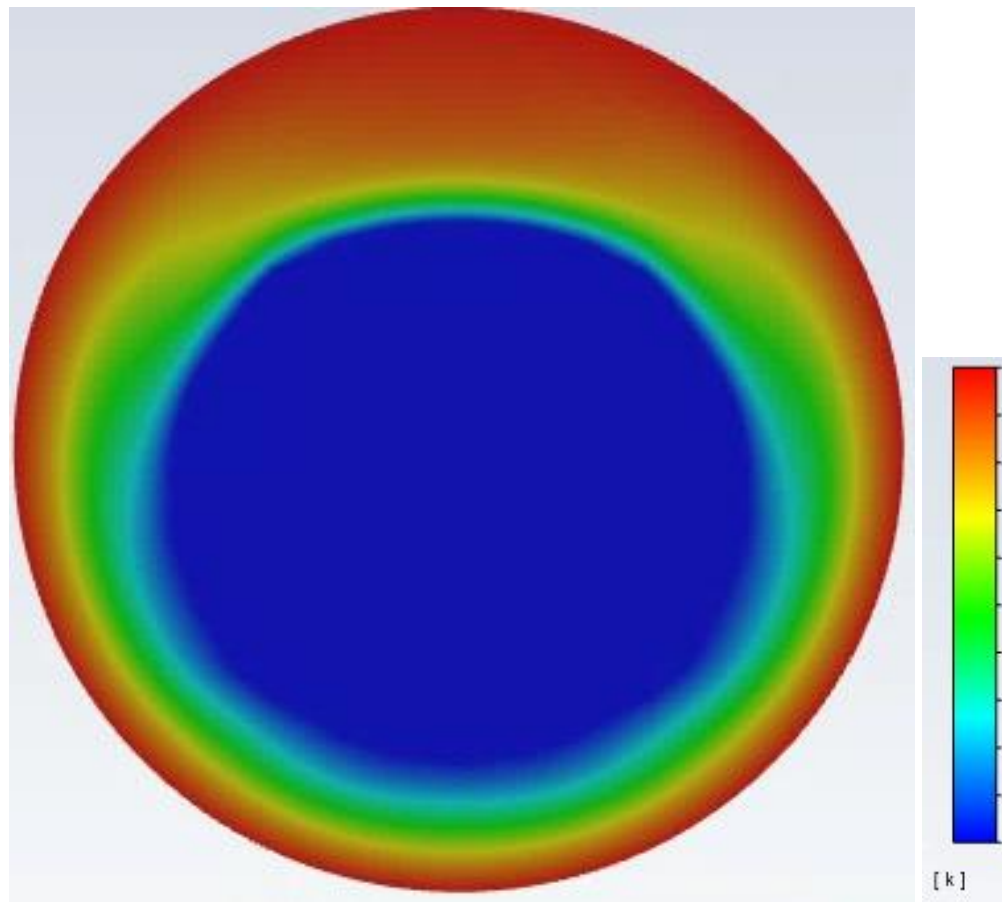


Figure 2.16 – Temperature contours corresponding to a 68% volume average liquid fraction melting PCM sphere, taken at a vertical midplane.

Several things can be observed in these temperature contour plots. Firstly, the solid PCM remains at the phase transition temperature (dark blue), as would be expected. A temperature gradient is developed surrounding the solid PCM, indicating that sensible heating of the surrounding fluid regions is still occurring at the same time as latent heating is occurring in the solid region.

The formation of a steady thermal stratification layer in the in the temperature contours can also be observed. Again, this is a consequence of the flow regime. The warm currents rising along the walls of the spherical container carry heat towards the upper regions of the melting sphere. This effect is why the heat contained within the melting PCM is concentrated towards the upper half of the sphere, and why horizontally asymmetrical melting is observed.

In figure 2.17, the variation of the area average overall heat transfer coefficient  $\bar{U}$  is plotted against the volume average liquid fraction of the PCM sphere.

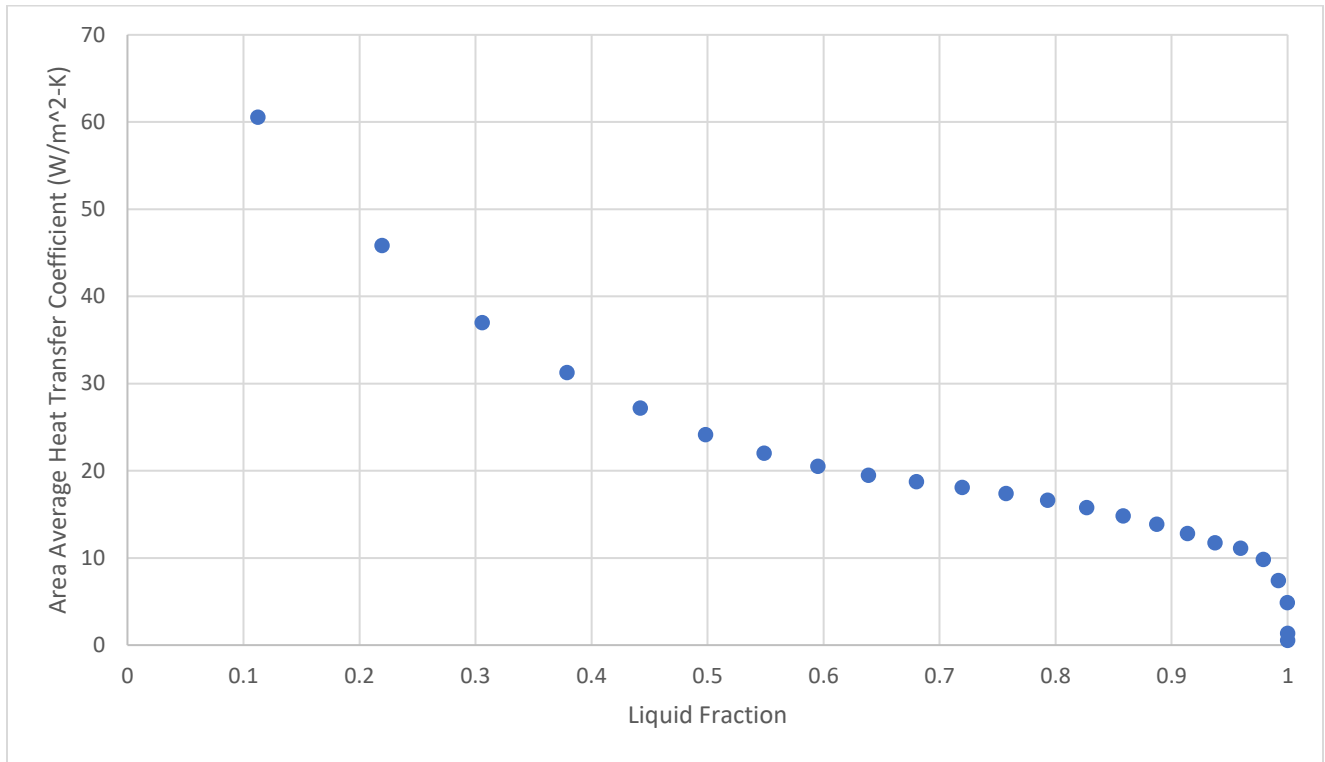


Figure 2.17 – Area average heat transfer coefficient plotted against the liquid fraction (melt fraction) of the spherically encapsulated PCM.

The temperature field that is developed within the melting PCM sphere (as seen in figure 2.16) as the melting progresses is responsible for the variation. The increased thermal resistance associated to the sensible heating of liquid PCM in the outer regions of the spherical cavity results in a decrease in the overall heat transfer coefficient. This reduction in overall heat transfer coefficient is largely responsible for the decrease in the melting rate over time as was seen in figure 2.10.

The implication of this behavior is that the charging rate of the spherically encapsulated PCM is fastest during the early stages of the melting. The charging rate is severely diminished by the time the PCM is almost melted. A reasonable design conclusion would be to suggest that thermal energy storage systems which employ spherically encapsulated phase change material and require rapid charging rates might only be scaled to achieve up to 50% melting during their anticipated charging period, in order to take advantage of the significantly faster charging rate associated to a low liquid fraction.

## Chapter 3

### 3. Approach for Modelling Packed Beds of Spherically Encapsulated PCM

The following chapter is dedicated to an explanation of the model implementation in the context of packed beds. The same numerical formulation in terms of the governing equations, phase change modelling, and treatment of volumetric expansion as explained in Chapter 2 for the model development is used for modelling of the packed bed. The purpose of this work is to demonstrate that the fundamental, high-fidelity approach used for modelling an individual sphere can be extended to a packed bed containing many spheres without the need for a separate numerical formulation. This high-fidelity approach involves modelling the packed bed as true lattice of spherical elements in a given packing arrangement, surrounded by a flow field. This is a relatively unique approach as opposed to the modelling of the packed bed as a continuous porous medium, as is done in much of the preceding literature discussed in the literature review [38-51].

The general model implementation is discussed, followed by an introduction of the novel computationally efficient method, and finally a parametric study to demonstrate the full model. Regarding the general model implementation: the packed bed geometry and materials considered are introduced. The mesh generation strategy used to spatially discretize the packed bed and the internal PCM spheres is then explained. The boundary conditions and numerical procedures used to solve the governing equations are provided. Regarding the computationally efficient method: a general description of the method is provided, followed by some corrections which can be used to improve the accuracy of the method in certain situations. Regarding the parametric study: the impact of parameters such as sphere diameter and HTF inlet temperature on the performance of the packed bed in terms of the charge and discharge rates are studied. The primary purpose however is a demonstration of the presented method.

## **3.1 Model Implementation in a Packed Bed**

### **3.1.1 Geometry & Materials Description**

The packed bed geometry considered is an organized packed bed arranged in a parallel packing structure. The packing is comprised of a 3 x 3 x 3 lattice of PCM encapsulated spheres, which are all of uniform diameter. 27 total spheres make up the packing arrangement. The packed bed geometry also includes the length of one sphere diameter as an inlet and outlet region, to better allow for the visualization of the surrounding heat transfer fluid flow field before and after coming into contact with the packing arrangement. The spheres themselves are of the same geometry introduced in Chapter 2 for the single spherical case. The spheres have a 20mm inner diameter acting as the internal PCM cavity, and a 1mm wall thickness, resulting in an outer diameter of 22mm. The spheres are arranged such that they are tangential with each other in both the horizontal and vertical axes, in the parallel packing arrangement. The extents of the packed bed are therefore 66mm x 66mm in width and length, and 110mm in height due to the inclusion of the inlet and outlet regions. The materials used in the packed bed for the composition of the spheres are the same as those used in Chapter 2 for both the cylindrical and spherical cases.

The phase change material used is the Rubitherm RT26 PCM, with material properties as indicated in Table 2.2 in Chapter 2, and in Appendix A6. The thermal & physical properties of the PCM are again treated as constant and independent of temperature and state, with the exception of the density of the liquid which is treated using the Boussinesq approximation. The material used for encapsulating shell is the same acrylic material, with material properties as indicated in Table 2.3 in Chapter 2. As before the properties of the acrylic are treated as constant and independent of temperature.

The substance used for the surrounding heat transfer fluid is liquid water, with constant thermophysical properties taken at the inlet temperature of the heat transfer fluid. While water would not typically be a suitable heat transfer fluid for practical applications, it is a sufficient candidate in this theoretical case to demonstrate the functionality of the method within the packed bed.

A 2D schematic representation of the packed bed geometry considered is provided in the following figure: (All dimensions in mm)

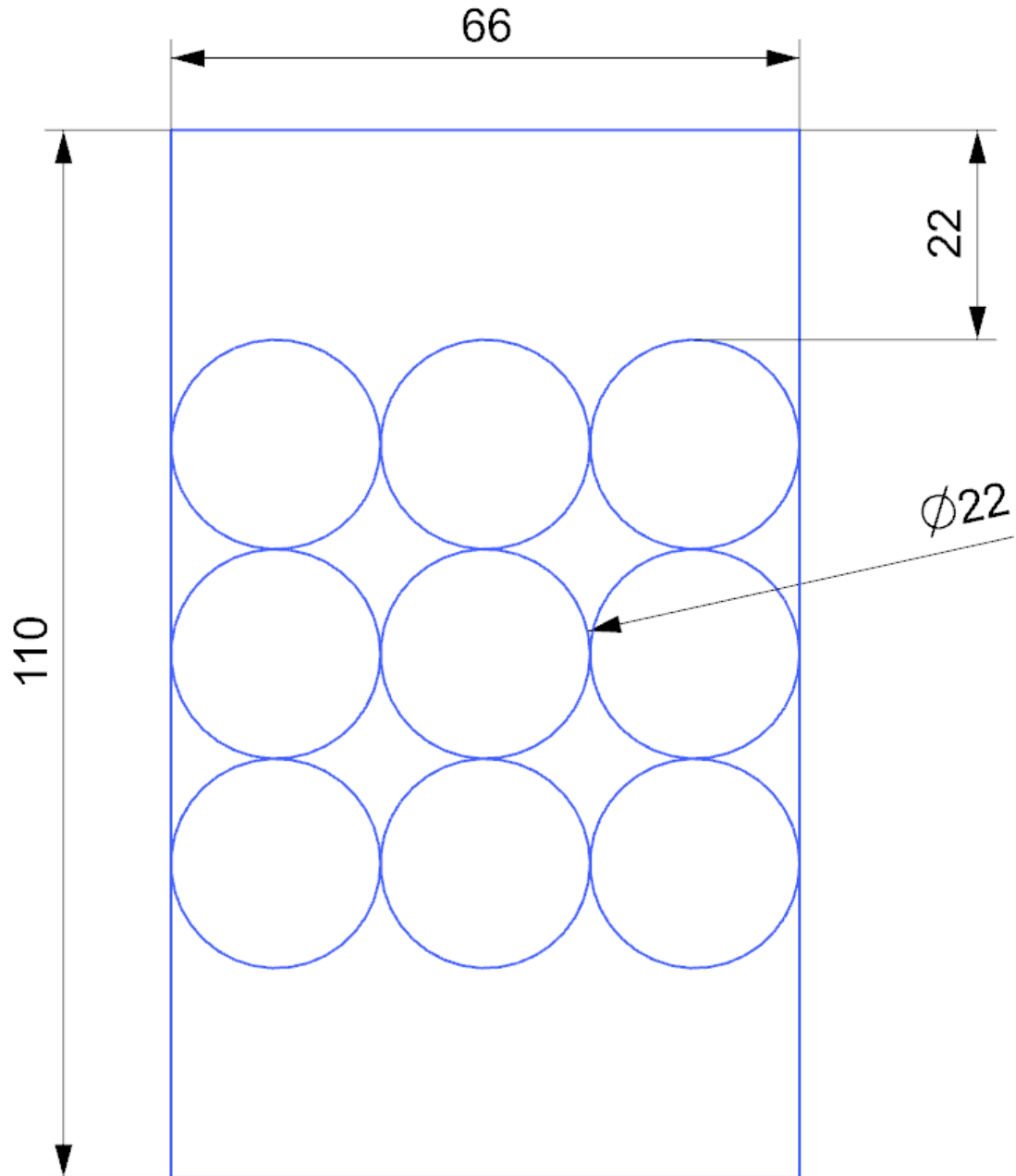


Figure 3.1- 2D Schematic of the 3D packed bed geometry considered (dimensions in mm).

### 3.1.2 Mesh Generation Approach

In this section, the mesh generation strategy for implementing the model in a packed bed arrangement is discussed. The computational meshes for the packed bed were generated using Pointwise V18.3R1 64-bit meshing software [58]. An isometric and 2D view of the full mesh for the PCM encapsulated sphere packed bed is provided in the following figure:

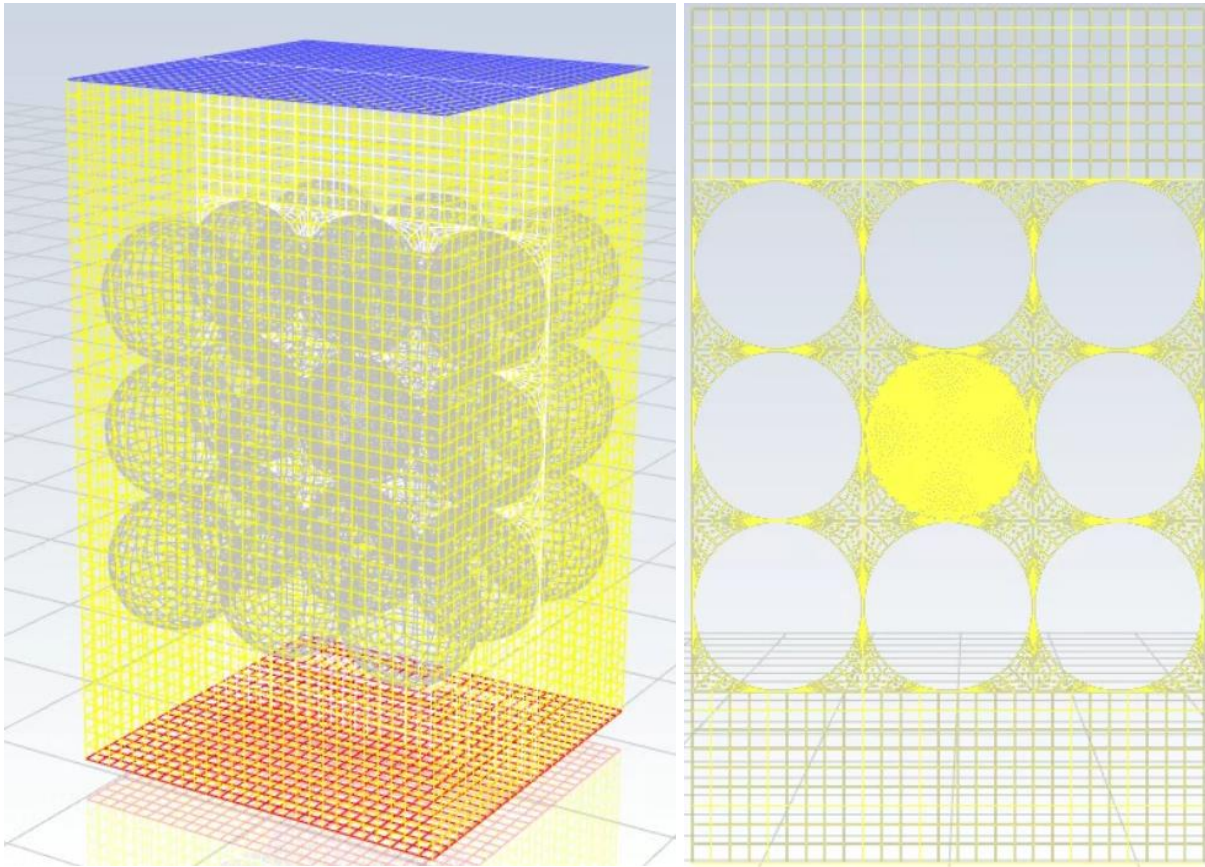


Figure 3.2 - Isometric and 2D view of the  $3 \times 3 \times 3$  sphere packed bed mesh. The blue boundary is the inlet, and the red boundary is the outlet.

The mesh generation strategy for the PCM encapsulated spheres which are to undergo melting & solidification is the same as that presented in Chapter 2 for the single spherical case. This involves the generation of a high resolution, structured hexahedral o-grid style mesh, with uniform grid spacing throughout. This mesh structure was found to be important in order to generate accurate results for the melting process. The actual mesh used for the PCM encapsulated sphere in the packed bed is identical to that in Chapter 2 for the single spherical case, as this mesh has already



been tested for spatial independence during the melting process. The lowest resolution mesh that produced grid independent results for the single spherical case is used, to minimize computational cost in the packed bed case while still producing accurate results in terms of melting behavior.

The mesh generation strategy for the surrounding packed bed involved generating a structured hexahedral mesh surrounding all of the encapsulated PCM spheres, and in the inlet and outlet regions. The structured hexahedral mesh in the HTF region of the packed bed was found to generally improve solver convergence, and reduce the number of grid elements required to achieve a grid independent solution.

The pressure drop in the HTF across the packed bed was used as a point of comparison to validate that the resolution of the surrounding packed bed mesh was spatially and temporally independent.

Clustering of grid elements in the surrounding flow field is performed in the areas surrounding the PCM encapsulated spheres, as shown in figure 3.3.

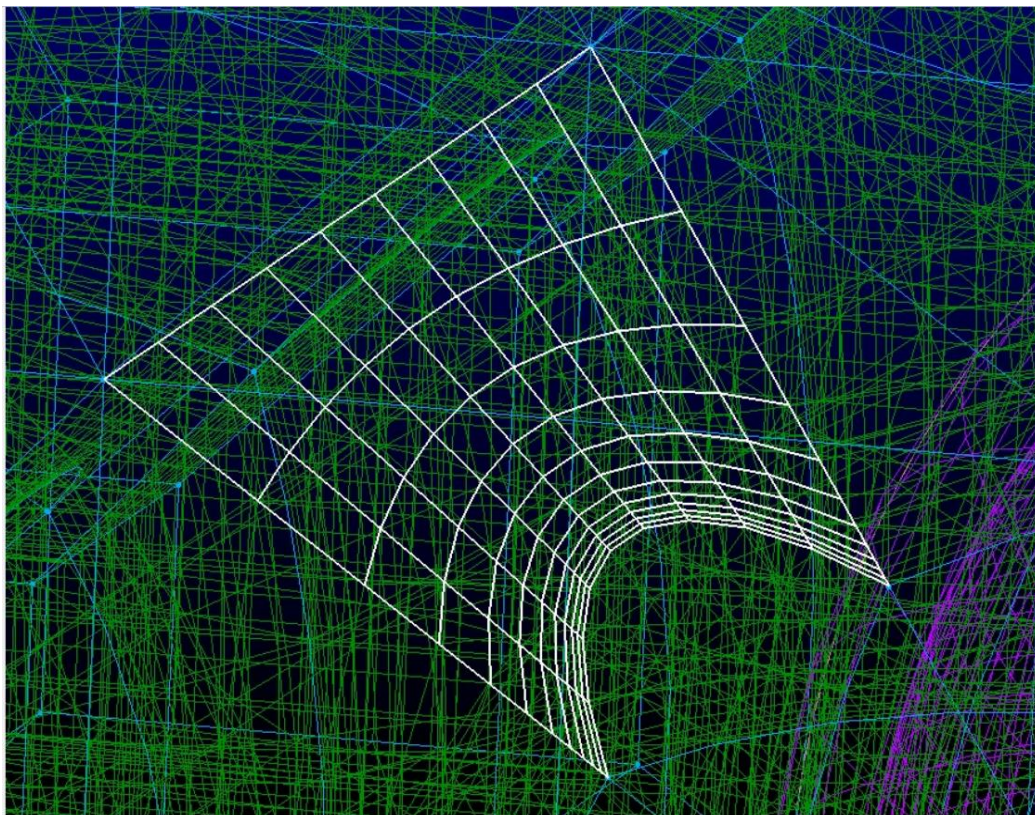


Figure 3.3 - Clustering of grid Elements towards the sphere wall boundaries in the outer flow field for the packed bed mesh.

This clustering of grid elements is performed in order to accurately resolve the boundary layer behavior of the surrounding heat transfer fluid in close proximity to the spheres. This is especially important for the central sphere, as the heat flux conditions measured on this surface are an important output parameter for the translational heat flux method to be discussed.

It was found that over-refining the mesh in the flow field surrounding the PCM encapsulated spheres led to solver instability. This issue was most prevalent in the pinch points between the PCM encapsulated spheres. Though the solid model was constructed such that adjacent spheres were tangential at their centerlines, the computational interpretation of this tangentiality in terms of spatial discretization still resulted in extremely small mesh elements existing in these pinch points. Over refining the surrounding mesh compounded this issue, and resulted in immediate solver divergence as the flow field was unable to be resolved in these regions. A careful balance had to be struck between refining the HTF flow field mesh enough to achieve grid independence, but not so much that the mesh elements between the PCM encapsulated spheres were small enough to cause divergence.

### 3.1.3 Boundary Conditions

The boundary conditions are summarized in Table 3.1. The locations of these boundary conditions are shown on a schematic of the geometry in figure 3.4.

Table 3.1 - Summary of boundary conditions imposed on the three-dimensional packed bed for melting and solidification simulations.

<b>Location/Type</b>	<b>Boundary Condition</b>
Top Face (Inlet)	-Constant temperature thermal condition -Constant velocity momentum condition
Bottom Face (Outlet)	-Coupled thermal condition -100% outflow condition momentum condition
All Side Faces (4)	-Symmetry condition
PCM Sphere Outer Wall (central sphere only)	-Coupled thermal condition -No slip momentum condition



PCM Sphere Inner Wall (central sphere only)	-Coupled thermal condition -No slip momentum condition
Void Spheres Outer Wall (all remaining 26 spheres)	-Heat flux thermal condition -No slip momentum condition

The top face of the packed bed domain is given an inlet boundary condition, to enable this surface to act as the inlet orifice for the incoming heat transfer fluid. At this boundary, a constant temperature thermal condition is imposed, to simulate the condition that the HTF entering the packed bed is at a known and constant temperature. A constant and uniform velocity momentum condition is imposed to simulate a fully developed plug flow at the inlet, to allow for the flow through the packed bed to be fully developed.

The opposite face of the packed bed domain (bottom face) is the outlet boundary. Here a coupled thermal condition is applied, to allow for the temperature of the HTF at the outlet to become a natural consequence of heat transfer throughout the domain. A 100% outflow momentum condition is applied, as this is the only outlet orifice in the domain. Under this condition, the entirety of the mass flow rate of HTF is allowed to escape through this boundary.

The four side faces of the domain are given symmetry boundary conditions. This is to simulate the condition that this domain is a small section of a larger packed bed in both length and width.

At the central discretized sphere outer wall, coupled thermal conditions are applied to enable the temperature at this surface to develop naturally as a result of heat transfer through the packed bed. This wall boundary is given no slip momentum conditions, as this surface is in contact with the surrounding heat transfer fluid.

For the inner walls of the central discretized sphere, coupled thermal conditions are again applied to enable the temperature at this surface to develop naturally as a result of heat transfer through the acrylic shell and into the PCM. This wall boundary is also given no slip momentum conditions, as this surface is in contact with the liquid PCM once it begins to melt.

At the wall boundaries for the remaining 26 surrounding spheres (modelled as void interiors with wall boundary conditions), heat flux thermal conditions are applied to simulate the condition that all spheres contribute to heat transfer to and from the HTF. The method used to obtain the value

of these heat flux conditions is explained in the following sections regarding the computationally efficient method. No slip momentum conditions are applied to these boundaries, as they are in contact with the surrounding heat transfer fluid.

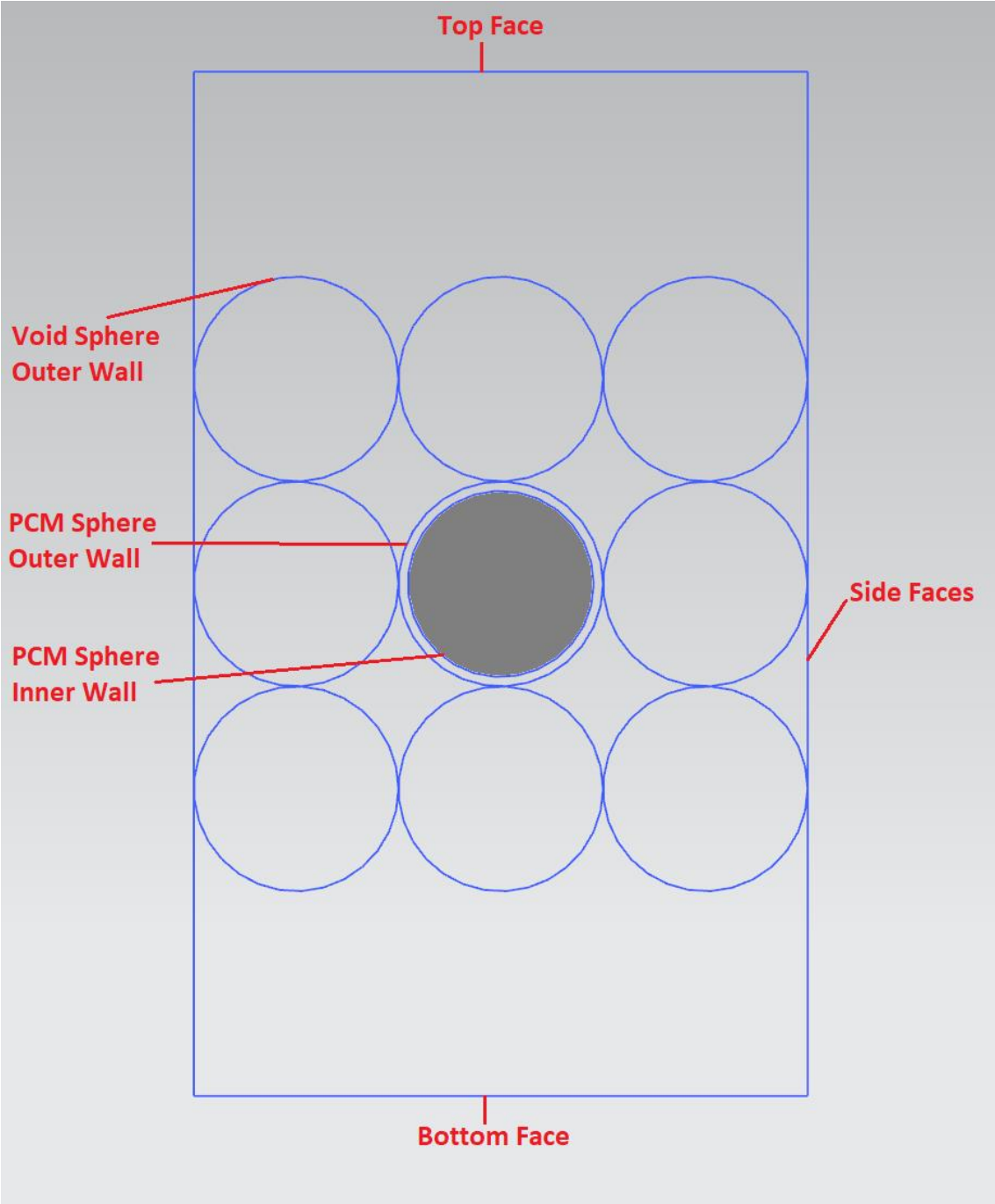


Figure 3.4 - Schematic of the Boundary Condition Locations Used for the Packed Bed.

### 3.1.4 Numerical Procedure

ANSYS Fluent [53] is again used to solve the system of transport equations. The numerical procedure for the packed bed is the same as that for the cases described in Chapter 2 for the quasi-two-dimensional cylinder, and for the three-dimensional single sphere.

The pressure-based solver is used, as this solver must be used when enabling the solidification and melting model within Fluent. Transient simulations are conducted to study melting and solidification over a period of time. Gravity is enabled to permit buoyancy to drive fluid motion within the liquid phase of the melting PCM sphere. Higher order schemes are used wherever possible, with the exception being the first-order upwinding scheme used for the momentum. A summary of the numerical methods used are given in Table 3.2.

Table 3.2 - Summary of Numerical Methods Used for The Packed Bed Cases

Method	Value or Condition	Explanation
Pressure-Velocity Coupling Scheme	SIMPLE	...
Gradient	Least Squares Cell Based	Most accurate method, requires less computational effort than node based.
Pressure	Second Order	Higher order scheme
Momentum	First Order Upwind	Instability issues with higher order
Energy	Second Order Upwind	Higher order scheme
Transient Formulation	Second Order Implicit	Higher order scheme

### 3.1.5 Flow Through the Packed Bed

The purpose of this section is to describe the flow of the HTF through the packed bed. The velocity vectors of the heat exchange fluid through the packed bed, taken at a diagonal plane slicing through the middle of the domain from corner to corner are shown in figure 3.5.

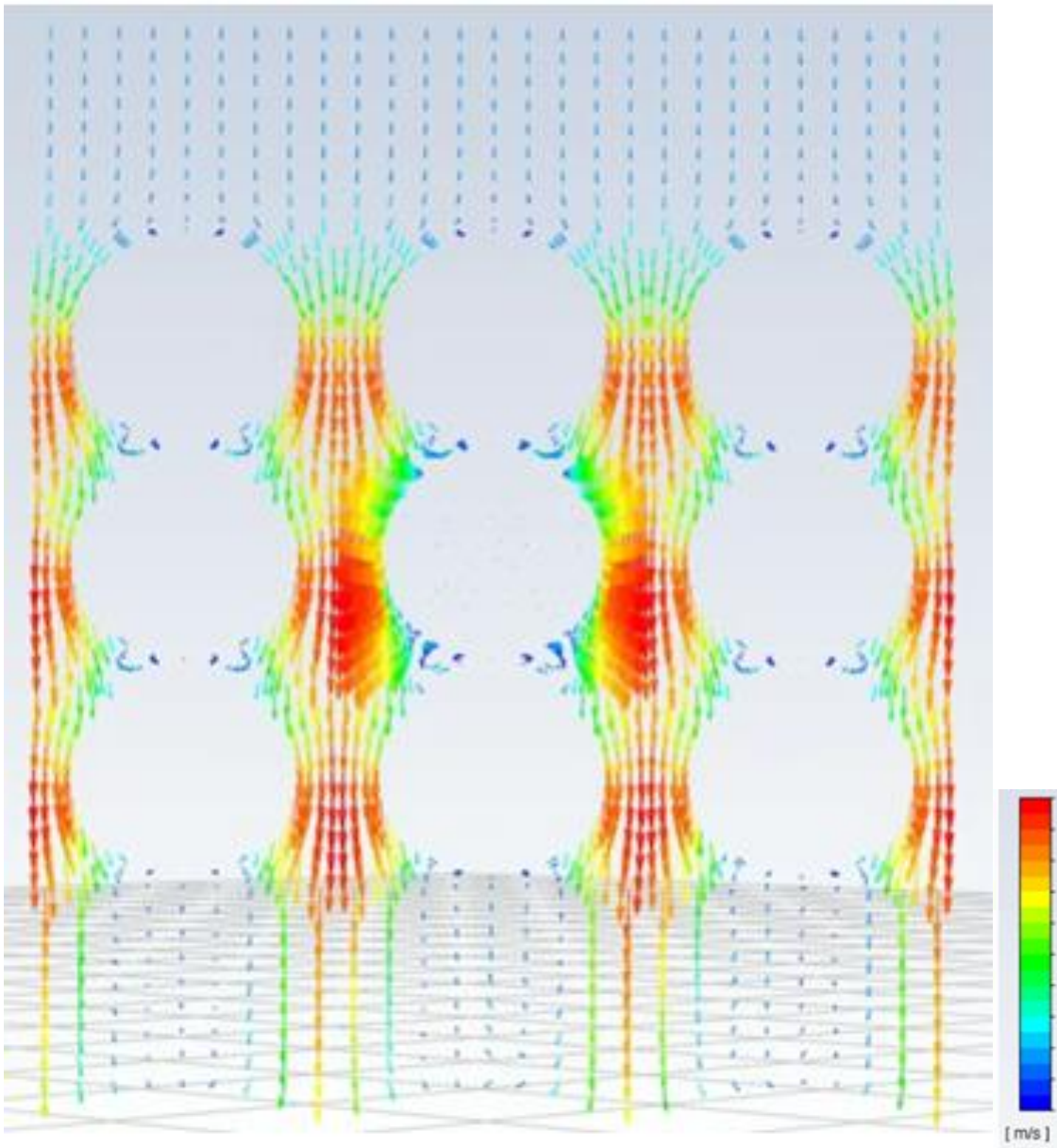


Figure 3.5 - Velocity vector field in the packed bed of PCM encapsulated spheres, taken at a diagonal middle plane at the start of the melting process. The packed bed flow field is constant throughout the melting process.

The inlet velocity boundary condition is set based on the diameter of the spherical elements, such that the flow is well within the laminar region. The velocity magnitude across the whole inlet surface is constant and uniform, as described in the boundary conditions. The actual velocity magnitude imposed to satisfy this condition is 0.01 m/s, corresponding to a Reynolds number of around 160-200 (this varies with respect to the density and viscosity of the HTF, given they are a function of temperature).

As shown in figure 3.5, the flow begins as a uniform plug flow in the inlet region, before coming into contact with the packed bed elements. The flow then channels into the empty regions between the spheres, where an increase in HTF velocity is observed as it is forced through the narrower channels. The red vectors in figure 3.5 indicate the highest velocity magnitude. This increase in fluid velocity between the packing material in packed beds has been shown to increase the heat transfer coefficient on the HTF side, and increase the heat transfer into the PCM spheres [38-40,40-42,50-51]. The flow then returns to a near uniform distribution in the outlet region, after having passed through the packed bed. The increased mesh resolution in the areas surrounding the central melting sphere is visible on the vector map by proxy of the increased vector density. This refinement is important, as it allows for an improved estimation of the heat transfer coefficient on the fluid side, resulting in an improved measurement of the heat flux at this boundary.

Accurately capturing the behavior of the flow field in the area surrounding the wall boundary of the central sphere is important in order to improve the accuracy with which the melting behavior is modelled. It is especially important in this model, because the measured value of the heat flux on this boundary is to be imposed on all surrounding sphere wall boundaries, as is to be discussed in the following section.

## **3.2 Computationally Efficient Method Introduction**

A novel method for efficiently modelling the melting and solidification process in a bed of spheres encapsulating PCM is presented, along with a proposed correction.

### **3.2.1 General Description of the Method**

The method in short, involves translating information from a fully discretized sphere which is undergoing the computationally expensive phase change process, to other spheres within the packed bed which do not need to be fully discretized or undergo phase change.

The main advantage of the presented method is that it eliminates the need to simulate the full melting and solidification processes in all PCM encapsulated spheres in the bed. The method is an approach which is able of capturing the thermal exchanges between the working bed fluid and all spheres in the bed, while simulating the full phase change process in only one sphere located centrally within the packed bed arrangement.

The target central sphere is fully discretized and modelled internally, using the mesh structure and mesh resolution presented in Chapter 2 for the single spherical case. The surrounding spheres in the packed bed are left as voids within the domain, with no interior meshing. These void regions are imposed by wall boundary conditions that represent the exterior boundaries of the spheres within the packing arrangement.

The method involves measuring the area-average heat flux on the exterior wall of the target centrally located sphere within the packed bed, as the melting or solidification process occurs. The value of this area-averaged heat flux is stored as an output parameter at each time interval throughout the melting and solidification processes.

The value of the heat flux on this wall boundary is highly transient, and changes significantly throughout the melting process as the liquid fraction of the PCM sphere increases. It is not sufficient to merely assume a constant heat flux occurs at this boundary, as doing so would

effectively ignore the impact of the melting and solidification process on the heat transfer into and out of the PCM spheres.

The heat flux output parameter is then imposed as a heat flux wall boundary condition on all surrounding spheres (represented by voids with wall boundaries in the domain). This boundary condition is then updated at each time interval, as the value of the measured area average heat flux output parameter is updated throughout the melting process. What is effectively being done is the value of the heat flux on the exterior surface of the discretized sphere is being measured, and then translated to all other spheres in the bed. The term translational heat flux method therefore seems an appropriate description.

The result is a model capable of approximating the performance of an entire packed bed arrangement (in terms of heat exchange between the spheres and the surrounding heat transfer fluid in the packed bed), while only modelling the computationally expensive solidification and melting processes within a single sphere. A schematic representation of the method is presented in figure 3.6:

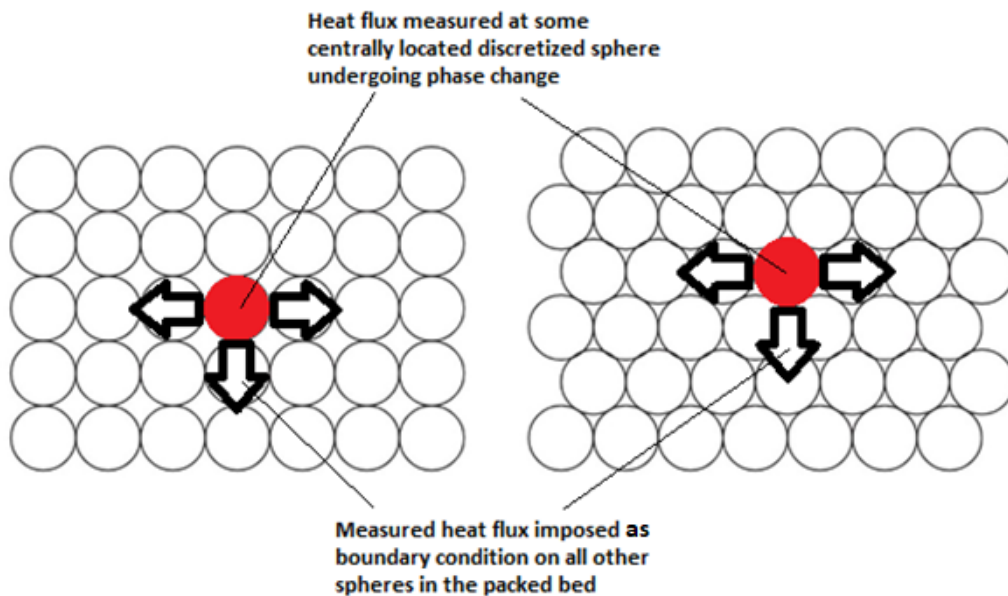


Figure 3.6- Schematic Representation of Translational Heat Flux Method.

The proposed method is equally applicable to virtually any packing arrangement. In random packing arrangements, the selection of the central discretized sphere should be carefully selected,

in order to ensure that a sphere representing the approximate average position of all spheres in the packed bed is used as the measurement region.

### 3.2.2 Heat Flux Correction

In a packed bed, the temperature of the heat transfer fluid changes as it flows through the packing elements and exchanges heat with them. Because of this, the actual heat flux at each sphere's boundary changes along the length of the bed, as the temperature of the HTF decreases. Hence, for long packed beds where the change in fluid temperature between the outlet and the inlet is significant, the change in fluid temperature should not be ignored.

In such cases, a correction is proposed for the heat flux, where the heat flux imposed on the spheres at a given bed depth is calculated based on the depth specific temperature difference between the HTF and the PCM (which can be obtained using a log mean temperature difference correlation for the fluid with respect to number of spheres passed over).

This temperature correction for the HTF at some depth in the bed is derived from the equation describing the temperature of an internal pipe flow with a constant surface temperature, and a known inlet temperature, as a function of distance from the pipe inlet. The derivation is as follows:

In a fully developed, enclosed pipe flow, an energy balance is applied to calculate how the mean temperature of the flowing fluid  $T_m$  varies logarithmically along the axial position of the pipe. The expression describing this variation in temperature is in the axial direction of the pipe is:

$$\frac{T_w - T_m(x)}{T_w - T_{m.inlet}} = \exp\left(-\frac{Px}{\dot{m}c_p}h\right) \quad (3.1)$$

Where  $T_w$  is the constant surface temperature,  $P$  is the perimeter of the pipe,  $x$  is the distance from the inlet,  $h$  is the convective heat transfer coefficient (constant for a fully developed flow),  $\dot{m}$  is the mass flow rate through the pipe, and  $C_p$  is the specific heat capacity of the fluid.



The log mean temperature variation obtained using equation 3.1 for the internal pipe flow with constant wall temperature is illustrated in figure 3.7.

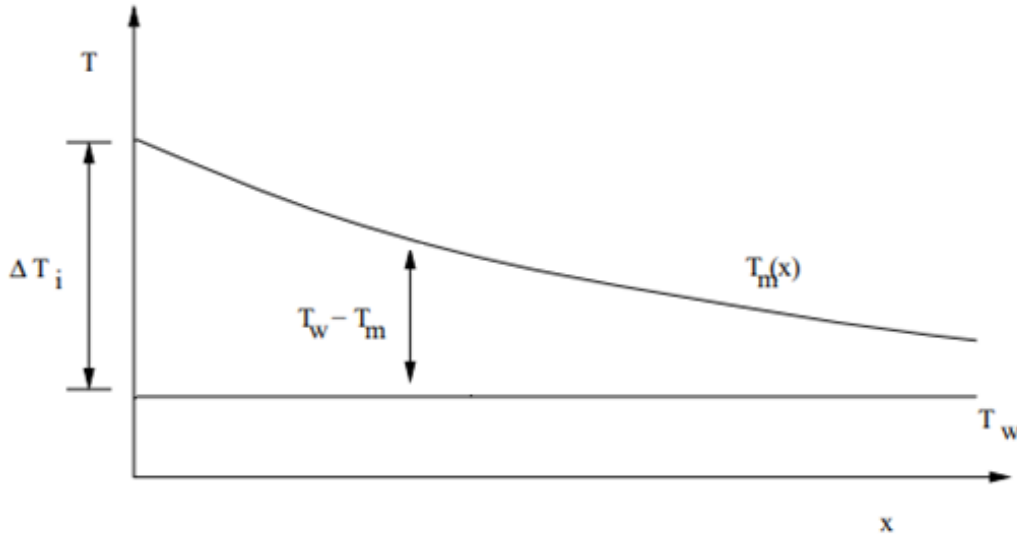


Figure 3.7 – Variation in the mean temperature of a fluid in an internal pipe flow with constant wall temperature

Equation 3.1 is then modified, to generate the corrected temperature difference for some depth in the packed bed:

$$\frac{T_{transition} - T_{HTF,depth}}{T_{transition} - T_{HTF,inlet}} = \exp\left(-\frac{NA_S}{\dot{m}_{HTF}C_p}h\right) \quad (3.2)$$

Where  $T_{HTF}$  is bulk mean temperature of the HTF,  $N$  is the total number spheres passed over by the HTF between the inlet and the specified bed depth,  $A_S$  is the surface area of a single sphere,  $h$  is the convective heat transfer coefficient of the HTF through the bed,  $\dot{m}_{HTF}$  is the mass flow rate of the heat transfer fluid, and  $C_p$  is the specific heat capacity of the HTF.

The terms  $NA_S$  effectively represent the heat transfer surface area the HTF has come into contact with at a given depth in the bed (instead of  $Px$  in the pipe flow equation). The convective heat transfer coefficient  $h$  through the bed can assumed to be constant for a fully developed HTF flow in the packed bed, just as for the pipe. The phase transition temperature of the PCM  $T_{transition}$  is

used in place of the constant wall temperature. This wall temperature is assumed to be approximately constant at the PCM phase transition temperature for the duration of the melting and solidification process, given the isothermal nature of latent heating. The mass flow rate of the heat transfer fluid  $\dot{m}_{HTF}$  is imposed as a boundary condition at the inlet of the packed bed.  $C_p$  is a property of the HTF substance being used.

This correction can be used to obtain a crude approximation for the depth specific temperature difference between the heat transfer fluid and the PCM spheres at that depth.

The heat flux boundary condition which is imposed on the wall boundary of the empty void spheres at a given bed depth can then be calculated using the overall area average heat transfer coefficient on the central sphere (which can be measured at each time interval and stored as an output parameter to be used in the boundary condition definition, just as was done for the heat flux in the uncorrected method) and the depth-corrected temperature difference.

The depth corrected heat flux can be calculated using:

$$\phi_{Depth} = \bar{U}(T_{transition} - T_{HTF,depth}) \quad (3.3)$$

Where  $\phi_{Depth}$  is the heat flux at a certain depth, and  $\bar{U}$  is the overall area average heat transfer coefficient on the central sphere, measured at each time interval and stored as an output parameter to be used in the boundary condition definition for the void spheres.

The result is that spheres positioned nearest the inlet will have a higher heat flux boundary condition imposed upon them, and spheres positioned nearest the outlet will have a lower heat flux boundary condition imposed upon them.

In short packed beds, or packed beds where the heat transfer fluid mass flow rate is high, the fluid temperature change between the inlet and outlet is small, and the imposition of the same heat flux (as of the central sphere) on all spheres in the bed does not cause considerable errors. This is confirmed in the present study, where the imposition of constant and corrected heat fluxes led to almost identical results for the short-packed bed considered. At a given bed height, the heat flux

experienced by the PCM spheres in the peripheral region of the bed i.e. in contact with the physical boundaries of a packed bed would be a different as they interact with the exterior wall. The convection heat transfer at the exterior surfaces of these spheres would also be different as the flow pattern of the heat transfer fluid would be altered due to the presence of the exterior wall. However, such spheres represent a very small fraction of the total spheres in the packed bed, and thus the imposition of an average heat flux on these spheres does not lead to any significant error in terms of the performance of the entire packed bed.

The proposed correction is an imperfect one. It is predicated on the assumption that the depth specific temperature difference between the heat transfer fluid and the PCM spheres considers the PCM spheres to be constantly at their phase transition temperature, which is not the reality. Although the latent heating process is in general isothermal, outer regions of the PCM sphere do experience sensible heating while the phase change is still occurring in the central region, as was discussed in section 2.3.6. The true nature of the temperature difference between the HTF and the PCM spheres is therefore smaller in reality than in the proposed correction. The depth specific HTF bulk mean temperature is for this reason overcorrected in the proposed correction.

The correction also involves the assumption that the overall heat transfer coefficient measured on the central sphere at each time interval is applicable to all spheres within the packed bed at the same time interval. This is only true if the liquid fraction of all spheres within the packed bed is approximately the same. This overall heat transfer coefficient changes throughout the melting process as a function of the liquid fraction, as was discussed in section 2.3.6. Because of this, the correction is largely invalid for very long packed beds where the liquid fraction of PCM spheres near the inlet varies significantly from the liquid fraction of spheres near the outlet. In such cases, the overall heat transfer coefficient between the two extremities of the bed would change significantly, and the correction would be inaccurate.

The ultimate correction would involve updating the heat flux boundary condition at any given depth in the bed as a function of the anticipated liquid fraction of spheres at that depth, in accordance with the relationship between the overall heat transfer coefficient/heat flux and the liquid fraction shown in section 2.3.6. This type of correction has not been successfully implemented at the time of writing.

The limitations and issues associated to using the proposed correction are acknowledged by the author. In spite of these limitations, the general method associated to translating information from a discretized sphere undergoing phase change to other spheres in the packed bed is still valid. While the correction could be improved, the fundamental advantage of the translational heat flux method is unchanged.

### **3.3 Demonstration of the Method Via Parametric Study**

In this section, the fully developed model is used in combination with the translational heat flux method to perform a parametric study. Several parameters of interest such as the PCM encapsulated sphere diameter, and the inlet temperature of the surrounding heat transfer fluid are parametrized, with their impact on the charging and discharging rate of the PCM being the primary point of comparison.

The parametric study is performed for both the melting (charging) and solidification (discharging) modes of the spherically encapsulated PCM packed bed. This is to demonstrate that the model is fully capable of supporting both solidification and melting processes without any required modifications. The numerical procedure, meshes, material properties, and types of boundary conditions used are exactly the same in both the melting and solidification cases.

While this parametric study evaluates certain parameters of interest in terms of designing such devices, its primary purpose is to demonstrate the presented method as being capable of supporting more thorough design activities. Though only one packing arrangement and combination of materials is presented in this parametric study, the method is intended to be generally applicable to virtually any packing arrangement, bed sizing, and material selection.

First a reference case is presented for both solidification and melting, and some remarks are made regarding the capabilities of the method to model packed beds containing PCM encapsulated spheres. These reference cases are followed by the parametric study, wherein the impact of the varied parameters on the charging and discharging rates of the PCM are compared to those in the reference cases

### 3.3.1 Reference Cases

In the following, the reference cases for both solidification and melting are presented.

#### *Melting*

In the melting cases, the 22mm OD PCM spheres are initialized at a temperature below their phase transition temperature, such that they begin as pure solids with zero percent liquid fraction. Given that the phase transition temperature of the Rubitherm RT26 PCM used is 299K, the PCM spheres are initialized at a uniform temperature of 293K to ensure they begin as pure solids. Because of this, some sensible heating occurs before the phase change begins. This sensible heating period is included in the overall melting time reported in the results.

In a melting (charging) process, heat from the surrounding HTF is exchanged with the PCM spheres as the HTF flows through the bed elements, which are charged via thermal energy content of the HTF. To allow for heat transfer into the PCM spheres, the surrounding HTF is allowed to enter the domain at a constant inlet temperature which is above the PCM melting temperature. In the reference case, the inlet temperature of the surrounding HTF is 309K, 10° above the RT26 PCM phase transition temperature of 299K. The temperature of the incoming HTF is however one of the parameters varied in the parametric study, though it is always above the phase transition temperature of the PCM for the melting cases.

Figure 3.8 shows the contours of the liquid fraction and the temperature field in the mid vertical plane of the packed bed at different time intervals throughout the melting process.

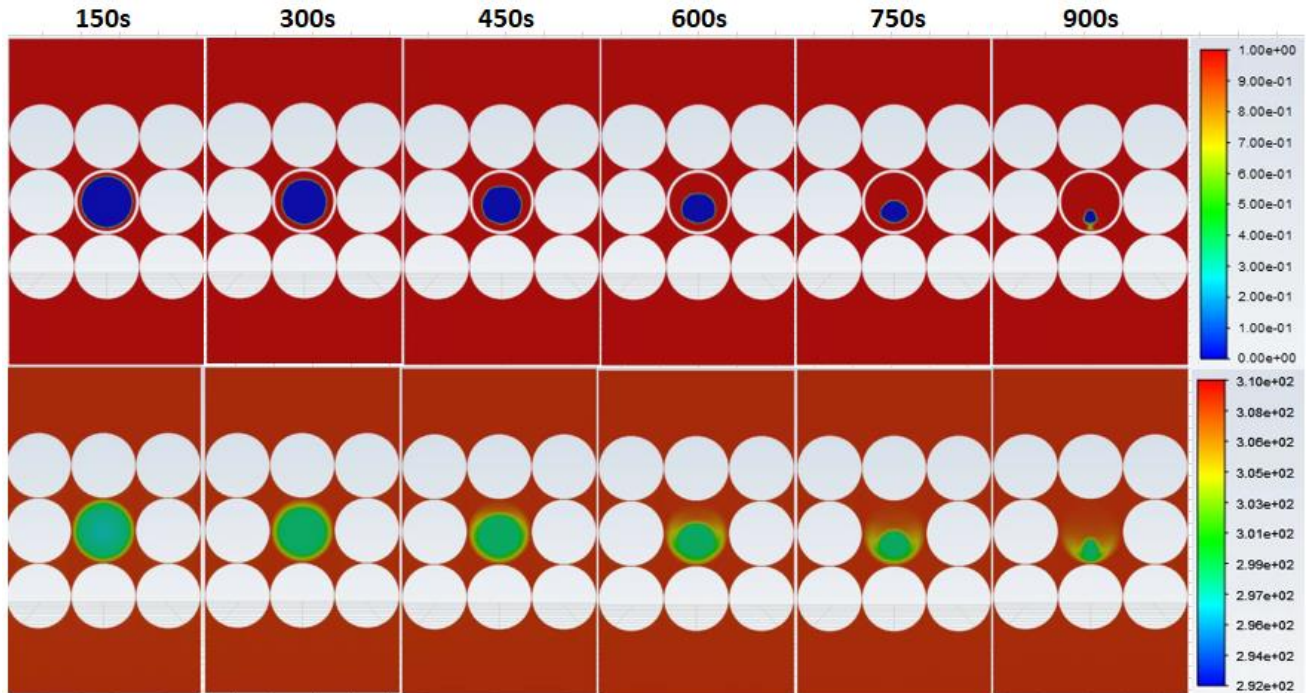


Figure 3.8 - Contours of liquid Fraction (top) and temperature field (bottom) at different time intervals in a packed bed melting process using the translational heat flux method.

As is immediately apparent in figure 3.8, only the central sphere is discretized internally. All remaining spheres are represented as the circular voids seen within the domain. Because the proposed translational heat flux approach is employed, all 27 spheres contained within the packed bed are extracting heat from the heat transfer fluid.

The recorded melting time for the centrally located sphere for this reference case is approximately 975 seconds (16.25 mins). As was the case with the melting times reported in Chapter 2, the volume average liquid fraction of the central sphere is monitored at 60 second intervals throughout the melting process. The midpoint of the interval in which the fully melted condition (100% liquid fraction) appeared is reported as the melting time.

The result is a good approximation of the performance of the entire packed bed system in terms of the PCM charging time, at a very reasonable computational cost. Of significance is that the model is capable of correctly modelling the heat removal from the HTF as if the PCM in all spheres in the packed bed were melting and extracting heat from the surrounding fluid, though the computationally expensive melting process is only being modelled in a single sphere.

These results are provided as a demonstration of the developed method, and for the purpose of acting as a reference point in the following parametric study.

### ***Solidification***

In the case of solidification, the 22mm OD PCM spheres are initialized at a temperature above their phase transition temperature, such that they begin as pure liquids with 100% liquid fraction. Given that the phase transition temperature of the Rubitherm RT26 PCM used is 299K, the PCM spheres are initialized at a uniform temperature of 305K to ensure they begin as pure liquids. Because of this, some sensible cooling occurs before the phase change begins. This sensible cooling period is included in the overall melting time reported in the results.

In a solidification (discharging) process, heat from the PCM spheres is exchanged with the surrounding HTF as the HTF flows through the bed elements, which discharge their thermal energy content to the HTF. To allow for heat transfer out of the PCM spheres, the surrounding HTF is allowed to enter the domain at a constant inlet temperature which is below the PCM melting temperature. In the reference case, the inlet temperature of the surrounding HTF is 289K, 10° below the RT26 PCM phase transition temperature of 299K. The temperature of the incoming HTF is again one of the parameters varied in the parametric study, though it is always below the phase transition temperature of the PCM for the solidification cases.

Figure 3.9 shows the contours of the liquid fraction and the temperature field in the mid vertical plane of the packed bed at different time intervals throughout the solidification process.

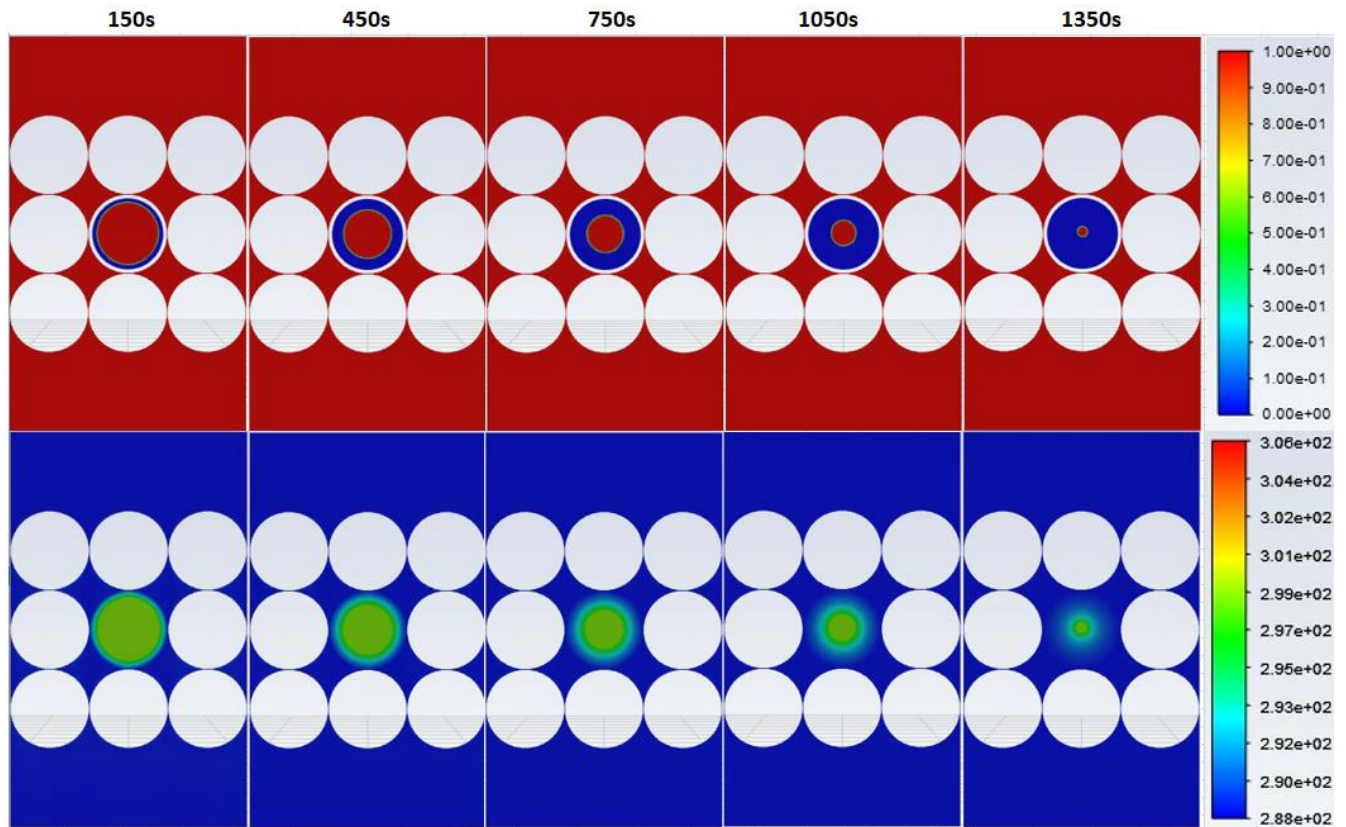


Figure 3.9 - Contours of liquid fraction (top) and temperature field (bottom) at different time intervals in a packed bed solidification process using the translational heat flux method.

As was the case with the melting reference case, only the central sphere is discretized internally. Again, the translational heat flux approach is employed, resulting in the PCM in all 27 spheres supplying heat to the surrounding heat transfer fluid. The recorded solidification time for the centrally located sphere for this reference case is approximately 1425 seconds (23.75 mins). Again, the volume average liquid fraction for the central sphere is monitored at frequent intervals throughout the solidification process. The midpoint of the interval in which the fully solidified condition (0% liquid fraction) appeared is reported as the solidification time.

The result is again a good approximation of the entire packed bed system in terms of the PCM discharging time. The model is capable of successfully modelling the heat release from the PCM to the surrounding HTF as if all PCM spheres in the packed bed were solidifying and exchanging heat with the HTF.



Of interest is the fact that the solidification time is generally higher than the melting time for the same temperature difference between the HTF and the PCM melting temperature. The rationale provided for this difference in charge and discharge rates relates to the heat transfer mechanisms involved in either case. While charging (melting) the heat transfer mechanisms include significant contributions from both conductive and convective heat transfer, whereas in discharging (solidification) the contribution from convective heat transfer is largely suppressed, and conduction is dominant.

Again, these results are provided as a demonstration of the developed method, and for the purpose of acting as a reference point in the following parametric study.

### **3.3.2 Variations in Sphere Diameter**

In this section of the parametric study, the diameter of the PCM encapsulated spheres is varied. The impact of the sphere diameter on the charging and discharging rates of the PCM are compared to the reference cases for both melting and solidification. Each data point represents a unique case in which the fully developed model and translation heat flux approach are applied. The packing arrangement within the bed, the number of encapsulated spheres, and the inlet conditions remain the same as in the reference case, with the bed dimensions scaled down proportionally to the new sphere dimensions.

#### ***Melting***

The four sphere diameters considered for the melting cases are 22mm (reference case), 11mm, 5.5mm and 2.2mm. The cases are run until the central sphere is fully melted (100% liquid fraction). As before the midpoint of the interval in which the fully melted condition appeared is reported as the melting time.

A comparison of the recorded melting time for different sphere diameters is shown in figure 3.10:

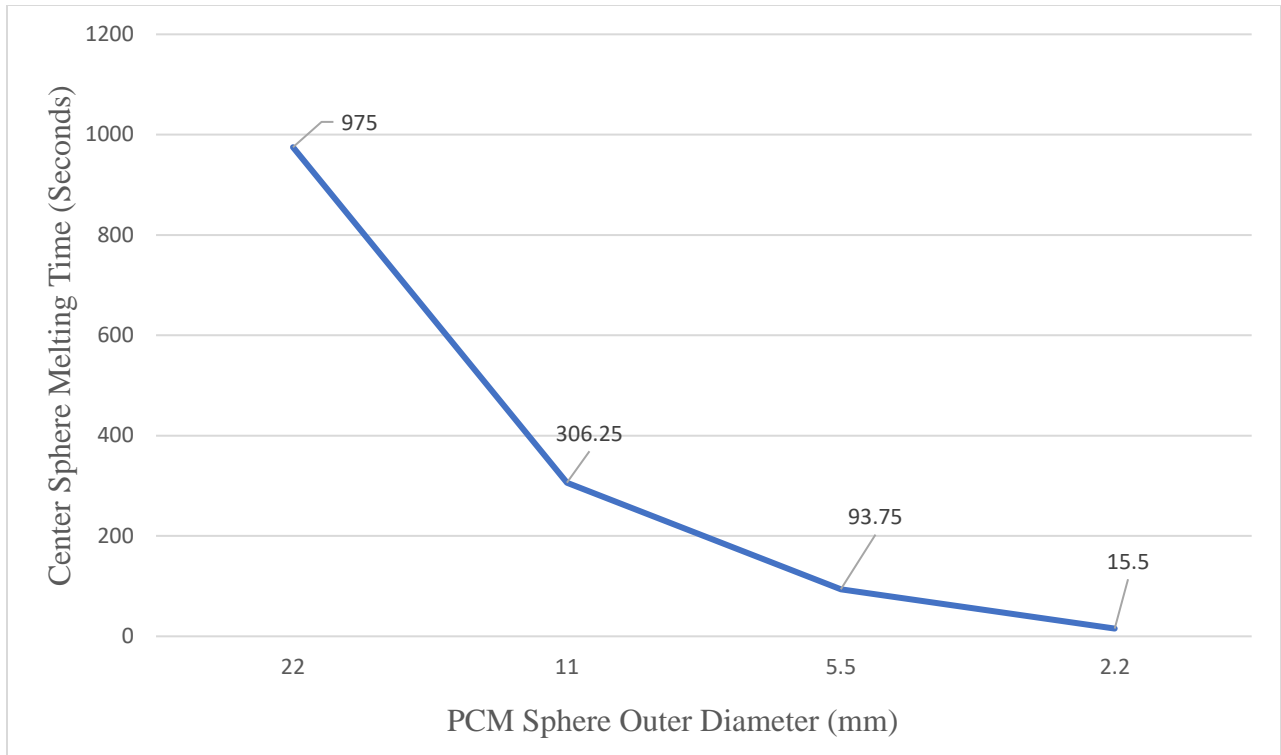


Figure 3.10 - Comparison of central sphere melting time for different sphere diameters.

As would be expected, the smaller sphere diameters correspond to faster melting time than the larger sphere diameters. These findings are consistent those reported in the literature for similar studies investigating sphere diameter [25,26], and consistent with what is expected intuitively.

The trend which can be observed in figure 3.10 suggests that the relationship between melting time and the sphere diameter is nonlinear. A reduction in 50% of the sphere diameter led to greater than 50% reduced melting time in all cases.

Considering the first two cases, ie the change in the sphere diameter from 22mm to 11mm diameter (50% reduction in sphere diameter) melting time was reduced from ~975 seconds to ~306 seconds – a reduction of ~69%. The melting time for the 50% smaller diameter sphere is approximately 3.19 times faster than the original sphere. A reduction from 11mm to 5.5mm diameter reduced the melting time by ~69%, while a reduction from 5.5mm to 2.2mm diameter reduced the melting time by ~83.5%.

## Solidification

The four sphere diameters considered for the solidification cases are 22mm (reference case), 11mm, 5.5mm and 2.2mm. As before the midpoint of the interval in which the fully solidified condition (0% liquid fraction) appeared is reported as the solidification time.

A comparison of the recorded solidification time for different sphere diameters is shown in figure 3.11:

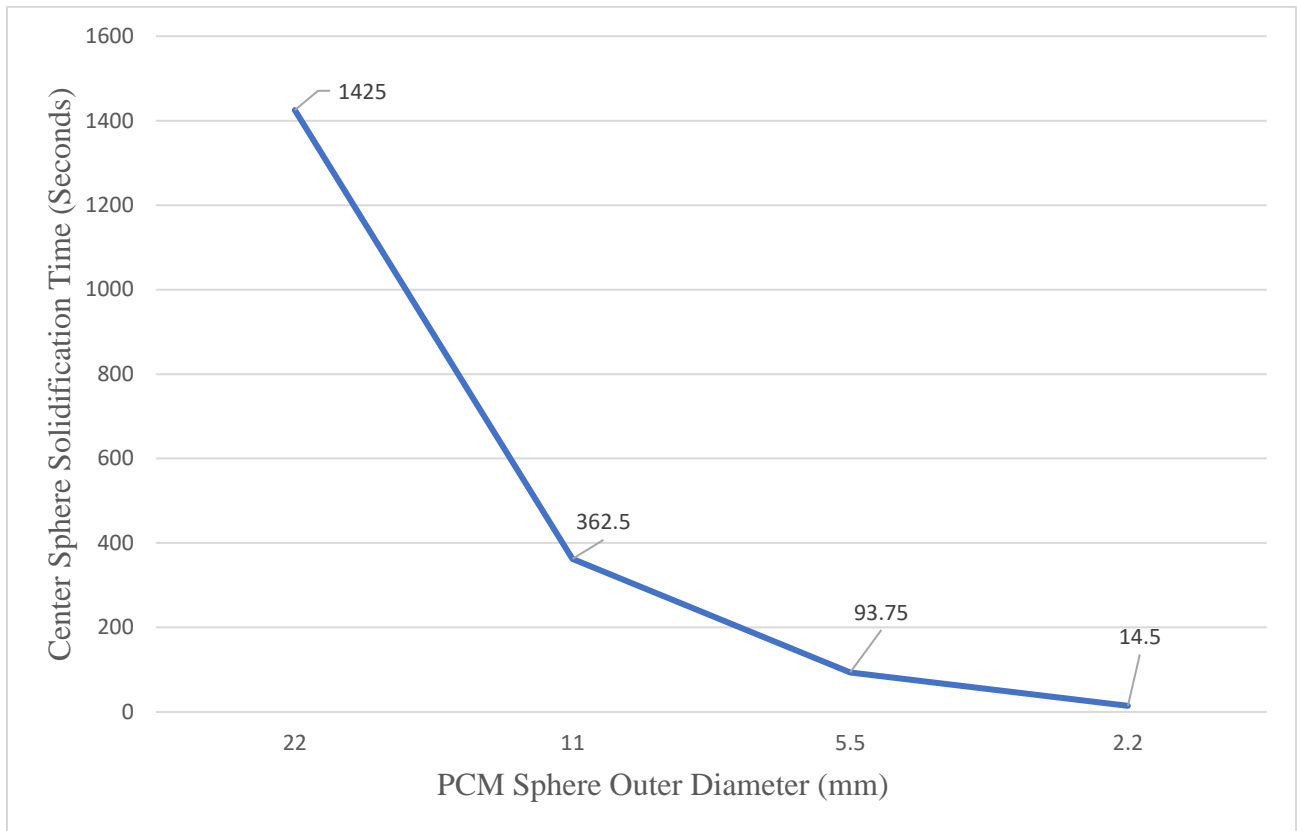


Figure 3.11 - Comparison of central sphere solidification time for different sphere diameters.

Again as is expected, the smaller sphere diameters correspond to faster solidification times than the larger sphere diameters. This is consistent with what is expected intuitively.

The trend seen in figure 11 is, like the one seen in melting, nonlinear. Considering the first two cases, ie the change in the sphere diameter from 22mm to 11mm diameter (50% reduction in sphere diameter), the solidification time reduced from ~1425 seconds to ~362 seconds – a reduction of ~75%. The solidification time for the 50% smaller diameter sphere is approximately 3.93 times

faster than the original sphere. A reduction in diameter from 11mm to 5.5mm reduced the solidification time by ~74%, while a reduction from 5.5mm to 2.2mm reduced the solidification time by ~84.5%.

For practical considerations regarding the design and development of PCM based packed bed LHS systems, the sphere diameter is definitely an important design consideration. A balance should be struck between minimizing the sphere diameter to maximize the charging and discharge rate, while ensuring the spheres are large enough to retain a meaningful thermal energy content and remain in the mixture region for the duration of the charging or discharging process. Manufacturing and fabrication considerations associated to producing the encapsulated PCM spheres and filling the packed bed should also be considered.

### **3.3.3 Variations in Inlet Temperature**

In this section of the parametric study, the inlet temperature of the packed bed heat transfer fluid is varied. The impact of the HTF inlet temperature on the charging and discharging rates of the PCM are compared to the reference case for both melting and solidification. Each case represents a unique condition in which the fully developed model and translation heat flux approach are applied. The sphere diameter is kept constant at 22mm.

#### ***Melting***

The five HTF inlet temperatures considered for the melting cases are 313K, 311K, 309K (reference case), 307K and 305K. As before the midpoint of the interval in which the fully melted condition (100% liquid fraction) appeared is reported as the melting time.

A comparison of the recorded melting time for different HTF inlet temperatures is shown in figure 3.12:

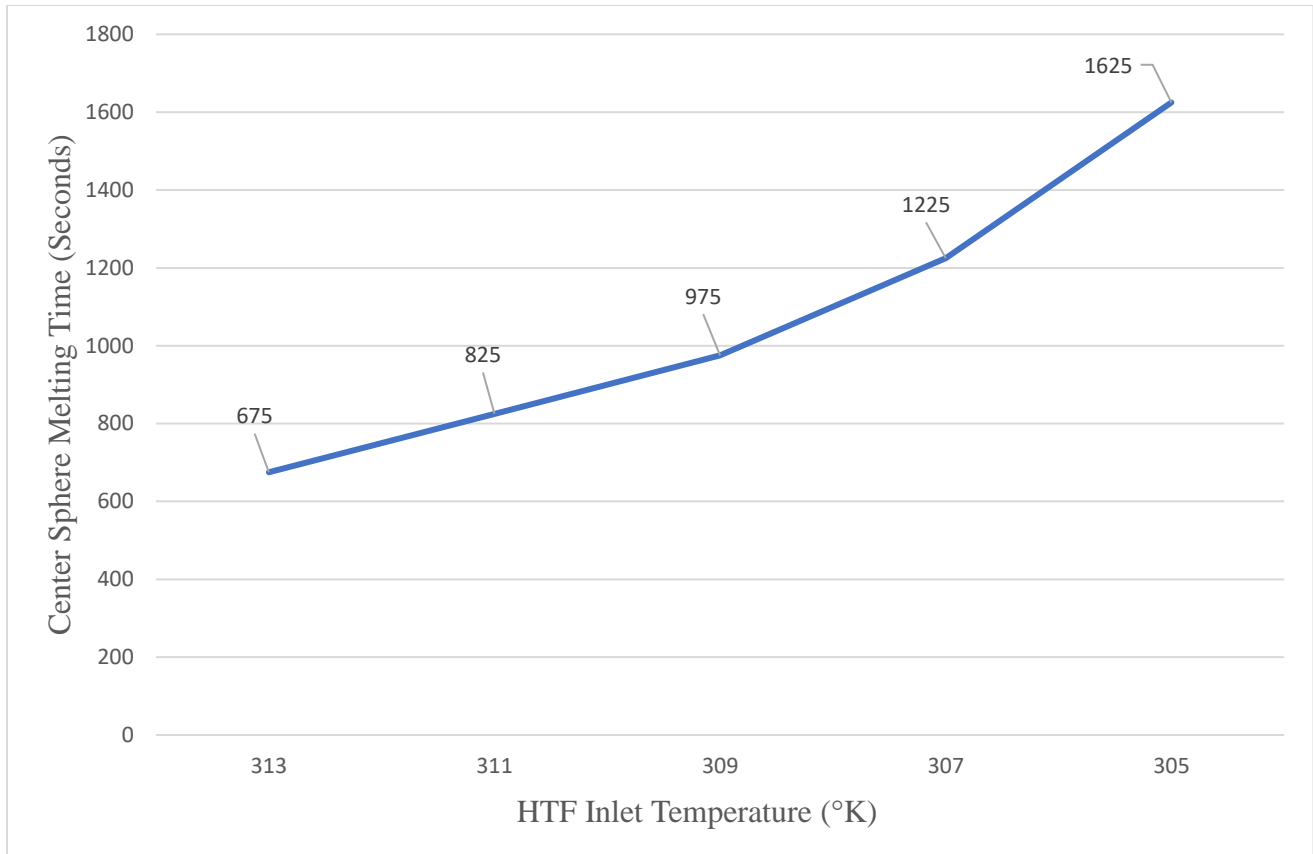


Figure 3.12 - Comparison of central sphere melting time for different HTF inlet temperatures (phase transition temperature 299K).

The findings suggest that an increase in the HTF inlet temperature through the packed bed corresponds to a reduction in melting time, and vice versa. This is consistent with what is reported in the literature for other PCM packed bed studies investigating the impact of heat transfer fluid temperature [38,40,50-51], and with what is expected intuitively.

In terms of the practical implications for designing PCM based packed bed LHS systems, the temperature of the incoming HTF should be as high as possible to ensure fast charging rates. The rate of heat transfer into the PCM spheres (and thus the charging rate) is proportional to the temperature difference between the HTF and the PCM spheres. Maximizing this temperature difference improves the performance of the system in terms of charging rate.

If the temperature of the incoming HTF is not a condition which can be readily modified, then the selection of the PCM material should consider a PCM with a phase transition temperature below the anticipated HTF inlet temperature. This will allow for a temperature difference during the latent heating period to drive heat transfer into the PCM.

The rate of heat transfer into the PCM spheres from the HTF (and thus the charging rate) is proportional to the temperature difference between the HTF and the PCM spheres. Maximizing this temperature difference improves the performance of the system in terms of charging rate.

### ***Solidification***

The five HTF inlet temperatures considered for the solidification cases are 293K, 291K, 289K (reference case), 287K and 285K. As before the midpoint of the interval in which the fully solidified condition (0% liquid fraction) appeared is reported as the solidification time.

A comparison of the recorded solidification time for different HTF inlet temperatures is shown in figure 3.13:

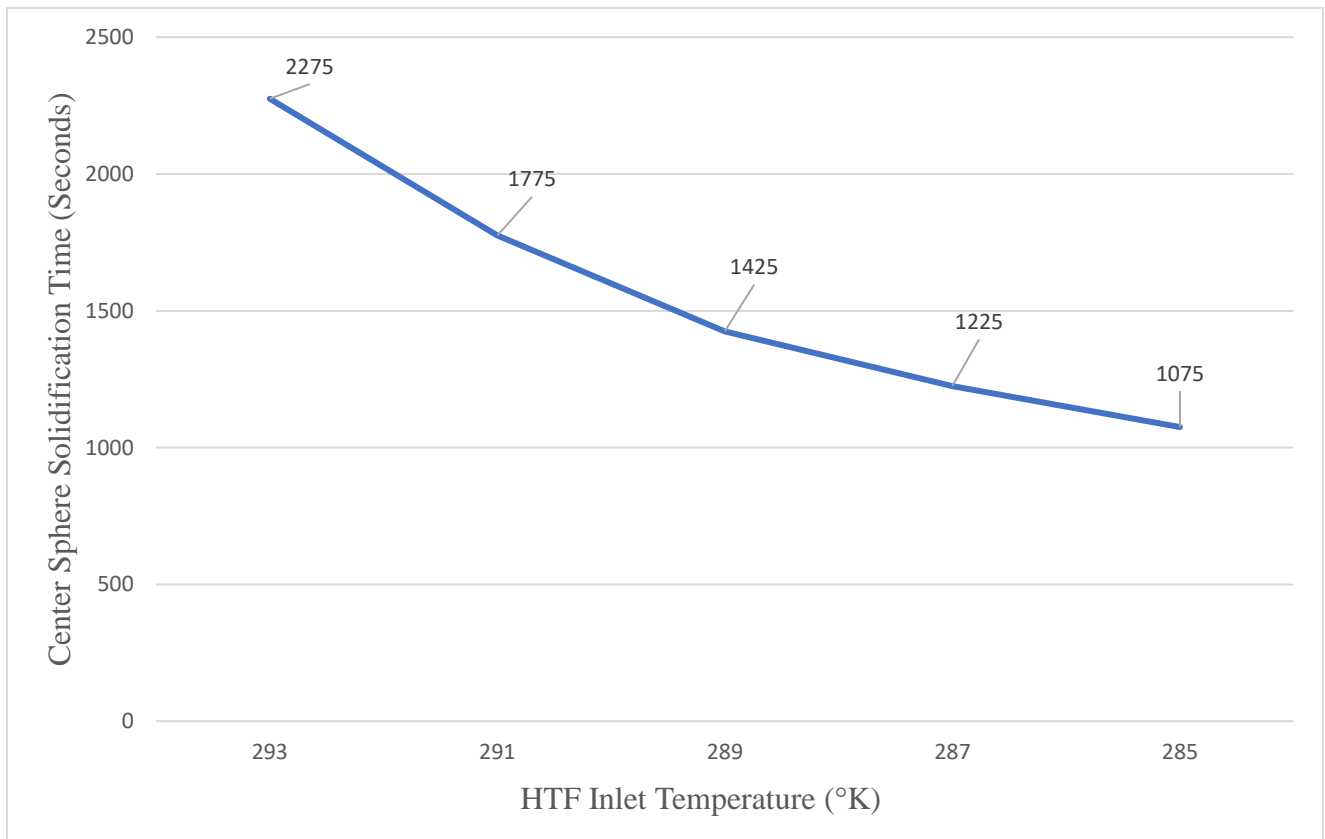


Figure 3.13 - Comparison of central sphere solidification time for different HTF inlet temperatures (phase transition temperature 299°K).

As was the case in melting, the findings suggest that an increase the temperature difference between the HTF and the PCM phase transition temperature corresponds to a faster discharging period. In the case of solidification, a larger temperature difference corresponds to a colder HTF inlet temperature. This is again consistent with what is reported in the literature, and what is expected intuitively.

In terms of the practical implications for designing PCM based packed bed LHS systems, the temperature of the incoming HTF in discharging must be lower than PCM phase transition temperature. This will allow for a temperature difference during the latent heating cooling period to drive heat transfer out of the PCM and into the HTF.

The rate of heat transfer into the HTF from the PCM spheres (and thus the discharging rate) is proportional to the temperature difference between the HTF and the PCM spheres. Maximizing this temperature difference improves the performance of the system in terms of discharging rate.

Again, if the temperature of the incoming HTF is not a condition which can be easily controlled, then the selection of a PCM with an appropriate phase transition temperature is important to ensure the desirable functionality of the system. The PCM should be selected such that the phase transition temperature is well above the temperature of the incoming HTF so that a temperature difference large enough for meaningful heat transfer to occur is present, allowing for adequate discharge rates.

The studies in the preceding sections were provided as a demonstration of the model and the translational heat flux method.

## Chapter 4

### 4. Summary and Conclusions

The outcome of the work successfully delivered upon the original objective of producing a computationally efficient method capable of modelling the performance packed beds containing spherically encapsulated phase change materials.

In order to meet this broader goal, the objectives laid out in section 1.3 regarding the process for developing such a model were achieved.

1) An initial model capable of describing the phase change process of a candidate phase change material was established. This involved the selection of an appropriate PCM, and development of a model capable of accurately describing the phase change process in terms of the melting time, and melting behavior of the selected PCM. Because there is no generally accepted method or procedure for producing such a model, it had to be developed largely independently, with many of the fine details associated to construction of the model being determined through trial and error. The numerical procedures, mesh generation approach, and treatment of the difficult to model phase change processes were determined through exhaustive testing, which lead to many poor results in the process. Producing a model capable of describing the phase change process at all for the given PCM was a great achievement in and of itself.

2) Accurately describing the phase change process involved the calibration of several key process tuning parameters, which were exclusive to the specific PCM and the geometry in which it is contained. These parameters included the thermal expansion coefficient, and mushy zone constant, of which there was no description in the literature for the PCM in question. As such, these parameters had to be parametrized and tuned until the model produced results which were comparable to those obtained in the physical reference experiment. The whole model was validated against the set of experimental results, in order to prove that the model was capable of accurately modelling the phase change process.

3) After the validated model had been established for the geometry considered in the physical reference experiment, the model was extended to another similar geometries of interest, the



encapsulated sphere. The model applied and tested in the new spherical geometry, to ensure that it was capable of producing reasonable results which were consistent with those presented in the literature for similar cases. Again, the delivery of a model that is capable of accurately describing the phase change process of a PCM within a spherical enclosure was a significant accomplishment in and of itself. The results obtained in applying the validated model to a spherical geometry were discussed, in order to illustrate the complex melting behavior.

4) Having successfully developed a model capable of describing the melting and solidification process within a single PCM encapsulated sphere, the model was then extended to the packed bed geometry. At this point the packed bed itself was modelled, with a structured parallel packing arrangement chosen consisting of the spherically encapsulated PCM geometry which had already been established. Here, the novel computationally efficient method for modelling the entire packed bed of spherically encapsulated PCM was introduced, in alignment with the original objective of developing such a method. The method is capable of incorporating the phase change model developed for the spherical geometry, while describing the performance of the packed bed as a whole in a computationally efficient manner. No prior method capable of doing so had been presented in the currently literature. The limitations of the proposed method, and the correction which can be used to improve the accuracy in certain situations were identified.

5) Having established a computationally efficient method for the treatment of the packed bed that can be used in conjunction with the high-fidelity phase change model for the single sphere, the method was then demonstrated via a parametric study. Several cases were run to demonstrate the viability of the method in producing accurate results in terms of the performance of the packed bed as a whole. The method's ability to support the development of spherically encapsulated PCM packed bed thermal energy storage devices for practical design purposes was demonstrated.

In conclusion, a novel computationally efficient method for modelling both the melting and solidification processes in packed beds of spherically encapsulated phase change materials has been introduced. The method involves measuring heat transfer conditions on the exterior surface of a fully discretized centrally located PCM sphere undergoing the phase change process, and applying the measured values as boundary conditions on surrounding spheres, which do not need to be discretized internally. The numerical model was calibrated against experimental data before being expanded to other geometries of interest. The resulting procedure makes it practical to

conduct accurate phase change modelling of entire packed beds of encapsulated PCM, without implementing computationally intensive schemes that involve simulating the phase change process in all spheres in the packed bed.

#### **4.1 Recommendations for Future Work**

Some recommendations for future work and research on the subject numerically modelling packed beds of spherically encapsulated PCM will be made:

The heat flux correction proposed for the computationally efficient method is lacking in robustness. It is likely that a better correction could be provided for the heat flux of a sphere at any given depth in the bed, as a function of the expected liquid fraction of spheres at different depths in the bed. The development of an improved correction could improve the applicability of the method for very long packed beds, where the temperature change in the heat transfer fluid is significant.

The method can be readily applied to other already validated models of spherically encapsulated PCM, to simulate their performance within a packed bed. Validated models for PCMs which undergo phase change at different temperature exist in the literature, and the method could be immediately used in conjunction with such models to study the performance of these other phase change materials in packed beds. The general process described for validating the PCM-specific model in the present study can also be used to guide the development of valid models for other PCMs, for which validated models do not yet exist.

The model should be used to support the development of thermal energy storage devices which employ packed beds of spherically encapsulated PCM. These devices can be used to enhance the energy efficiency of many systems in industry, and provide valuable waste heat recovery for many existing industrial processes. Further parametric studies can be conducted using the model, to investigate the impacts of many different important design parameters in packed beds containing spherically encapsulated PCM. The influence of parameters such as encapsulating shell material, heat transfer fluid flow rates, heat transfer fluid material, and different packing configurations within packed beds could be studied using the method.

## Bibliography

- [1] “U.S. Energy Information Administration - EIA - Independent Statistics and Analysis,” Hourly electricity consumption varies throughout the day and across seasons - Today in Energy - U.S. Energy Information Administration (EIA). [Online]. Available: <https://www.eia.gov/todayinenergy/detail.php?id=42915#:~:text=Electricity%20consumption%20typically%20cycles%20each,down%20during%20late%20evening%20hours>. [Accessed: 15-Nov-2022].
- [2] Denholm, P., King, J. C., Kutcher, C. F., & Wilson, P. P. H. (2012). Decarbonizing the electric sector: Combining renewable and nuclear energy using thermal storage. *Energy Policy*, 44, 301–311. <https://doi.org/10.1016/j.enpol.2012.01.055>
- [3] R. Sioshansi and P. Denholm. (2010). The value of concentrating solar power and thermal energy storage. *IEEE Transactions on Sustainable Energy*, 1 (3) pp. 173-183
- [4] Alva, G., Lin, Y., & Fang, G. (2018). An overview of thermal energy storage systems. *Energy*, 144, 341–378. <https://doi.org/10.1016/j.energy.2017.12.037>
- [5] Pelay, U., Luo, L., Fan, Y., Stitou, D., & Rood, M. (2017). Thermal energy storage systems for concentrated solar power plants. *Renewable and Sustainable Energy Reviews*, 79(May), 82–100. <https://doi.org/10.1016/j.rser.2017.03.139>
- [6] A. S. Fleischer, in *Thermal Energy Storage Using Phase Change Materials Fundamentals and Applications*, Cham: Springer International Publishing, 2015.
- [7] A. Sharma, V. V. Tyagi, C. R. Chen, and D. Buddhi, “Review on thermal energy storage with phase change materials and applications,” *Renew. Sustain. Energy Rev.*, vol. 13, no. 2, pp. 318–345, 2009, doi: 10.1016/j.rser.2007.10.005.
- [8] “Paraffin hydrocarbon,” *Encyclopædia Britannica*. [Online]. Available: <https://www.britannica.com/science/paraffin-hydrocarbon>. [Accessed: 15-Nov-2022].
- [9] S. Rousseau, “What Is a Hydrated Salt?,” *Sciencing*, 02-Mar-2019. [Online]. Available: <https://sciencing.com/hydrated-salt-8700669.html>. [Accessed: 15-Nov-2022].
- [10] W. Su, J. Darkwa, and G. Kokogiannakis, “Review of solid-liquid phase change materials and their encapsulation technologies,” *Renew. Sustain. Energy Rev.*, vol. 48, pp. 373–391, 2015, doi: 10.1016/j.rser.2015.04.044.
- [11] B. P. Jelle and S. E. Kalnæs, *Phase Change Materials for Application in Energy-Efficient Buildings*. Elsevier Ltd, 2017.
- [12] Castell, A., & Solé, C. (2015). An overview on design methodologies for liquid-solid PCM storage systems. *Renewable and Sustainable Energy Reviews*, 52, 289–307. <https://doi.org/10.1016/j.rser.2015.07.119>
- [13] Choi, D. H., Lee, J., Hong, H., & Kang, Y. T. (2014). Thermal conductivity and heat transfer performance enhancement of phase change materials (PCM) containing carbon additives

for heat storage application. *International Journal of Refrigeration*, 42, 112–120.  
<https://doi.org/10.1016/j.ijrefrig.2014.02.004>

[14] Dhaidan, N. S., Khodadadi, J. M., Al-Hattab, T. A., & Al-Mashat, S. M. (2013). Experimental and numerical investigation of melting of NePCM inside an annular container under a constant heat flux including the effect of eccentricity. *International Journal of Heat and Mass Transfer*, 67, 455–468. <https://doi.org/10.1016/j.ijheatmasstransfer.2013.08.002>

[15] Tay, N. H. S., Bruno, F., & Belusko, M. (2013). Comparison of pinned and finned tubes in a phase change thermal energy storage system using CFD. *Applied Energy*, 104, 79–86.  
<https://doi.org/10.1016/j.apenergy.2012.10.040>

[16] R. H. Perry, “Reactors,” in *Perry's Chemical Engineers' Handbook*, New York, NY: McGraw Hill, 2019.

[17] Subramanian, R. S. (2016). *Flow through Packed and Fluidized Beds*. 1–6.

[18] Al-Abidi, A. A., Bin Mat, S., Sopian, K., Sulaiman, M. Y., & Mohammed, A. T. (2013). CFD applications for latent heat thermal energy storage: A review. *Renewable and Sustainable Energy Reviews*, 20, 353–363. <https://doi.org/10.1016/j.rser.2012.11.079>

[19] Stefan, J. Über die Theorie der Eisbildung, insbesondere über die Eisbildung im Polarmeere. *Ann. Phys.* 1981, 278, 269–286

[20] Kenisarin, M. M., Mahkamov, K., Costa, S. C., & Makhkamova, I. (2020). Melting and solidification of PCMs inside a spherical capsule: A critical review. *Journal of Energy Storage*, 27(August 2019), 101082. <https://doi.org/10.1016/j.est.2019.101082>

[21] Khodadadi, J.M. and Zhang, Y. (2001). [Effects of buoyancy-driven convection on melting within spherical containers](#). *Int. J. Heat Mass Transf.*, 44 (8) (2001 Apr 1), pp. 1605-1618

[22] Tan, F. L. (2008). Constrained and unconstrained melting inside a sphere. *International Communications in Heat and Mass Transfer*, 35(4), 466–475.  
<https://doi.org/10.1016/j.icheatmasstransfer.2007.09.008>

[23] Tan, F. L., Hosseinizadeh, S. F., Khodadadi, J. M., & Fan, L. (2009). Experimental and computational study of constrained melting of phase change materials (PCM) inside a spherical capsule. *International Journal of Heat and Mass Transfer*, 52(15–16), 3464–3472.  
<https://doi.org/10.1016/j.ijheatmasstransfer.2009.02.043>

[24] Galione, P. A., Lehmkuhl, O., Rigola, J., & Oliva, A. (2015). Fixed-grid numerical modeling of melting and solidification using variable thermo-physical properties - Application to the melting of n-Octadecane inside a spherical capsule. *International Journal of Heat and Mass Transfer*, 86, 721–743. <https://doi.org/10.1016/j.ijheatmasstransfer.2015.03.033>

[25] Li, W., Li, S. G., Guan, S., Wang, Y., Zhang, X., & Liu, X. (2017). Numerical study on melt fraction during melting of phase change material inside a sphere. *International Journal of Hydrogen Energy*, 42(29), 18232–18239. <https://doi.org/10.1016/j.ijhydene.2017.04.136>

- [26] Sattari, H., Mohebbi, A., Afsahi, M. M., & Azimi Yancheshme, A. (2017). Simulation par MFN du processus de fusion des matériaux à changement de phase dans une capsule sphérique. *International Journal of Refrigeration*, 73, 209–218. <https://doi.org/10.1016/j.ijrefrig.2016.09.007>
- [27] Soni, V., Kumar, A., & Jain, V. K. (2018). Modeling of PCM melting: Analysis of discrepancy between numerical and experimental results and energy storage performance. *Energy*, 150, 190–204. <https://doi.org/10.1016/j.energy.2018.02.097>
- [28] Mawire, A., McPherson, M., van den Heetkamp, R. R. J., & Taole, S. H. (2010). Experimental volumetric heat transfer characteristics between oil and glass pebbles in a small glass tube storage. *Energy*, 35(3), 1256–1263. <https://doi.org/10.1016/j.energy.2009.11.005>
- [29] Mawire, A., & Taole, S. H. (2011). A comparison of experimental thermal stratification parameters for an oil/pebble-bed thermal energy storage (TES) system during charging. *Applied Energy*, 88(12), 4766–4778. <https://doi.org/10.1016/j.apenergy.2011.06.019>
- [30] Okello, D., Nydal, O. J., & Banda, E. J. K. (2014). Experimental investigation of thermal de-stratification in rock bed TES systems for high temperature applications. *Energy Conversion and Management*, 86, 125–131. <https://doi.org/10.1016/j.enconman.2014.05.005>
- [31] Anderson, R., Shiri, S., Bindra, H., & Morris, J. F. (2014). Experimental results and modeling of energy storage and recovery in a packed bed of alumina particles. *Applied Energy*, 119, 521–529. <https://doi.org/10.1016/j.apenergy.2014.01.030>
- [32] Bruch, A., Fourmigué, J. F., & Couturier, R. (2014). Experimental and numerical investigation of a pilot-scale thermal oil packed bed thermal storage system for CSP power plant. *Solar Energy*, 105, 116–125. <https://doi.org/10.1016/j.solener.2014.03.019>
- [33] Rodat, S., Bruch, A., Dupassieux, N., & Mouchid, N. El. (2015). Unique Fresnel Demonstrator Including ORC and Thermocline Direct Thermal Storage: Operating Experience. *Energy Procedia*, 69, 1667–1675. <https://doi.org/10.1016/j.egypro.2015.03.127>
- [34] Cascetta, M., Cau, G., Puddu, P., & Serra, F. (2016). A comparison between CFD simulation and experimental investigation of a packed-bed thermal energy storage system. *Applied Thermal Engineering*, 98, 1263–1272. <https://doi.org/10.1016/j.applthermaleng.2016.01.019>
- [35] Hoffmann, J. F., Fasquelle, T., Goetz, V., & Py, X. (2016). A thermocline thermal energy storage system with filler materials for concentrated solar power plants: Experimental data and numerical model sensitivity to different experimental tank scales. *Applied Thermal Engineering*, 100, 753–761. <https://doi.org/10.1016/j.applthermaleng.2016.01.110>
- [36] Bruch, A., Molina, S., Esence, T., Fourmigué, J. F., & Couturier, R. (2017). Experimental investigation of cycling behaviour of pilot-scale thermal oil packed-bed thermal storage system. *Renewable Energy*, 103, 277–285. <https://doi.org/10.1016/j.renene.2016.11.029>

- [37] Esence, T., Bruch, A., Molina, S., Stutz, B., & Fourmigué, J. F. (2017). A review on experience feedback and numerical modeling of packed-bed thermal energy storage systems. *Solar Energy*, 153, 628–654. <https://doi.org/10.1016/j.solener.2017.03.032>
- [38] Li, C., Li, Q., & Ding, Y. (2019). Investigation on the thermal performance of a high temperature packed bed thermal energy storage system containing carbonate salt based composite phase change materials. *Applied Energy*, 247(November 2018), 374–388. <https://doi.org/10.1016/j.apenergy.2019.04.031>
- [39] Li, C., Li, Q., & Ding, Y. (2019). Carbonate salt based composite phase change materials for medium and high temperature thermal energy storage: From component to device level performance through modelling. *Renewable Energy*, 140, 140–151. <https://doi.org/10.1016/j.renene.2019.03.005>
- [40] Li, M. J., Jin, B., Ma, Z., & Yuan, F. (2018). Experimental and numerical study on the performance of a new high-temperature packed-bed thermal energy storage system with macroencapsulation of molten salt phase change material. *Applied Energy*, 221(March), 1–15. <https://doi.org/10.1016/j.apenergy.2018.03.156>
- [41] Wei, J., Kawaguchi, Y., Hirano, S., & Takeuchi, H. (2005). Study on a PCM heat storage system for rapid heat supply. *Applied Thermal Engineering*, 25(17–18), 2903–2920. <https://doi.org/10.1016/j.applthermaleng.2005.02.014>
- [42] Yang, J., Wang, Q., Zeng, M., & Nakayama, A. (2010). Computational study of forced convective heat transfer in structured packed beds with spherical or ellipsoidal particles. *Chemical Engineering Science*, 65(2), 726–738. <https://doi.org/10.1016/j.ces.2009.09.026>
- [43] Chen, L., Lee, W., & Lee, J. (2017). Analysis of the thermal field and heat transfer characteristics of pebble beds packed in a face-centered cubic structure. *Applied Thermal Engineering*, 121, 473–483. <https://doi.org/10.1016/j.applthermaleng.2017.04.113>
- [44] Zhang, H. W., Zhou, Q., Xing, H. L., & Muhlhaus, H. (2011). A DEM study on the effective thermal conductivity of granular assemblies. *Powder Technology*, 205(1–3), 172–183. <https://doi.org/10.1016/j.powtec.2010.09.008>
- [45] He, X., Qiu, J., Wang, W., Hou, Y., Ayyub, M., & Shuai, Y. (2022). A review on numerical simulation, optimization design and applications of packed-bed latent thermal energy storage system with spherical capsules. *Journal of Energy Storage*, 51(April), 104555. <https://doi.org/10.1016/j.est.2022.104555>
- [46] Xia, L., Zhang, P., & Wang, R. Z. (2010). Numerical heat transfer analysis of the packed bed latent heat storage system based on an effective packed bed model. *Energy*, 35(5), 2022–2032. <https://doi.org/10.1016/j.energy.2010.01.018>
- [47] Erek, A., & Dincer, I. (2009). Numerical heat transfer analysis of encapsulated ice thermal energy storage system with variable heat transfer coefficient in downstream. *International Journal of Heat and Mass Transfer*, 52(3–4), 851–859. <https://doi.org/10.1016/j.ijheatmasstransfer.2008.06.024>

- [48] Arkar, C., Vidrih, B., & Medved, S. (2007). Efficiency of free cooling using latent heat storage integrated into the ventilation system of a low energy building. *International Journal of Refrigeration*, 30(1), 134–143. <https://doi.org/10.1016/j.ijrefrig.2006.03.009>
- [49] Arkar, C., & Medved, S. (2005). Influence of accuracy of thermal property data of a phase change material on the result of a numerical model of a packed bed latent heat storage with spheres. *Thermochimica Acta*, 438(1–2), 192–201. <https://doi.org/10.1016/j.tca.2005.08.032>
- [50] Seeniraj, R. V., & Lakshmi Narasimhan, N. (2005). The thermal response of a cold LHTS unit with heat leak through side walls. *International Communications in Heat and Mass Transfer*, 32(10), 1375–1386. <https://doi.org/10.1016/j.icheatmasstransfer.2005.07.011>
- [51] Benmansour, A., Hamdan, M. A., & Bengueuddach, A. (2006). Experimental and numerical investigation of solid particles thermal energy storage unit. *Applied Thermal Engineering*, 26(5–6), 513–518. <https://doi.org/10.1016/j.applthermaleng.2005.07.014>
- [52] Ansys® Fluent Theory Guide, Release 12.0, Help System. ANSYS, Inc.
- [53] Ansys® Workbench, Release 2020 R1, ANSYS, Inc.
- [54] Teather, K. & Siddiqui, K. (2021). Transient flow behavior of a PCM encased in a circular domain. *Fluids Engineering Division Summer Conference*, August 10-12, 2021 (Virtual).
- [55] Rubitherm. (2020). RT26 Data Sheet. Rubitherm Technologies GmbH. [https://www.rubitherm.eu/media/products/datasheets/Techdata\\_RT26\\_EN\\_06082018.PDF](https://www.rubitherm.eu/media/products/datasheets/Techdata_RT26_EN_06082018.PDF)
- [56] Ferrer, G., Gschwander, S., Solé, A., Barreneche, C., Fernández, A. I., Schossig, P., & Cabeza, L. F. (2017). Empirical equation to estimate viscosity of paraffin. *Journal of Energy Storage*, 11, 154–161. <https://doi.org/10.1016/j.est.2017.03.002>
- [57] Altuglas International. (2006). Typical Physical Properties Plexiglas® V045i Acrylic Resin. <https://web.archive.org/web/20070223072449/http://www.plexiglas.com/tds/4b.pdf>
- [58] Pointwise Version 18.3, Release 2019 R1. Cadence, Inc.



## Appendices

### Appendix A – PCM Property Tables

Appendix A1 – Transition temperature and latent heat capacity of some paraffin PCMs [7]

No. of carbon atoms	Melting point (°C)	Latent heat of fusion (kJ/kg)
14	5.5	228
15	10	205
16	16.7	237.1
17	21.7	213
18	28.0	244
19	32.0	222
20	36.7	246
21	40.2	200
22	44.0	249
23	47.5	232
24	50.6	255
25	49.4	238
26	56.3	256
27	58.8	236
28	61.6	253
29	63.4	240
30	65.4	251
31	68.0	242
32	69.5	170
33	73.9	268
34	75.9	269



Appendix A2 – Transition temperature and latent heat capacity of some fatty acids []

Material	Formula	Melting point (°C)	Latent heat (kJ/kg)
Acetic acid	CH <sub>3</sub> COOH	16.7	184
Polyethylene glycol 600	H(OC <sub>2</sub> H <sub>2</sub> ) <sub>n</sub> -OH	20–25	146
Capric acid	CH <sub>3</sub> (CH <sub>2</sub> ) <sub>8</sub> -COOH	36	152
Eladic acid	C <sub>8</sub> H <sub>7</sub> C <sub>9</sub> H <sub>16</sub> -COOH	47	218
Lauric acid	CH <sub>3</sub> (CH <sub>2</sub> ) <sub>10</sub> -COOH	49	178
Pentadecanoic acid	CH <sub>3</sub> (CH <sub>2</sub> ) <sub>13</sub> -COOH	52.5	178
Tristearin	(C <sub>17</sub> H <sub>35</sub> COO)C <sub>3</sub> H <sub>5</sub>	56	191
Myristic acid	CH <sub>3</sub> (CH <sub>2</sub> ) <sub>12</sub> -COOH	58	199
Palmitic acid	CH <sub>3</sub> (CH <sub>2</sub> ) <sub>14</sub> -COOH	55	163
Stearic acid	CH <sub>3</sub> (CH <sub>2</sub> ) <sub>16</sub> -COOH	69.4	199
Acetamide	CH <sub>3</sub> CONH <sub>2</sub>	81	241
Methyl fumarate	(CHCO <sub>2</sub> NH <sub>3</sub> ) <sub>2</sub>	102	242

Appendix A3 – Transition temperature and latent heat capacity of some salt hydrates [10]

Name	Chemical formula	$T_m$ (°C)	$H$ (kJ/kg)
Lithium chlorate trihydrate	$\text{LiClO}_3 \cdot 3\text{H}_2\text{O}$	8	253
Zinc chloride trihydrate	$\text{ZnCl}_2 \cdot 3\text{H}_2\text{O}$	10	n.a.
Ammonium chloride Sodium sulphate decahydrate	$\text{NH}_4\text{Cl} \cdot \text{Na}_2\text{SO}_4 \cdot 10\text{H}_2\text{O}$	11	163
Dipotassium hydrogen phosphate hexahydrate	$\text{K}_2\text{HPO}_4 \cdot 6\text{H}_2\text{O}$	14	109
Sodium chloride Sodium sulphate decahydrate	$\text{NaCl} \cdot \text{Na}_2\text{SO}_4 \cdot 10\text{H}_2\text{O}$	18	286
Potassium fluoride tetrahydrate	$\text{KF} \cdot 4\text{H}_2\text{O}$	18	330
Dipotassium hydrogen phosphate tetrahydrate	$\text{K}_2\text{HPO}_4 \cdot 4\text{H}_2\text{O}$	18.5	231
Iron bromide hexahydrate	$\text{FeBr}_3 \cdot 6\text{H}_2\text{O}$	21	105
Manganese nitrate hexahydrate	$\text{Mn}(\text{NO}_3)_2 \cdot 6\text{H}_2\text{O}$	25.5	125.9–148
Lithium metaborate octahydrate	$\text{LiBO}_2 \cdot 8\text{H}_2\text{O}$	25.7	289
Calcium chloride hexahydrate	$\text{CaCl}_2 \cdot 6\text{H}_2\text{O}$	29–30	170–192
Calcium chloride dodecahydrate	$\text{CaCl}_2 \cdot 12\text{H}_2\text{O}$	29.8	174
Lithium nitrate trihydrate	$\text{LiNO}_3 \cdot 3\text{H}_2\text{O}$	30	189–296
Lithium nitrate dihydrate	$\text{LiNO}_3 \cdot 2\text{H}_2\text{O}$	30	296
Sodium sulphate decahydrate	$\text{Na}_2\text{SO}_4 \cdot 10\text{H}_2\text{O}$	32	251–254
Sodium carbonate decahydrate	$\text{Na}_2\text{CO}_3 \cdot 10\text{H}_2\text{O}$	32	267
Iron potassium alum	$\text{KFe}(\text{SO}_4)_2 \cdot 12\text{H}_2\text{O}$	33	173
Calcium bromide hexahydrate	$\text{CaBr}_2 \cdot 6\text{H}_2\text{O}$	34	115–138
Lithium bromide dihydrate	$\text{LiBr} \cdot 2\text{H}_2\text{O}$	34	124
Dipotassium hydrogen phosphate dodecahydrate	$\text{Na}_2\text{HPO}_4 \cdot 12\text{H}_2\text{O}$	35–40	256–281
Zinc nitrate hexahydrate	$\text{Zn}(\text{NO}_3)_2 \cdot 6\text{H}_2\text{O}$	36	134–147
Manganese nitrate tetrahydrate	$\text{Mn}(\text{NO}_3)_2 \cdot 4\text{H}_2\text{O}$	37	115
Iron chloride hexahydrate	$\text{FeCl}_3 \cdot 6\text{H}_2\text{O}$	37	223
Calcium chloride tetrahydrate	$\text{CaCl}_2 \cdot 4\text{H}_2\text{O}$	39	158
Copper sulphate heptahydrate	$\text{CuSO}_4 \cdot 7\text{H}_2\text{O}$	40.7	171
Potassium fluoride dihydrate	$\text{KF} \cdot 2\text{H}_2\text{O}$	42	162–266
Magnesium iodide octahydrate	$\text{MgI}_2 \cdot 8\text{H}_2\text{O}$	42	133
Calcium iodide hexahydrate	$\text{CaI}_2 \cdot 6\text{H}_2\text{O}$	42	162
Calcium nitrate tetrahydrate	$\text{Ca}(\text{NO}_3)_2 \cdot 4\text{H}_2\text{O}$	43–47	106–140
Zinc nitrate tetrahydrate	$\text{Zn}(\text{NO}_3)_2 \cdot 4\text{H}_2\text{O}$	45	110
Tripotassium phosphate tribasic heptahydrate	$\text{K}_3\text{PO}_4 \cdot 7\text{H}_2\text{O}$	45	145
Dipotassium hydrogen phosphate heptahydrate	$\text{K}_2\text{HPO}_4 \cdot 7\text{H}_2\text{O}$	45	145
Iron nitrate nonahydrate	$\text{Fe}(\text{NO}_3)_3 \cdot 9\text{H}_2\text{O}$	47	155–190
Magnesium nitrate tetrahydrate	$\text{Mg}(\text{NO}_3)_2 \cdot 4\text{H}_2\text{O}$	47	142
Sodium sulphite pentahydrate	$\text{Na}_2\text{SiO}_3 \cdot 5\text{H}_2\text{O}$	48	168
Sodium sulphite tetrahydrate	$\text{Na}_2\text{SiO}_3 \cdot 4\text{H}_2\text{O}$	48	168
Dipotassium hydrogen phosphate heptahydrate	$\text{Na}_2\text{HPO}_4 \cdot 7\text{H}_2\text{O}$	48	135–170
Sodium thiosulfate pentahydrate	$\text{Na}_2\text{S}_2\text{O}_3 \cdot 5\text{H}_2\text{O}$	48	209
Dipotassium hydrogen phosphate trihydrate	$\text{K}_2\text{HPO}_4 \cdot 3\text{H}_2\text{O}$	48	99
Magnesium sulphate heptahydrate	$\text{MgSO}_4 \cdot 7\text{H}_2\text{O}$	48.5	202
Calcium nitrate trihydrate	$\text{Ca}(\text{NO}_3)_2 \cdot 3\text{H}_2\text{O}$	51	104
Sodium nitrate hexahydrate	$\text{Na}(\text{NO}_3)_2 \cdot 6\text{H}_2\text{O}$	53	158
Zinc nitrate dihydrate	$\text{Zn}(\text{NO}_3)_2 \cdot 2\text{H}_2\text{O}$	55	68
Iron chloride dihydrate	$\text{FeCl}_3 \cdot 2\text{H}_2\text{O}$	56	90
Cobaltous nitrate hexahydrate	$\text{Co}(\text{NO}_3)_2 \cdot 6\text{H}_2\text{O}$	57	115
Nick nitrate hexahydrate	$\text{Ni}(\text{NO}_3)_2 \cdot 6\text{H}_2\text{O}$	57	169
Manganese chloride tetrahydrate	$\text{MnCl}_2 \cdot 4\text{H}_2\text{O}$	58	151
Sodium acetate trihydrate	$\text{CH}_3\text{COONa} \cdot 3\text{H}_2\text{O}$	58	270–290
Lithium acetate dihydrate	$\text{LiC}_2\text{H}_3\text{O}_2 \cdot 2\text{H}_2\text{O}$	58	251–377
Magnesium chloride tetrahydrate	$\text{MgCl}_2 \cdot 4\text{H}_2\text{O}$	58	178
Sodium hydroxide monohydrate	$\text{NaOH} \cdot \text{H}_2\text{O}$	58	272
Cadmium nitrate tetrahydrate	$\text{Cd}(\text{NO}_3)_2 \cdot 4\text{H}_2\text{O}$	59	98
Cadmium nitrate monohydrate	$\text{Cd}(\text{NO}_3)_2 \cdot 1\text{H}_2\text{O}$	59.5	107
Iron nitrate hexahydrate	$\text{Fe}(\text{NO}_3)_2 \cdot 6\text{H}_2\text{O}$	60.5	126
Sodium aluminium sulphate dodecahydrate	$\text{NaAl}(\text{SO}_4)_2 \cdot 12\text{H}_2\text{O}$	61	181
Sodium aluminium sulphate decahydrate	$\text{NaAl}(\text{SO}_4)_2 \cdot 10\text{H}_2\text{O}$	61	181
Ferrous sulphate heptahydrate	$\text{FeSO}_4 \cdot 7\text{H}_2\text{O}$	64	200
Sodium phosphate dodecahydrate	$\text{Na}_3\text{PO}_4 \cdot 12\text{H}_2\text{O}$	65	190
Sodium borate decahydrate	$\text{Na}_2\text{B}_4\text{O}_7 \cdot 10\text{H}_2\text{O}$	68	n.a.
Lithium ethanoate dihydrate	$\text{LiCH}_3\text{COO} \cdot 2\text{H}_2\text{O}$	70	150–251
Sodium polyphosphate decahydrate	$\text{Na}_2\text{P}_2\text{O}_7 \cdot 10\text{H}_2\text{O}$	70	186–230
Aluminium nitrate nonahydrate	$\text{Al}(\text{NO}_3)_3 \cdot 9\text{H}_2\text{O}$	72	155–176
Barium hydroxide octahydrate	$\text{Ba}(\text{OH})_2 \cdot 8\text{H}_2\text{O}$	78	265–280
Aluminium sulphate 18-hydrate	$\text{Al}_2(\text{SO}_4)_3 \cdot 18\text{H}_2\text{O}$	88	218
Strontium hydroxide octahydrate	$\text{Sr}(\text{OH})_2 \cdot 8\text{H}_2\text{O}$	89	370
Magnesium nitrate hexahydrate	$\text{Mg}(\text{NO}_3)_2 \cdot 6\text{H}_2\text{O}$	89.9	167
Aluminium potassium sulphate dodecahydrate	$\text{KAl}(\text{SO}_4)_2 \cdot 12\text{H}_2\text{O}$	91	184
Ammonium alum	$(\text{NH}_4)\text{Al}(\text{SO}_4) \cdot 6\text{H}_2\text{O}$	95	269
Lithium chloride monohydrate	$\text{LiCl} \cdot \text{H}_2\text{O}$	99	212
Calcium bromide tetrahydrate	$\text{CaBr}_2 \cdot 4\text{H}_2\text{O}$	110	n.a.
Aluminium sulphate 16-hydrate	$\text{Al}_2(\text{SO}_4)_3 \cdot 16\text{H}_2\text{O}$	112	n.a.
Magnesium chloride hexahydrate	$\text{MgCl}_2 \cdot 6\text{H}_2\text{O}$	117	167

Appendix A4 – Transition temperature and latent heat capacity of some metallic PCMs [10]

Name	$T_m$ (°C)	$H$ (kJ/kg)
Mercury	-38.87	11.4
Cesium	28.65	16.4
Gallium-gallium antimony	29.8	n.a.
Gallium	30	80.3
Rubidium	38.85	25.74
Bismuth-lead-indium-tin-cadmium ( $\text{Bi}_{44.7}\text{Pb}_{22.6}\text{In}_{19.1}\text{Sn}_{8.3}\text{Cd}_{5.3}$ )	47	36.8
Bismuth-indium-lead-tin ( $\text{Bi}_{49}\text{In}_{21}\text{Pb}_{18}\text{Sn}_{12}$ )	58	28.9
Cerrowlow	58	90.9
Bismuth-cadmium-indium	61	25
Potassium	63.2	59.59
Cerrobend	70	32.6
Bismuth-lead-tin-cadmium ( $\text{Bi}_{30}\text{Pb}_{26.7}\text{Sn}_{13.3}\text{Cd}_{10}$ )	70	39.8
Bismuth-lead-indium	70	29
Bismuth-indium	72	25
Bismuth-lead-tin ( $\text{Bi}_{32}\text{Pb}_{30}\text{Sn}_{18}$ )	96	34.7
Bismuth-lead-tin	96	n.a.
Sodium	97.8	n.a.
Bi-Pb	125	n.a.
Bismuth-tin ( $\text{Bi}_{58}\text{Sn}_{42}$ )	138	44.8
Indium	156.8	28.59
Lithium	186	433.78
Tin-zinc ( $\text{Sn}_{91}\text{Zn}_9$ )	199	32.5
Tin	232	60.5
Bismuth	271.4	53.3

Appendix A5 – Transition temperature and latent heat capacity of some eutectic materials [10]

Name	Composition (wt%)	$T_m$ (°C)	$H$ (kJ/kg)
Diethylene glycol	n.a.	- 10	247
Tetradecane + octadecane	n.a.	- 4.02	227.52
Water + polyacrylamide	n.a.	0	295
Tetradecane + docosane	n.a.	1.5–5.6	234.33
Tetradecane + hexadecane	91.67 + 8.33	1.7	156.2
Tetradecane + geneicosane	n.a.	3.54– 5.56	200.28
$\text{Na}_2\text{SO}_4 + \text{NaCl} + \text{KCl} + \text{H}_2\text{O}$	31 + 13 + 16 + 40	4	234
Tetrahydrofurano (THF)	n.a.	5	280
Pentadecane + heneicosane	n.a.	6.23–7.21	128.25
Pentadecane + docosane	n.a.	7.6–8.99	214.83
Pentadecane + octadecane	n.a.	8.5–9.0	271.93
$\text{Na}_2\text{SO}_4 + \text{NaCl} + \text{NH}_4\text{Cl} + \text{H}_2\text{O}$	32 + 14 + 12 + 42	11	n.a.
$\text{C}_5\text{H}_5\text{C}_6\text{H}_5 + (\text{C}_6\text{H}_5)_2\text{O}$	26.5 + 73.5	12	97.9
Triethylolethane + water + urea	38.5 + 31.5 + 30	13.4	160
$\text{CaCl}_2 \cdot 6\text{H}_2\text{O} + \text{CaBr}_2 \cdot 6\text{H}_2\text{O}$	45 + 55	14.7	140
$\text{Na}_2\text{SO}_4 + \text{NaCl} + \text{H}_2\text{O}$	37 + 17 + 46	18	n.a.
Capric + lauric acid	61.5 + 38.5	19.1	132
Capric + lauric acid	82 + 18	19.1–20.4	147
Capric + lauric acid	45 + 55	21	143
Capric + myrctic	73.5 + 26.5	21.4	152
Capric + palmitate	75.2 + 24.8	22.1	153
$\text{Na}_2\text{S}_4 + \text{MgSO}_4 + \text{H}_2\text{O}$	25 + 21 + 54	24	n.a.
$\text{C}_{14}\text{H}_{28}\text{O}_2 + \text{C}_{10}\text{H}_{20}\text{O}_2$	34 + 66	24	147.7
$\text{CaCl}_2 \cdot 6\text{H}_2\text{O} + \text{MgCl}_2 \cdot 6\text{H}_2\text{O}$	50 + 50	25	95
$\text{CaCl}_2 \cdot 6\text{H}_2\text{O} + \text{Nucleat} + \text{MgCl}_2 \cdot 6\text{H}_2\text{O}$	66.7 + 33.3	25	127
$\text{CaCl}_2 + \text{NaCl} + \text{KCl} + \text{H}_2\text{O}$	48 + 4.3 + 0.4 + 47.3	26.8	188
Capric + stearate	86.6 + 13.4	26.8	160
$\text{CH}_3\text{CONH}_2 + \text{NH}_2\text{CONH}_2$	50 + 50	27	163
Triethylolethane + urea	62.5 + 37.5	29.8	218
$\text{Ca}(\text{NO}_3)_2 \cdot 4\text{H}_2\text{O} + \text{Mg}(\text{NO}_3)_2 \cdot 6\text{H}_2\text{O}$	47 + 53	30	136
$\text{CH}_3\text{COONa} \cdot 3\text{H}_2\text{O} + \text{NH}_2\text{CONH}_2$	40 + 60	30	200.5
Lauric + palmitic acid	69 + 31	35.2	166.3
$\text{NH}_2\text{CONH}_2 + \text{NH}_4\text{NO}_3$	53 + 47	46	95
$\text{Mg}(\text{NO}_3)_2 \cdot 6\text{H}_2\text{O} + \text{NH}_4\text{NO}_3$	61.5 + 38.5	52	125.5
$\text{Mg}(\text{NO}_3)_2 \cdot 6\text{H}_2\text{O} + \text{MgCl}_2 \cdot 6\text{H}_2\text{O}$	58.7 + 41.3	59	132.2
$\text{Mg}(\text{NO}_3)_2 \cdot 6\text{H}_2\text{O} + \text{MgCl}_2 \cdot 6\text{H}_2\text{O}$	50 + 50	59.1	144
$\text{Mg}(\text{NO}_3)_2 \cdot 6\text{H}_2\text{O} + \text{Al}(\text{NO}_3)_3 \cdot 9\text{H}_2\text{O}$	53 + 47	61	148
$\text{CH}_3\text{CONH}_2 + \text{C}_{17}\text{H}_{35}\text{COOH}$	50 + 50	65	218
$\text{Mg}(\text{NO}_3)_2 \cdot 6\text{H}_2\text{O} + \text{MgBr}_2 \cdot 6\text{H}_2\text{O}$	59 + 41	66	168
Napthalene + benzoic acid	67.1 + 32.9	67	123.4
$\text{AlCl}_3 + \text{NaCl} + \text{ZrCl}_2$	79 + 17 + 4	68	234
$\text{AlCl}_3 + \text{NaCl} + \text{KCl}$	66 + 20 + 14	70	209
$\text{NH}_2\text{CONH}_2 + \text{NH}_4\text{Br}$	66.6 + 33.4	76	151
$\text{LiNO}_3 + \text{NH}_4\text{NO}_3 + \text{NaNO}_3$	25 + 65 + 10	80.5	113
$\text{LiNO}_3 + \text{NH}_4\text{NO}_3 + \text{KNO}_3$	26.4 + 58.7 + 14.9	81.5	116
$\text{LiNO}_3 + \text{NH}_4\text{NO}_3 + \text{NH}_4\text{Cl}$	27 + 68 + 5	81.6	108
$\text{AlCl}_3 + \text{NaCl} + \text{KCl}$	60 + 26 + 14	93	213
$\text{AlCl}_3 + \text{NaCl}$	66 + 34	93	201
$\text{NaNO}_2 + \text{NaNO}_3 + \text{KNO}_3$	40 + 7 + 53	142	n.a.

## Data sheet



# RT26



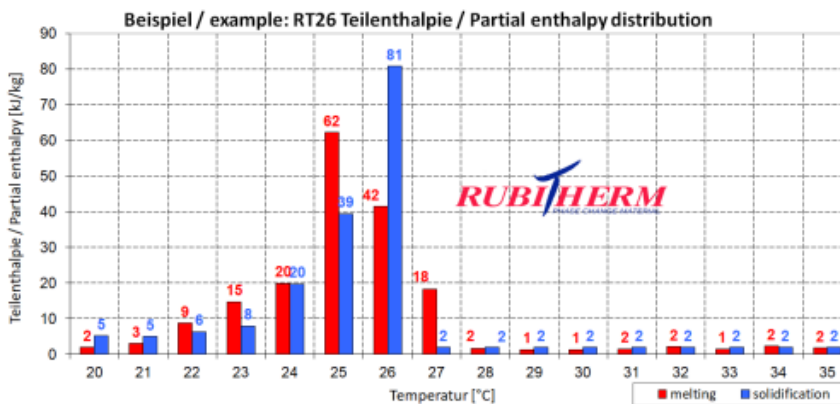
RUBITHERM® RT is a pure PCM, this heat storage material utilising the processes of phase change between solid and liquid (melting and congealing) to store and release large quantities of thermal energy at nearly constant temperature. The RUBITHERM® phase change materials (PCM's) provide a very effective means for storing heat and cold, even when limited volumes and low differences in operating temperature are applicable.

**Properties for RT-line:**

- high thermal energy storage capacity
- heat storage and release take place at relatively constant temperatures
- no supercooling effect, chemically inert
- long life product, with stable performance through the phase change cycles
- melting temperature range between -9 °C and 100 °C available

**The most important data:**

	Typical Values	
<b>Melting area</b>	<b>25-26</b>	[°C]
	main peak: 26	
<b>Congeeing area</b>	<b>26-25</b>	[°C]
	main peak: 26	
<b>Heat storage capacity ± 7,5%</b> Combination of latent and sensible heat in a temperatur range of 19°C to 34°C.	<b>180</b>	[kJ/kg]*
	<b>50</b>	[Wh/kg]*
<b>Specific heat capacity</b>	<b>2</b>	[kJ/kg·K]
<b>Density solid</b> at 20°C	<b>0,88</b>	[kg/l]
<b>Density liquid</b> at 30°C	<b>0,75</b>	[kg/l]
<b>Heat conductivity (both phases)</b>	<b>0,2</b>	[W/(m·K)]
<b>Volume expansion</b>	<b>12,5</b>	[%]
<b>Flash point</b>	<b>150</b>	[°C]
<b>Max. operation temperature</b>	<b>60</b>	[°C]



Rubitherm Technologies GmbH  
 Imhoffweg 6  
 D-12307 Berlin  
 phone: +49 (30) 7109622-0  
 E-Mail: info@rubitherm.com  
 Web: www.rubitherm.com

The product information given is a non-binding planning aid, subject to technical changes without notice.  
 Version: 09.10.2020

# Curriculum Vitae

**Name:** Colin Jaffray

**Post-secondary Education and Degrees:** University of Ontario Institute of Technology  
Oshawa, Ontario, Canada  
2014-2019. B.Eng.

**Related Work Experience** Teaching Assistant  
The University of Western Ontario  
2020-2022